Since 1955

Strojniški vestnik
Journal of Mechanical Engineering

no. 9
year 2017
volume 63

Strojniški vestnik – Journal of Mechanical Engineering (SV-JME)

Aim and Scope
The international journal publishes original and (mini)review articles covering the concepts of materials science, mechanics, kinematics, thermodynamics, energy and environment, mechatronics and robotics, fluid mechanics, tribology, cybernetics, industrial engineering and structural analysis.
The journal follows new trends and progress proven practice in the mechanical engineering and also in the closely related sciences as are electrical, civil and process engineering, medicine, microbiology, ecology, agriculture, transport systems, aviation, and others, thus creating a unique forum for interdisciplinary or multidisciplinary dialogue.
The international conferences selected papers are welcome for publishing as a special issue of SV-JME with invited co-editor(s).

Editorial Office
University of Ljubljana, Faculty of Mechanical Engineering
SV-JME, Aškerčeva 6, SI-1000 Ljubljana, Slovenia
Phone: 386 (0)1 4771 137
Fax: 386 (0)1 2518 567
info@sv-jme.eu, http://www.sv-jme.eu

Print: Papirografika Bori, printed in 300 copies

Founders and Publishers
University of Ljubljana, Faculty of Mechanical Engineering, Slovenia
University of Maribor, Faculty of Mechanical Engineering, Slovenia
Association of Mechanical Engineers of Slovenia
Chamber of Commerce and Industry of Slovenia, Metal Processing Industry Association

Cover:
The figure shows the implementation of the cyclic loading of the console beam mounted with an additional clamping device on the Instron 8802 uni-axial testing device and prepared for the analysis of the deformation field with the Gom Aramis 5M optical measuring system.

Image Courtesy:
Andrej Žerovnik, University of Ljubljana, Faculty of Mechanical Engineering, Slovenia

General information
Strojniški vestnik – Journal of Mechanical Engineering is published in 11 issues per year (July and August is a double issue).

Institutional prices include print & online access: institutional subscription price and foreign subscription €100,00 (the price of a single issue is €10,00); general public subscription and student subscription €50,00 (the price of a single issue is €5,00). Prices are exclusive of tax. Delivery is included in the price. The recipient is responsible for paying any import duties or taxes. Legal title passes to the customer on dispatch by our distributor.

Single issues from current and recent volumes are available at the current single-issue price. To order the journal, please complete the form on our website. For submissions, subscriptions and all other information please visit: *http://en.sv-jme.eu/.*

You can advertise on the inner and outer side of the back cover of the journal. The authors of the published papers are invited to send photos or pictures with short explanation for cover content.

We would like to thank the reviewers who have taken part in the peer-review process.

ISSN 0039-2480

The journal is subsidized by Slovenian Research Agency.

Strojniški vestnik - Journal of Mechanical Engineering is available on http://www.sv-jme.eu, where you access also to papers' supplements, such as simulations, etc.

Contents

Strojniški vestnik - Journal of Mechanical Engineering
volume 63, (2017), number 9
Ljubljana, September 2017
ISSN 0039-2480

Published monthly

Papers

Strojniški vestnik - Journal of Mechanical Engineering 63(2017)9, 479-488

DOI:10.5545/sv-jme.2017.4499 Original Scientific Paper
Received for review: 2017-05-26
Received revised form: 2017-08-17
Accepted for publication: 2017-08-24

The Yield-Point Phenomenon and Cyclic Plasticity of the Console Beam

Andrej Žerovnik* – Ivan Prebil – Robert Kunc
University of Ljubljana, Faculty of Mechanical Engineering, Slovenia

In the paper, the influence of the yield-point phenomenon (YPP) on cyclic plasticity of the console beam is presented with the objective to demonstrate the impact of the YPP on the local cyclic plasticity. The influence of the YPP and its dependence on cyclic material hardening or softening was studied through experiments and numerical simulations. Console beams are made from the low-alloy EN 42 CrMo 4 steel in its normalized state (184 HV), which exhibits cyclic hardening, and in its tempered state (296 HV), which is subject to cyclic softening. Numerical simulations were performed on constitutive model of cyclic plasticity taking into account the kinematic hardening, isotropic hardening or softening and formulations of the YPP which are based on the change of the elastic region surface in the stress space at first transition into the stress plateau. Analysis of the results shows the importance of taking into account the YPP equations in constitutive models of cyclic plasticity as well as the influence of the YPP on cyclic plasticity of the console beam.
Keywords: yield-point phenomenon, cyclic plasticity, mechanical testing, FEM simulations

Highlights
- *The yield-point phenomenon (YPP) was observed in relation with cyclic plasticity of the console beam.*
- *The influence of the YPP on cyclic plasticity of the console beam was determined from experimental and numerical simulations of cyclic bend tests.*
- *Research was made with the objective to demonstrate the impact of the YPP on the local cyclic plasticity.*
- *Based on the presented results, it is evident that formulation of the YPP in constitutive models of cyclic plasticity leads to more realistic results of cyclic plasticity.*

0 INTRODUCTION

The yield-point phenomenon (YPP) is the result of a rapid increase in the number of mobile dislocations **[1]** and **[2]** and is common in iron **[3]**, low-alloy steels **[4]** and **[5]**, titanium alloys **[6]**, aluminium **[7]** and **[8]**, tantalum **[9]** and **[10]** and several other metallic alloys **[11]** to **[14]** as well as in composites and laminates **[15]** and **[16]**, polymers **[17]** and **[18]** and even rocks **[19]** and **[20]**.

Most previous studies that were engaged with the influence of the YPP analyse the reasons behind its development and its effects on monotonic loading **[1]**, **[2]** and **[5]**. The stress state and the reasons associated with Lüders banding were researched by Schwab and Ruff **[21]**. Barnett et al. **[14]** made a major step by experimental microstructural analysis for verification of the onset of deformation twinning in Lüders bands. Wenman and Chard-Tuckey **[22]** analyse the effect of the Lüders strains on residual stresses from various material hardening models in uniaxially-loaded specimens. The effect of Lüders bands on the bending of steel tubes was discussed by Aguirre et al. **[23]**, Hallai and Kyriakides **[24]** and Bechle and Kyriakides **[6]**. Recently, Zou et al. **[25]** observed cyclic loading in yield plateau and Žerovnik et al. **[26]** presented the influence of the YPP on cyclic plasticity of the uniaxially loaded specimens.

The first to describe the uniaxial model of the YPP was Hahn **[27]**. The presented model described the stress drop based on Johnston and Gilman's **[28]** concept of a rapid increase in the number of mobile dislocations at the yield point. Shioya and Shioiri **[29]** later expanded Hahn's model to a multiaxial one, while Itoh et al. **[30]** was the first to implement Hahn's model to the finite-element code.

Cyclic plasticity research has a long and rich tradition. Armstrong and Frederick **[31]** were among the first to describe kinematic hardening. Their work was later extended by Chaboche et al. **[32]** and Chaboche **[33]** and **[34]**, whose proposal included a superposition of three kinematic rules. Mostly with a view to further improve ratcheting simulation, several other models were later proposed **[32]**, **[35]** to **[41]**. Chaboche **[42]** presented a comprehensive overview of the selected constitutive models. Particularly worth mentioning is the Ohno-Wang model **[43]** and **[44]**, which introduced critical state of dynamic recovery into kinematic hardening rules. Although of a slightly earlier date, the Ohno-Wang model had not lost its relevance, as was confirmed by Yu et al. **[40]** in their upgraded model integrating equations of cyclic visco-plasticity. Similarly, the Ohno-Wang model was also

*Corr. Author's Address: University of Ljubljana, Faculty of Mechanical Engineering, Ljubljana, Slovenia, andrej.zerovnik@fs.uni-lj.si

modified by Abdel-Karim [39], who proved that inclusion of isotropic hardening enabled the model to predict uniaxial as well as multiaxial ratcheting. Another interesting model that related cyclic hardening to the plastic strain history was proposed by Korelc et al. [45].

However, only few research studies [26], [46] to [48] are focused on the effect of the YPP in combination with cyclic plasticity. Even the materials which express the YPP was addressed by constitutive models of cyclic plasticity, the YPP is not taken into account in most of those models. [49] to [51]. In most cyclic load cases, the zone of elastic deformation surrounds the plastic deformation zone, and failure to consider the YPP would lead to incorrect predictions of plastic deformation deviating from the real-life situation. In order to conduct precise stress-strain analyses, a constitutive model is needed which enables accurate descriptions of the YPP as well as subsequent cyclic plasticity. In the recent period, Yoshida [47] and [48] has made a significant contribution in this field. He has presented two rate-dependent models of cyclic plasticity, which describe kinematic and isotropic hardening as well as the YPP. In his model based on the micromechanical approach, Yoshida claims that after the yield point an abrupt yield drop takes place because of the rapid multiplication of dislocations. Besides describing the phenomenon, Yoshida also used the benefits of the YPP for solving real-world problems [47]. Žerovnik et al. [46] presented their observations of the YPP based on the phenomenological approach which relates the yield plateau with a reduction in the size of the elastic region surface and displacement of the elastic region centre in the stress space.

The aim of this paper is to present and evaluate the influence of the YPP on cyclic plasticity behavior of the console beam, with the objective to demonstrate the impact of the YPP on the local cyclic plasticity. The study is based on a combination of experimental observations and numerical simulations.

1 EXPERIMENTAL OBSERVATIONS

The influence of the YPP on cyclic plasticity was estimated from cyclic bend tests of console beams (Fig. 1). Console beams were made from low-alloy EN 42 CrMo 4 steel, which exhibits cyclic hardening in its normalized state and cyclic softening in its tempered state [26]. To analyse the impact of the YPP in combination with cyclic hardening or softening, console beams were prepare in two different states, normalized (184 HV) and hardened (296 HV).

The experiments were conducted on the Instron 8802 test rig [52]. An additional clamping device was made for the purpose of attaching the specimens (Fig. 2). The stiffness of the clamping device was verified through numerical stress-strain simulations, which showed that the impact of the clamping device strains on console beam displacement is less than 1 % of the measured value in all predicted load cases. Instron 2527-101 dynamic load cell (capacity ±250 kN and certified measurement system error ±0.1 % of total range) was used to measure the force applied to the beam and the console beam displacement was measured using Instron 2620-604 Dynamic Extensometer (gauge length of 15 mm and certified measurement system error ±0.1 % of total travel) (Fig. 2). Symmetric and asymmetric cyclic bend tests were performed under displacement control (Table 1) at a loading frequency of 0.5 Hz and under time-dependent sinusoidal load.

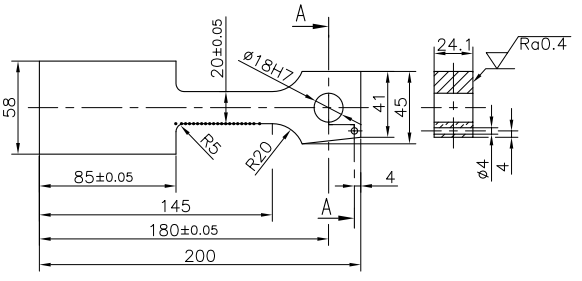

Fig. 1. *A console beam*

Table 1. *Cyclic bend experiments of console beams*

Specimen	Displacement amplitude [mm]	Heat treatment
CN1	2	Normalized (184 HV)
CN2	3	
CN3	4	
CN4	2*	
CT1	3	Tempered (296 HV)
CT2	4	

* Asymmetric loading, mean displacement value is 2 mm.

During cyclic loading of the console beams made of 184 HV steel, the GOM Aramis 5M measurement system was used to observe the strain field of the specimens (Fig. 2). Optical measurement system has lenses with a focal point of 50 mm, the area of image capture was 35 mm× 29 mm. System resolution at 0.032 pixels and system error at 0.06 pixels is automatically evaluated.

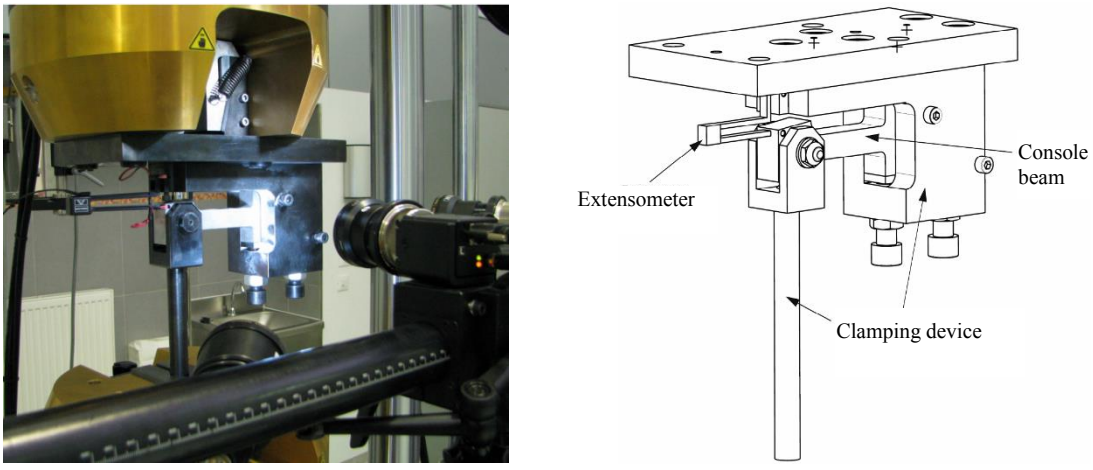

Fig. 2. *Cyclic loading of a console beam*

2 NUMERICAL SIMULATIONS

A source code for a three-dimensional eight-node isoparametric finite element was generated for FEM-based numerical simulations. The formulation was based on the displacement field method, and the stiffness matrix was derived with the variation approach [46]. The FE code was generated using the symbolic algebra package AceGen [53]. Additionally, FE models of a console beam were built (Fig. 3).

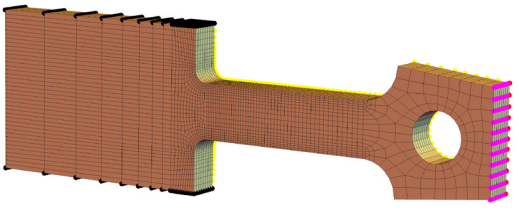

Fig. 3. *FE model of a console beam loaded in bending*

The constitutive model integrated in the FE code is based on the phenomenological approach and the small-strain theory. The isotropic material properties are assumed. The model includes descriptions of material cyclic hardening or softening, nonlinear kinematic hardening, and the YPP. Also, it takes into account the von Mises yield surface, whereas the equation defining the size of the yield surface F is supplemented by coefficients of the YPP as well as cyclic and kinematic hardening [46]:

$$F = \tilde{\sigma}_{eq} - \left(R - M + \sigma_{Ypre}\right) + \sigma_{Ycor} = 0, \tag{1}$$

where σ_{Ypre} stands for the stress of the upper yield point and R for the coefficient of cyclic hardening or softening. M is the coefficient of the YPP which denotes the isotropic changing of the elastic region size within the stress space resulting from an increase in the number of mobile dislocations at transition from the elastic into the elasto-plastic region. σ_{Ycor} is the yield stress correction expressing the change in the size of the elastic region within the yield region. $\tilde{\sigma}_{eq}$ denotes equivalent stress [46].

The shift in the position of the elastic domain in the stress space (i.e. the Bauschinger effect) is given by the evolution equation for the back stress describing kinematic hardening, which was originally proposed by Armstrong and Frederick [31] and later extended by Chaboche [33]:

$$\mathbf{X} = \sum_{n=1}^{3} \mathbf{X}^{(n)}. \tag{2}$$

The segments of the kinematic curve (n=1, 2, 3) are described by an equation proposed by Ohno and Wang [43] and [44], which takes into account the Bauschinger effect and uses the Ohno-Wang parameters to consider mean-stress relaxation in the event of asymmetric hardening:

$$\dot{\mathbf{X}}^{(n)} = \frac{2}{3}\gamma^{(n)} X_{\infty}^{(n)} \dot{\boldsymbol{\mu}}^{p} - \left(\frac{X_{eq}^{(n)}}{X_{\infty}^{(n)}}\right)^{m^{(n)}} \mathbf{X}^{(n)} \gamma^{(n)} \dot{\lambda}. \tag{3}$$

The change in the elastic region size in the stress space is defined by the isotropic cyclic hardening or softening equation. Uniaxial experimental observations [26] show that material hardening or softening continues for the specimen's whole remaining life time. The rate of hardening also depends on the magnitude of the plastic strain. In his observations of cyclic plasticity in construction steels, Korelc [45] detected similar behavior and later

described the isotropic cyclic material response with a cyclic hardening model that integrates the time history of plastic deformation:

$$\dot{R} = b_0 \left(b_1 \cdot \lambda + R_\infty \left(\varepsilon_{p,\max} \right) - R \right) \dot{\lambda} + b_1 \cdot \dot{\lambda}, \tag{4}$$

where:

$$b_1 = \operatorname{sgn}(R_{\infty,s}) \cdot 1 - e^{-s_0 \cdot \varepsilon_{p,\max}}, \tag{5}$$

$$R_\infty = R_{\infty,s} \left(1 + (\alpha - 1) e^{-\xi \cdot \varepsilon_{p,\max}} \right). \tag{6}$$

Yoshida **[47]** and **[48]** was the first to point out that it is not sensible to consider cyclic hardening or softening in the region of Lüders bands (ε_L).This applies only to the first transition from the elastic into the elasto-plastic region (monotonic loading), and not to subsequent cyclic loading in the Lüders strain region.

The YPP in Eq. (1) is described by M and σ_{Ycor}. The stress drop after the upper yield point is described by the equation denoting the isotropic changing of the elastic region size **[46]**:

$$\dot{M} = c(\sigma_{Ydrop} - M)\dot{\lambda}. \tag{7}$$

The correction of yield stress which describes the change of the elastic region size in the stress plateau and is taken account of in the yield Eq. (1) is as follows **[46]**:

$$\sigma_{Ycor} = \begin{cases} X_{eq} & \text{for stress plateau region,} \\ \sigma_{Ypre} - \sigma_{Ypost} - \sigma_{Ydrop} & \text{for strain hardening region.} \end{cases} \tag{8}$$

The constitutive model parameters for EN 42 CrMo 4 which were used in the implementation of numerical simulations are given by Table 2.

3 RESULTS AND DISCUSSION

The results of the analyses of cyclic plasticity of console beams will be presented in this paper to provide a clearer picture of the influence which the YPP has on cyclic plasticity of the structural elements, where local cyclic plasticity occurs.

Numerical simulations were conducted for two model cases: firstly, for the constitutive model which includes YPP descriptions (with the YPP), and secondly, for the constitutive model not taking account of the YPP (without the YPP).

Table 2. *EN 42 CrMo 4 material parameters of the constitutive model*

Parameter	Unit	Normalized (184 HV)	Tempered (296 HV)
E	N/mm²	203020	198085
ν	–	0.3	0.3
c	–	2800	1800
ε_L	–	0.007	0.01
σ_{Ypre}	N/mm²	410	850
σ_{Ypost}	N/mm²	180	520
σ_{Ydrop}	N/mm²	40	28
B_0	–	35	10
$R_{\infty,s}$	N/mm²	65	-195
S_0	–	155	92
α	–	0.02	0.9
ζ	–	105	155
γ_1	–	3200	549
γ_2	–	600	103
γ_3	–	27	40
$X^1{}_\infty$	N/mm²	50	245
$X^2{}_\infty$	N/mm²	75	157
$X^3{}_\infty$	N/mm²	400	180
m^1	–	5	2
m^1	–	5	1.5
m^1	–	1.5	0.8

Formulation and material parameters of the constitutive model for isotropic hardening/softening and kinematic hardening are the same in both cases. The results obtained from numerical simulations were compared against experimental data. In terms of the stress-strain curves of uniaxial tensile-compression loads **[26]**, the difference between the two models (model with the YPP and model without the YPP) only exists in the first cycle, where transition from the elastic into the elasto-plastic region occurs at different yield stress. The model with the YPP is consistent with the experimental results, whereas the model without the YPP in the first cycle at transition into plastic strain does not follow the experimental results. Fig. 4. shows the comparison between different shapes of the stress-strain curve exhibited by the uniaxially cyclically loaded specimens.

The following part of the paper presents the impact of the YPP formulation on the results of numerical simulations of the cyclically loaded console beam in bending. Due to long computation times, numerical simulations for all load cases of cyclic plasticity of console beams were performed for the first 100 cycles. In view of their high number, the results of certain load cases which showed similar effects or benefits are not presented.

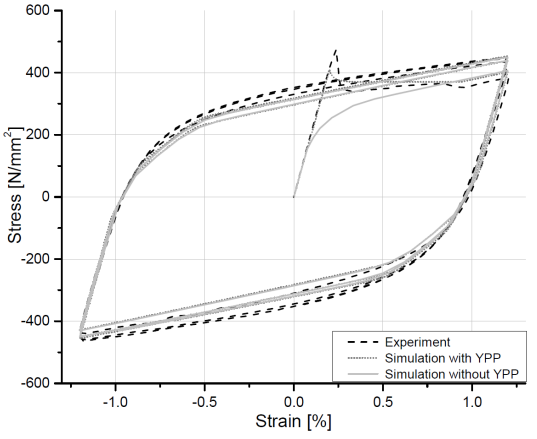

Fig. 4. *Comparison of stress-strain hysteresis loops under uniaxial tensile-compression cyclic loading, strain amplitude $\Delta\varepsilon$ = 1.2 %, for models with and without the YPP (184 HV)*

Figs. 5, 6, 9 and 10 show a comparison of force-displacement hysteresis loops for the first and second cycles and the force and displacement amplitudes in relation to the number of cycles for the 184 HV material, while Fig. 11 illustrates the flow of force amplitudes relative to the number of cycles for the 296 HV material.

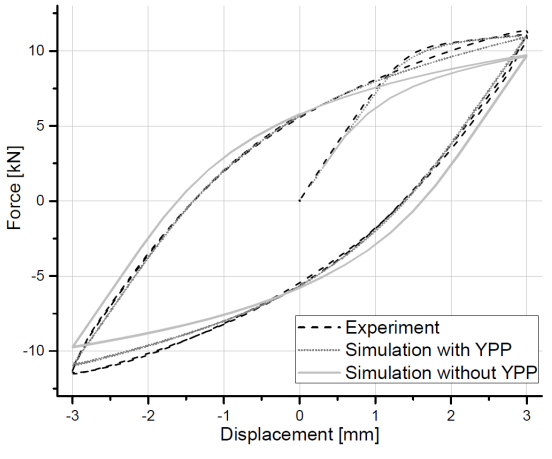

Fig. 5. *Comparison of force-displacement hysteresis loops for the 1st and 2nd cycle at a displacement amplitude of 3 mm, 184 HV material*

Fig. 5 shows force-displacement hysteresis loops for the first and second cycle, under cyclic loading at a displacement amplitude of 3 mm. The figure demonstrates very good agreement between the experimental and numerical results for models including the YPP, whereas simulation results deviate across the entire loaded region if the YPP is not considered in the constitutive model. These deviations are most expressed in the shape of the first cycle hysteresis loop. When the YPP is not taken into account, the force-displacement curve transits from the linear into the nonlinear region at a force of 4 kN; otherwise, this transition takes place at 8.5 kN.

A similar trend is evident in the comparison of force amplitudes and the number of cycles (Fig. 6). In simulations with the YPP, numerically-obtained force amplitude results deviate from experimental data by a maximum of 3 % at a strain amplitude of 2 mm, while in models without the YPP, the discrepancy between experimental and simulation results is between 6 % and 20 %. It should also be noted that in models with the YPP the force amplitude curve (Fig. 6) is similar in shape across the entire region to the curves obtained from experiments. If the YPP is not taken into account, the shape of the curve deviates more significantly. A satisfactory agreement of numerical and experimental results is also revealed in load cases at a displacement amplitude of 3 mm (Fig. 6). Simulation-generated force amplitude curves taking account of the YPP only deviate from experimental results in the first 20 cycles, by a maximum of 4 %, while deviations between experimental and simulation results for cases where the phenomenon is not considered are between 4 % and 15 %.

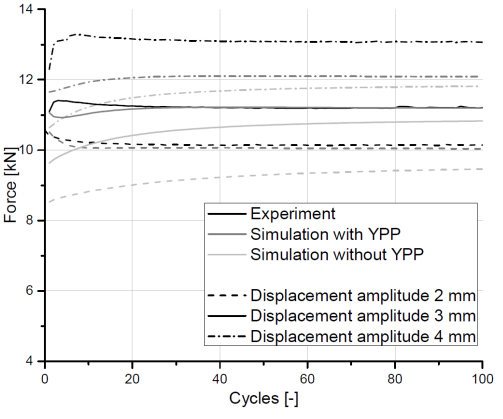

Fig. 6. *Comparison of force amplitudes under cyclic loading at symmetric displacement amplitudes of 2, 3 and 4 mm, 184 HV material*

Slightly lower agreement between the model with the YPP and experiment becomes evident during loading at a displacement amplitude of 4 mm (Fig. 6). The discrepancy results from slightly changed characteristics of the specimen material which exhibits faster hardening in the cyclic strain region. This hypothesis is confirmed in Fig. 9, which indicates that the curves for experimental and simulation results that include the YPP show a good agreement during the first cycle up to the displacement of 4 mm.

It is interesting to observe and compare force amplitudes for symmetric load cases at displacement amplitudes of 2 mm and 4 mm (Fig. 6), since they show different force amplitude curves for experiment and simulation results if the YPP is considered. Symmetric load cases at a displacement amplitude of 2 mm display a drop in the force amplitude curve. Under symmetric loading at a displacement amplitude of 4 mm the force amplitude rises. The change in the softening or hardening trend is due to the prevalent influence of the YPP for the 2 mm displacement amplitude and the influence of isotropic cyclic hardening for the 4 mm displacement amplitude. This is evident in Figs. 7 and 8, which show the values of the isotropic hardening variable (R) and the yield stress correction variable (σ_{Ycor}). The figures show the state of the console beam after the 1st, 20th, 50th and 100th cycle on the observed region, marked with a dotted line in Fig. 1. At a displacement amplitude of 2 mm (Fig. 7), the state of the material in the observed region during the first few cycles is within the stress plateau and consequently σ_{Ycor} increases. A significant increase occurs in the right part of the console beam (at a distance between 105 mm and 123 mm). Similarly to σ_{Ycor}, the isotropic hardening variable (R) also increases during the cyclic loading. In the left part of the observed console beam field (at a distance between 85 mm and 105 mm from the left face), the change in variables R and σ_{Ycor} is of the same magnitude, whereas in the right part (at a distance between 105 and 123 mm) the change in variable σ_{Ycor} is more prominent, which consequently affects the force amplitude drop. The force drop is in relation with the nonhomogeneous material response in the first cycles when the strain amplitude is lower than Lüders strain **[26]**. In the event of a displacement amplitude of 4 mm (Fig. 8), in the observed region of the console beam plastic strain occurs during the first loading is bigger than the stress plateau (Fig. 12), due to which variable σ_{Ycor} reaches its limit value in the first cycle in the left part of the observed region of the console beam. Consequently, during further loading variable σ_{Ycor} changes only in the right part of the observed region of the console beam. Since deformations in this load case are significantly bigger than in the event of loading at a displacement amplitude of 2 mm, the value of the isotropic loading variable R is also bigger. It is prominent in the left part of the observed region of the console beam and consequently leads to force amplitude growth during cyclic loading.

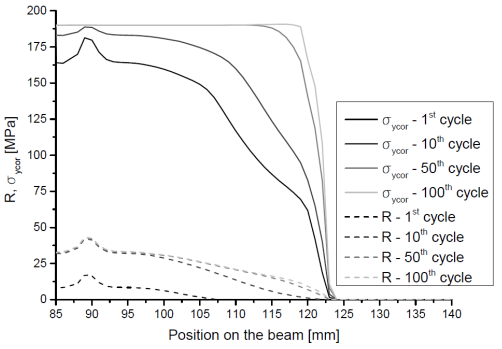

Fig. 7. Values of variables R and σ_{Ycor} under symmetric loading at a strain amplitude of 2 mm

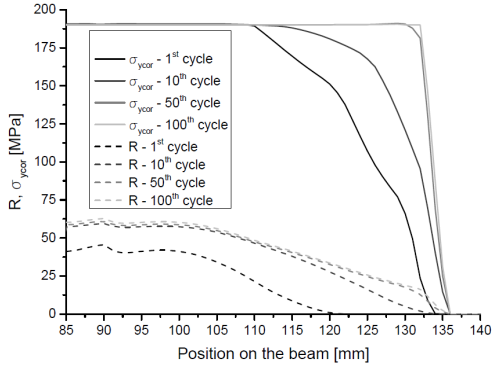

Fig. 8. *Values of variables R and σ_{Ycor} under symmetric loading at a strain amplitude of 4 mm*

In numerical simulations without the YPP, the force amplitude curve constantly increases and does not correspond with experimental data (Fig. 6).

Even in displacement-controlled asymmetric load cases (Figs. 9 and 10), numerical simulation results show a better agreement with experimental results when the YPP is taken into account.

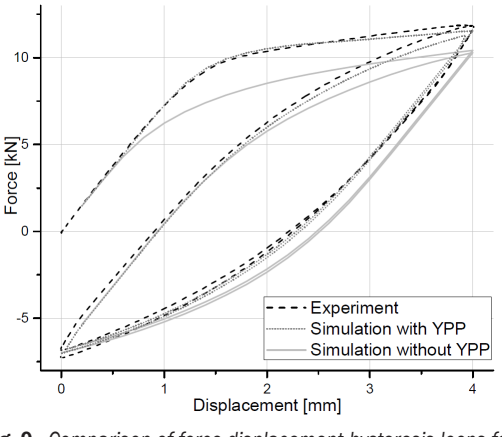

Fig. 9. *Comparison of force-displacement hysteresis loops for the 1st and 2nd cycle under asymmetric loading at a displacement amplitude of 2 mm and mean value of 2 mm, 184 HV material*

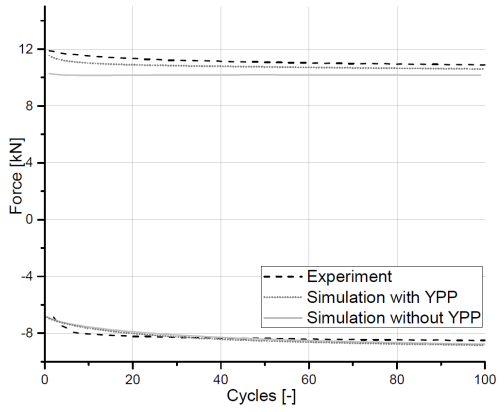

Fig. 10. *Comparison of force amplitudes under asymmetric cyclic loading at a displacement amplitude of 2 mm and mean value of 2 mm, 184 HV material*

Console beams made from the 296 HV material were subjected to cyclic plasticity in order to analyse the influence of the YPP in correlation with cyclic softening. Fig. 11 gives a comparison of force amplitudes in relation to the number of cycles for a displacement amplitude of 4 mm. Experimental results are in good agreement with numerical simulations for the cases including the YPP, and differ by approximately up to 20 % for cases without the YPP.

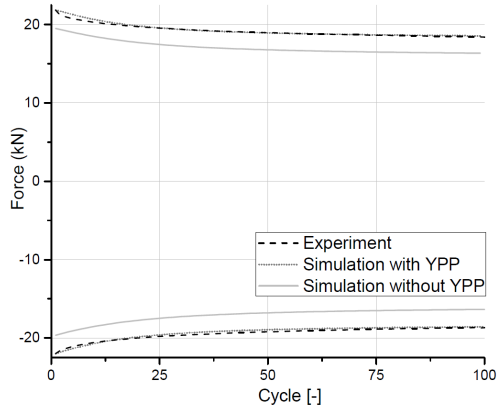

Fig. 11. *Comparison of force amplitudes under cyclic loading at a symmetric displacement amplitude of 4 mm, 296 HV material*

A strain-field comparison is another way to assess the benefit of describing the YPP. Fig. 12 shows a comparison of the von Mises equivalent strain for a displacement amplitude of 4 mm. Strain fields are given for the 1st and 100th cycle. The entire strain of the console beam in the region of greatest deformation is given. As seen below, experimental results are in better agreement with numerical results when the YPP is taken into account, which further supports the merit of supplemented equations describing this phenomenon. The difference is particularly evident in the first cycle but dissipates slightly until the 100th cycle due to cyclic hardening. The influence of the YPP in constitutive models of cyclic plasticity on the strain-stress state of a console beam is clearly expressed in the illustration of von Mises stresses in the beam. Figs. 13 and 14 show a comparison of the stresses in the 1st and 100th cycle for the material with hardness levels of 184 HV and 296 HV for a variety of load cases. The course of maximum von Mises stresses is completely different depending on whether or not the YPP is taken into account. For the 184 HV beams, the maximum comparative stresses in cases considering the YPP amount to 410 N/mm² in the 1st and 100th cycle. If the YPP is not taken into account, these values are 181 N/mm² in the first or 230 N/mm² in the 100th cycle (Fig. 13). The reason behind these differences lies in the inclusion of the YPP as it describes the changes in the size (i.e. reductions) of the elastic region at transition over the Lüders plateau. The growth of maximum comparative stresses in models without the YPP is attributable to cyclic material hardening. Fig. 14, which shows maximum comparative stresses for a 296 HV beam, demonstrates a similar response. In this case, the

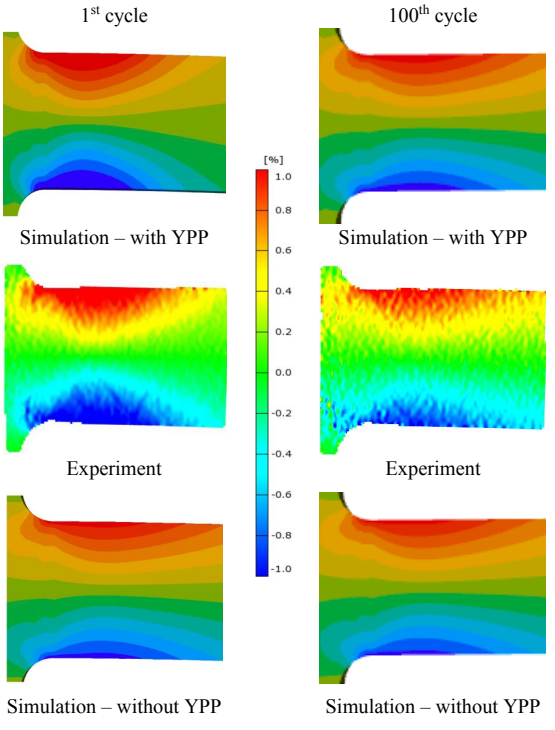

Fig. 12. *Comparison of console beam strain fields for the 184 HV material (symmetric loading, displacement amplitude of 4 mm)*

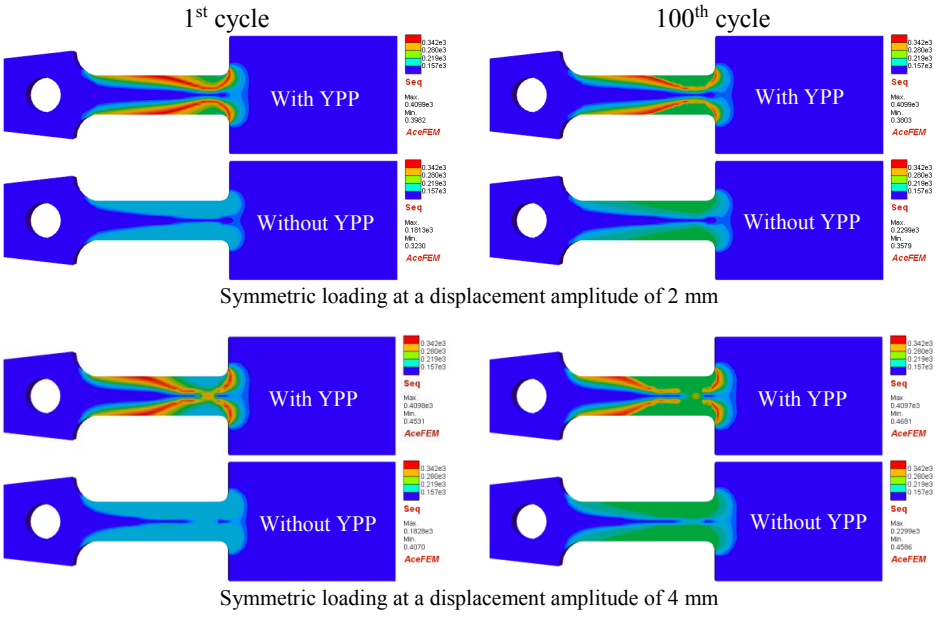

Fig. 13. *Maximum von Mises stress in the 1st and 100th cycle, for models with and without the YPP, 184 HV material*

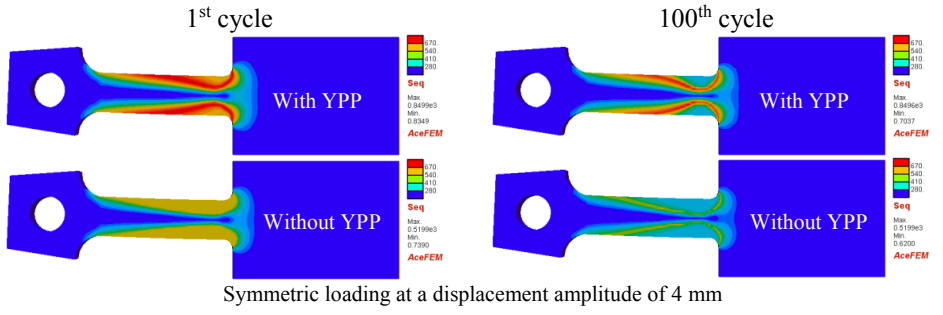

Fig. 14. *Maximum von Mises stress in the 1st and 100th cycle, for models with and without the YPP, 296 HV material*

maximum comparative stresses in the 1st and 100th cycle reach 850 N/mm² if the YPP is taken into account, and 520 N/mm² if it is not included, which is consistent with the model parameters given in Table 2.

Figs. 13 and 14 also point out the differences in the development of von Mises stresses during cyclic softening or hardening. In the 184 HV materials exhibiting cyclic hardening, the plastic strain region expands (in particular at a displacement amplitude of 4 mm and with the YPP, as seen in Fig. 13) and the maximum stress region moves along the beam. In the 296 HV materials exhibiting cyclic softening, the plastic strain region does not grow but rather remains constant throughout 100 cycles (Fig. 14). Cyclic material softening causes the maximum stress region to narrow, even greater is the decrease of maximum von Mises stresses in the region in which the material is subject to cyclic plasticity.

5 CONCLUSIONS

The influences of the YPP on cyclic plasticity of the console beam have been under-researched through experimental observations and numerical simulations. Numerical results for the model with the YPP and model without the YPP formulation were compared with experimental results. The specimens were made from EN 42 CrMo 4 steel in its normalized (184 HV) and tempered hardness values (296 HV) with the purpose to analyse the influence of the YPP in relation to cyclic hardening and softening.

Results such as force vs. displacement, force vs. cycle numbers as well as comparison of strain and stress field of a console beam were presented. Based on the presented results, it is evident that formulation of the YPP in the constitutive models of cyclic plasticity leads to better correlation with experimental

results in all presented cases. Comparison of von Mises stress results for the model with the YPP and without the YPP allows the reader to understand the real significance of the YPP effect on cyclic plasticity. Based on the presented results, it is evident that formulation of the YPP in constitutive models of cyclic plasticity leads to more realistic forecasts of the stress-strain response during cyclic plasticity.

6 REFERENCES

[1] Cottrell, A.H., Bilby, B.A. (1949). Dislocation theory of yielding and strain ageing in iron. *Proceedings of Physics Society A*, vol. 62, no. 1, p. 49-62, **DOI:10.1088/0370-1298/62/1/308**.

[2] Hall, E.O. (1970). *Yield Point Phenomena in Metals and Alloys*. Plenum Press, New York, **DOI:10.1007/978-1-4684-1860-6**.

[3] Franciosi, P., Le, L.T., Monnet, G., Kahloun, C., Chavanne, M.H. (2015). Investigation of slip system activity in iron at room temperature by SEM and AFM in-situ tensile and compression tests of iron single crystals. *International Journal of Plasticity*, vol. 65, p. 226-249, **DOI:10.1016/j.ijplas.2014.09.008**.

[4] Tsuchida, N., Masuda, H., Harada, Y., Fukaura, K., Tomota, Y., Nagai, K. (2008). Effect of ferrite grain size on tensile deformation behavior of a ferrite-cementite low carbon steel. *Materials Science and Engineering: A*, vol. 488, no. 1-2, p. 446-452, **DOI:10.1016/j.msea.2007.11.047**.

[5] Zhang, J., Jiang, Y. (2005). Lüders bands propagation of 1045 steel under multiaxial stress state. *International Journal of Plasticity*, vol. 21, no. 3, p. 651-670, **DOI:10.1016/j.ijplas.2004.05.001**.

[6] Bechle, N.J., Kyriakides, S(2014). Localization in NiTi tubes under bending. *International Journal of Solids and Structures*, vol. 51, no. 5, p. 967-980, **DOI:10.1016/j.ijsolstr.2013.11.023**.

[7] Tsuji, N., Ito, Y., Saito, Y., Minamino, Y. (2002). Strength and ductility of ultrafine grained aluminum and iron produced by ARB and annealing. *Scripta Materialia*, vol. 47, no. 12, p. 893-899, **DOI:10.1016/S1359-6462(02)00282-8**.

[8] Mahmudi, R. (1994). Yield point phenomenon in ultrafine-grained aluminium sheets. *Materials Letters*, vol. 19, no. 5-6, p. 243-246, **DOI:10.1016/0167-577X(94)90164-3**.

[9] Colas, D., Finot, E., Flouriot, S., Forest, S., Mazière, M., Paris, T. (2014). Investigation and modeling of the anomalous yield point phenomenon in pure tantalum. *Materials Science and Engineering: A*, vol. 615, p. 283-295, **DOI:10.1016/j.msea.2014.07.028**.

[10] Knezevic, M., Beyerlein, I.J., Lovato, M.L., Tomé, C.N., Richards, A.W., McCabe, R.J. (2014). A strain-rate and temperature dependent constitutive model for BCC metals incorporating non-Schmid effects: Application to tantalum–tungsten alloys. *International Journal of Plasticity*, vol. 62, p. 93-104, **DOI:10.1016/j.ijplas.2014.07.007**.

[11] Dickson, J.I., Sayar, A. (1977). The influence of aging stress on the yield point phenomenon in the zirconium alloy, ozhennite 0.5. *Journal of Nuclear Materials*, vol. 64, no. 1-2, p. 49-56, **DOI:10.1016/0022-3115(77)90007-1**.

[12] González-Doncel, G., Adeva, P., Cristina, M.C., Ibá-ez, J. (1995). Lüders bands formation in a rapidly solidified Ni_3Al alloy ribbon. *Acta Metallurgica et Materialia*, vol. 43, no. 12, p. 4281-4287, **DOI:10.1016/0956-7151(95)00140-Q**.

[13] Min, J., Hector, Jr. L.G., Lin, J., Carter, J.T., Sachdev, A.K. (2014). Spatio-temporal characteristics of propagative plastic instabilities in a rare earth containing magnesium alloy. *International Journal of Plasticity*, vol. 57, p. 52-76, **DOI:10.1016/j.ijplas.2014.02.004**.

[14] Barnett, M.R., Nave, M.D., Ghaderi, A. (2012). Yield point elongation due to twinning in a magnesium alloy. *Acta Materialia*, vol. 60, no. 4, p. 1433-1443, **DOI:10.1016/j.actamat.2011.11.022**.

[15] Hallai, J.F., Kyriakides, S. (2013). Underlying material response for Lüders-like instabilities. *International Journal of Plasticity*, vol. 47, p. 1-12, **DOI:10.1016/j.ijplas.2012.12.002**.

[16] Khan, T., Rabinovitch, M., Stohr, J.F., Trottier, J.P., Bibring, H. (1973). On the yield point phenomenon in composites. *Scripta Metallurgica*, vol. 7, no. 7, p. 727-730, **DOI:10.1016/0036-9748(73)90122-1**.

[17] Lu, J., Ravi-Chandar, K. (1999). Inelastic deformation and localization in polycarbonate under tension. *International Journal of Solids and Structures*, vol. 36, no. 3, p. 391-425, **DOI:10.1016/S0020-7683(98)00004-3**.

[18] Wu, T., Cao, Y., Yang, F., Xiang, M. (2014). Investigation on double yielding behavior under tensile loading in isotactic polypropylene. *Materials & Design*, vol. 60, p. 153-163, **DOI:10.1016/j.matdes.2014.03.044**.

[19] Burg, J.P., Harris, L.B. (1982). Tension fractures and boudinage oblique to the maximum extension direction: an analogy with lüders' bands. *Tectonophysics*, vol. 83, no. 3-4, p. 347-363, **DOI:10.1016/0040-1951(82)90027-0**.

[20] Watterson, J. (1999). The future of failure: stress or strain? *Journal of Structural Geology*, vol. 21, no. 8-9, p. 939-948, **DOI:10.1016/S0191-8141(99)00012-7**.

[21] Schwab, R., Ruff, V. (2013). On the nature of the yield point phenomenon. *Acta Materialia*, vol. 61, no. 5, p. 1798-1808, **DOI:10.1016/j.actamat.2012.12.003**.

[22] Wenman, M.R., Chard-Tuckey, P.R. (2010). Modelling and experimental characterisation of the Lüders strain in complex loaded ferritic steel compact tension specimens. *International Journal of Plasticity*, vol. 26, no. 7, p. 1013-1028, **DOI:10.1016/j.ijplas.2009.12.005**.

[23] Aguirre, F., Kyriakides, S., Yun, H.D. (2004). Bending of steel tubes with Lüders bands. *International Journal of Plasticity*, vol. 20, no. 7, p. 1199-1225, **DOI:10.1016/j.ijplas.2003.05.001**.

[24] Hallai, J.F., Kyriakides, S. (2011). On the effect of Lüders bands on the bending of steel tubes. Part I: Experiments. *International Journal of Solids and Structures*, vol. 48, no. 24, p. 3275-3284, **DOI:10.1016/j.ijsolstr.2011.06.024**.

[25] Zou, T., Li, D., Wu, G., Peng, Y. (2016). Yield strength development from high strength steel plate to UOE pipe. *Materials & Design*, vol. 89, p. 1107-1122, **DOI:10.1016/j.matdes.2015.10.095**.

[26] Žerovnik, A., Pepel, V., Prebil, I., Kunc, R. (2016). The yield-point phenomenon and cyclic plasticity of the uniaxially loaded specimens. *Materials & Design*, vol. 92, p. 971-977, **DOI:10.1016/j.matdes.2015.12.111**.

[27] Hahn, G.T. (1962). A model for yielding with special reference to the yield-point phenomena of iron and related

bcc metals. *Acta Metallurgica*, vol. 10, no. 8, p. 727-738, **DOI:10.1016/0001-6160(62)90041-X**.

[28] Johnston, W.G., Gilman, J.L. (1959). Dislocation velocities, dislocantion densities and plastic flow in lithium floride crystals. *Journal of Applied Physics*, vol. 30, no. 2, p. 129, **DOI:10.1063/1.1735121**.

[29] Shioya, T., Shioiri, J. (1976). Elastic-plastic analysis of the yield process in mild steel. *Journal of the Mechanics and Physics of Solids*, vol. 24, no. 4, p. 187-204, **DOI:10.1016/0022-5096(76)90002-8**.

[30] Itoh, M., Yoshida, F., Yamashita, Y., Ohmori. M. (1992). FEM Analysis for Nonuniform Yielding Processes in Mild Steel Plates under Stretching. *JSME International Journal Ser. 1, Solid Mechanics, Strength of Materials*, vol. 35, no. 1, p. 70-77, **DOI:10.1299/jsmea1988.35.1_70**.

[31] Armstrong, P.J., Frederick, C.O. (1966). *A Mathematical Representation of the Multiaxial Bauschinger Effect*. Central Electricity Generating Board, Berkeley Nuclear Laboratories, Berkley.

[32] Chaboche, J.L., Gaubert, A., Kanouté, P., Longuet, A., Azzouz, F., Mazière, M. (2013). Viscoplastic constitutive equations of combustion chamber materials including cyclic hardening and dynamic strain aging. *International Journal of Plasticity*, vol. 46, p. 1-22, **DOI:10.1016/j.ijplas.2012.09.011**.

[33] Chaboche, J.L. (1986). Time-independent constitutive theories for cyclic plasticity. *International Journal of Plasticity*, vol. 2, no. 2, p. 149-188, **DOI:10.1016/0749-6419(86)90010-0**.

[34] Chaboche, J.L. (1989). Constitutive equations for cyclic plasticity and cyclic viscoplasticity. *International Journal of Plasticity*, vol. 5, no. 3, p. 247-302, **DOI:10.1016/0749-6419(89)90015-6**.

[35] Abdel-Karim, M., Ohno, N. (2000). Kinematic hardening model suitable for ratchetting with steady-state. *International Journal of Plasticity*, vol. 16, no. 3-4, p. 225-240, **DOI:10.1016/S0749-6419(99)00052-2**.

[36] Abdel-Karim, M., Khan, A. (2010). Cyclic multiaxial and shear finite deformation responses of OFHC Cu. Part II: An extension to the KHL model and simulations. *International Journal of Plasticity*, vol. 26, no. 5, p. 758-773, **DOI:10.1016/j.ijplas.2009.10.008**.

[37] Abdel-Karim, M. (2009). Modified kinematic hardening rules for simulations of ratchetting. *International Journal of Plasticity*, vol. 25, no. 8, p. 1560-1587, **DOI:10.1016/j.ijplas.2008.10.004**.

[38] Abdel-Karim, M. (2010). An evaluation for several kinematic hardening rules on prediction of multiaxial stress-controlled ratchetting. *International Journal of Plasticity*, vol. 26, no. 5, p. 711-730, **DOI:10.1016/j.ijplas.2009.10.002**.

[39] Abdel-Karim, M. (2010). An extension for the Ohno–Wang kinematic hardening rules to incorporate isotropic hardening. *International Journal of Pressure Vessels and Piping*, vol. 87, no. 4, p. 170-176, DOI:10.1016/j.ijpvp.2010.02.003.

[40] Yu, D., Chen, G., Yu, W., Li, D., Chen, X. (2012). Visco-plastic constitutive modeling on Ohno–Wang kinematic hardening rule for uniaxial ratcheting behavior of Z2CND18.12N steel. *International Journal of Plasticity*, vol. 28, no. 1, p. 88-101, **DOI:10.1016/j.ijplas.2011.06.001**.

[41] Pham, M.-S., Iadicola, M., Creuziger, A., Hu, L., Rollett, A.D. (2015). Thermally-activated constitutive model including dislocation interactions, aging and recovery for strain path dependence of solid solution strengthened alloys: *Application to AA5754-O. International Journal of Plasticity*, vol 75, p. 226-243, **DOI:10.1016/j.ijplas.2014.09.010**.

[42] Chaboche, J.L. (2008). A review of some plasticity and viscoplasticity constitutive theories. *International Journal of Plasticity*, vol. 24, no. 10, p. 1642-1693, **DOI:10.1016/j.ijplas.2008.03.009**.

[43] Ohno, N., Wang, J.D. (1993). Kinematic hardening rules with critical state of dynamic recovery, part I: formulation and basic features for ratchetting behavior. *International Journal of Plasticity*, vol. 9, no. 3, p. 375-390, **DOI:10.1016/0749-6419(93)90042-O**.

[44] Ohno, N., Wang, J.D. (1993). Kinematic hardening rules with critical state of dynamic recovery, part II: Application to experiments of ratchetting behavior. *International Journal of Plasticity*, vol. 9, no. 3, p. 391-403, **DOI:10.1016/0749-6419(93)90043-P**.

[45] Korelc, J., Skuber, P., Beg, D. (2004). *Derivation of Finite Strain Damage Model for Simulation of Low-Cycle Fatigue of Steel Structures. Computational Mechanics*. Tsinghua University Press, Beijing, p. 264.

[46] Žerovnik, A., Kunc, R., Prebil, I. (2010). Yield-point phenomenon in constitutive models of cyclic plasticity. *Computational Materials Science*, vol. 49, no. 3, p. 473-482, **DOI:10.1016/j.commatsci.2010.05.038**.

[47] Yoshida, F., Kaneda, Y., Yamamoto, S. (2008). A plasticity model describing yield-point phenomena of steels and its application to FE simulation of temper rolling. *International Journal of Plasticity*, vol. 24, no. 10, p. 1792-1818, **DOI:10.1016/j.ijplas.2008.05.004**.

[48] Yoshida, F. (2000). A constitutive model of cyclic plasticity. *International Journal of Plasticity*, vol. 16, no. 3-4, p. 359-380, **DOI:10.1016/S0749-6419(99)00058-3**.

[49] Kunc, R., Zerovnik, A., Prebil, I. (2007). Verification of numerical determination of carrying capacity of large rolling bearings with hardened raceway. *International Journal of Fatigue*, vol. 29, no. 9-11, p. 1913-1919, **DOI:10.1016/j.ijfatigue.2007.02.003**.

[50] Krishna, S., Hassan, T., Ben Naceur, I., Saï, K., Cailletaud, G. (2009). Macro versus micro-scale constitutive models in simulating proportional and nonproportional cyclic and ratcheting responses of stainless steel 304. *International Journal of Plasticity*, vol. 25, no. 10, p. 1910-1949, **DOI:10.1016/j.ijplas.2008.12.009**.

[51] Franulovic, M., Basan, R., Prebil, I. (2009). Genetic algorithm in material model parameters' identification for low-cycle fatigue. *Computational Materials Science*, vol. 45, no. 2, p. 505-510, **DOI:10.1016/j.commatsci.2008.11.012**.

[52] Instron (2008). *Instron 8800 Servohydraulic Testing Systems*. Instron, Norwood.

[53] Korelc, J. (1997). Automatic generation of finite-element code by simultaneous optimization of expressions. *Theoretical Computer Science*, p. 187, no. 1-2, p. 231-248, **DOI:10.1016/S0304-3975(97)00067-4**.

Strojniški vestnik - Journal of Mechanical Engineering 63(2017)9, 489-500

DOI:10.5545/sv-jme.2017.4430 Original Scientific Paper
Received for review: 2017-03-03
Received revised form: 2017-05-09
Accepted for publication: 2017-06-16

Application of a Force Model Adapted for the Precise Turning of Various Metallic Materials

Richárd Horváth* – Judit Lukács
Óbuda University, Donát Bánki Faculty of Mechanical and Safety Engineering, Hungary

The knowledge of cutting forces is critical. They might affect the load of the machine and, in the case of fine turning, the deformation of thin and slim workpieces. The generated forces depend not only on material properties (hardness, tensile strength) and on cutting parameters, but also on the tool edge geometry, that strongly determines the geometry of the chip (thickness and width). This article deals with the application of a force model adapted for precise turning technology. Three different types of materials widely used in mass production were taken into consideration (C45 and KO36 steel types and AS12 die-cast aluminium alloy). The components of cutting force were measured in three directions (F_c, F_f, F_p) and the specific cutting forces were calculated. The main values of specific cutting forces were introduced for precision turning ($k_{1,0.1}$); using this, a new force model was constructed based on the theoretical parameters of the non-deformed chip cross-section (h_{eq} is equivalent chip thickness and l_{eff} effective length of the edge of the tool) in case of all three examined materials. Investigations revealed that the influence of l_{eff} on specific cutting force components is not negligible; however, it has the least effect on k_c and is the most influential in case of k_p. The errors of the constructed new force models follow Gaussian distribution with low values of standard deviation. Thereby, the models can be applied to estimate cutting force components during the technological process planning procedure with adequate accuracy.
Keywords: fine turning, force model, force measurement, specific cutting force

Highlights
- *New predictive models were determined to estimate cutting force components while fine turning.*
- *Novel geometric parameters of the chip cross-section were introduced.*
- *The main values of specific cutting forces characterizing fine turning technology were theoretically calculated.*
- *The applicability of the equations for each material used was investigated by residuals.*

0 INTRODUCTION

The cutting force has a significant effect on the geometry and tolerances (e.g. circularity, deviation of circular shape or cylindricity, ovality, conical surfaces) of the workpiece (especially in the case of thin and slim parts), which are key criteria for the products. Moreover, they also affect the tool wear process. Due to the development of technology, the new tool (coatings) and workpiece materials require the exact knowledge of the cutting forces, their investigation during turning is an important field of cutting studies. In the case of turning, the kinetic conditions of which can be seen in Fig. 1, a spatial force system is generated.

A new frictional model was constructed by Rusinek et al. [1] in case of orthogonal cutting that took the forces acting on the tool face as well as on the tool flank into consideration. Furthermore, the influence of the tool flank forces on system dynamics was studied.

The mathematical modelling of cutting processes can be based on two methods: creating mechanical or phenomenological models. In recent years, several researchers have investigated the machinability of different types of materials, dealt with optimizing, measuring, and calculating cutting forces.

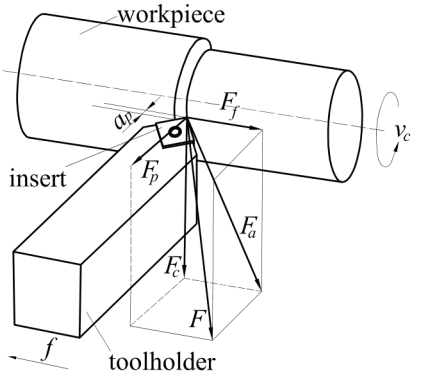

Fig. 1. *The kinetic conditions of turning and the generated spatial force system*

The investigation of the machinability of different types of steel is still a basic field of cutting studies.

Kulkarni et al. [2] carried out cutting tests on AISI304 austenite stainless steel by using AlTiCrN coated inserts. In their experimental runs, the depth of cut was held at a constant value (a_p = 1 mm), the limits of the other cutting parameters were v_c = 140 m/min to 320 m/min; f = 0.08 mm to 0.26 mm. The generated forces and the cutting temperature were studied. They said that regarding the force components, the effect of the feed was the most significant; however, the influence of cutting speed was negligible. In contrast,

*Corr. Author's Address: Óbuda University, Donát Bánki Faculty of Mechanical and Safety Engineering, Institute of Materials and Manufacturing Sciences, Népszinház str. 8., Budapest, 1081 Hungary, horvath.richard@bgk.uni-obuda.hu

that was the cutting speed had the greatest impact on the value of the cutting temperature.

Čep et al. [3] investigated the machinability of 13MoCrV6 and C45 steels with two different types of Si3N4 based ceramic inserts (Tungaloy: FX105, CX710) in the case of interrupted machining.

Suresh et al. [4] examined the generated forces on AISI4340 steel with CVD coated (TiC/Ti/CN/Al_2O_3) inserts. They created linear equations on calculating the resultant cutting force and the specific cutting force. The feed was declared to be the most significant factor, and the depth of cut was at the second position; however, the cutting speed was the least influential regarding the cutting forces.

López de Lacalle et al. [5] carried out high-speed milling cutting studies on inclined surfaces. Two types of steels (hardness: 30 and 50 HRC) were investigated when using sintered tungsten carbide ball end mills with TAlN coating. It was stated, that upmilling produces smaller deflection errors than downmilling does. In addition, average surface roughness values were higher in the case of 50 HRC steel. Moreover, average surface roughness slightly increased with slope.

Cukor and Jurković [6] tested the cutting ability of DIN Ck45 steel in the case of dry turning with coated tool. Cutting forces, surface roughness, and tool wear were measured as a function of cutting parameters (v_c, f, a_p). They determined a context among the set cutting parameters and the measured ones with the help of a genetic algorithm.

Multi-objective optimization is a key industrial question. Singaravel and Selvaraj [7] studied the problem mentioned in the case of turning EN 25 steel with coated carbide tools. Two methods (technique for order preference by similarity to ideal solution (TOPSIS) and analytic hierarchy process (AHP)) were combined to simultaneously minimize the micro-hardness and surface roughness of the cut surface and to maximize the material removal rate. Nevertheless, their combined method (TOPSIS and AHP) could determine the optimum cutting parameters.

Selvaraj et al. [8] examined two types of duplex stainless steel (DSS ASTM A 995 grade 5A – hardness: 223 HB and grade 4A – hardness: 212 HB) in case of dry turning. Feed and cutting speed were varied; in contrast, depth of cut was chosen to be held at a constant value. The influence of cutting parameters was measured on the generated forces, cut surface roughness, and tool wear. It was stated that feed is the most important factor in case of cutting forces and surface roughness (to an extent depending on the workpiece material); in contrast, cutting speed was found significant only in the case of tool wear. Optimum cutting parameters were determined for both materials, for which cutting forces and surface roughness were minimized.

Puh et al. [9] also defined the optimal parametric combination for turning processes. Their experiments were carried out on Ck45 steel with coated carbide insert under dry conditions. The Grey-Based Taguchi method was applied to minimize average surface roughness and to maximize material removal rate. It was stated that the cutting speed and depth of cut were two parameters significantly influencing the Grey relational grade. In addition, the depth of cut was the most effective factor in the performance.

Hassine et al. [10] presented a further multi-objective optimization in turning. The objective functions of their case study were to minimize production time, cost, and energy consumption.

Hard turning (turning of hardened steel types) requires special technology and tools. Carrying out studies in that field is currently very popular.

Karpuschewski et al. [11] analysed the influence of the microgeometry of the tool-on-tool wear in the case of hard turning. They used two types of ceramic insert (TiN coated and non-coated ones). Pairs of cutting speed-feed values were defined based on the measured force components (F_c, F_f, F_p) to prevent tool edge chipping and sudden loss of cutting performance.

Nayak and Sehgal [12] investigated the machinability of AISI D6 (54±2 HRC) steel while hard turning. Their experiment was carried out by using three types of CBN tools. During the experimental runs, the main cutting force, the thrust force, the temperature of the edge of the tool, and the cut surface roughness were measured. Regarding the value of the main cutting force, the influence of feed was the most significant; however, the effect of cutting speed was declared infinitesimal.

El Hakim et al. [13] carried out cutting studies on a high-alloy tool steel (AISI T15; hardness: ≈ 52 HRC) using a multilayer coated (TiC/TiCN/Al_2O_3) tool by hard turning. It was argued that over a certain cutting speed (v_c ≈ 40 m/min) the cutting force components barely depend on the cutting speed (the values are a bit lowered because of the annealing caused by the high cutting speed).

Kundrák et al. [14] examined the change of the microhardness of the hard-turned cut surface. As the literature showed, the values of the cutting force do not directly influence the hardness of the cut surface. However, indirectly, by the transformation of the mechanical energy into thermal energy, the generated forces affect the hardness of the surface.

Chen et al. [15] cut GCr15 (hardness: 60 HRC) bearing steel. In their tests, the values of cutting speed and feed were varied; however, depth of cut was held constant. All three force components were measured. It was determined that feed was the most significant factor on the values of the force and on the surface roughness. Having raised the value of feed, both these parameters had increased.

Meddour et al. [16] examined AISI 52100 steel (hardness: 59 HRC) in the case of hard turning. Ceramic inserts were used with different values of nose radius. Their studies were focused on the cutting forces and the cut surface roughness. An empirical model was created in order to estimate the cutting forces as a function of the systematically varied cutting parameters. Regarding the generated forces, depth of cut was the most significant factor; feed was also important. In contrast, the effect of cutting speed was negligible.

Wojciechowski et al. [17] examined ball-end milling of hardened steel (55NiCrMoV6 – hardness: ~ 55 HRC). A monolithic sintered tungsten carbide ball end mill with TiAlN coating was chosen to study cutter's displacements and cutting force components in case of different surface inclinations (0°, 30°, 60°). The increased values of both feed per tooth and depth of cut resulted in higher values of cutting forces and tool's deflections. Nevertheless, in the case of lower values of cutting parameters, meaning smaller cross-sections, maximal normal force was significantly lower. In addition, maximal normal force was higher when slot milling than when upward ramping (60°).

Moreover, the generated edge forces were analysed by Wojciechowski et al. [18] in case of ball milling of hardened steel (55NiCrMoV6). Monolithic sintered carbide ball end mills with TiAlN were used. The effect of surface inclination and progressive flank wear on edge forces was examined. It was proved that uncut chip thickness had the greatest influence on edge forces. During use, worn tool radial forces are higher than tangential ones. Regarding surface inclination, the highest force components were detected in the case of slot milling.

Further cutting studies [19] were carried out in case of cylindrical end milling of the same material. Monolithic tools were used with TiAlN coating. Cutter's displacements resulted from radial run out that is also generated by cutting forces. Radial run out was measured off-line. The model, developed for estimating surface roughness parameters, included dynamic tool displacements. Two different mechanisms of surface irregularity formation were determined.

An example of hard turning technology and its power relations is shown by Zębala and Kowalczyk [20] by using a polycrystalline diamond tool (PCD). Three different types of raw materials were investigated, the difference in whose was the amount of Co (10, 15, and 25 volume %). In the cases of being alloyed with 15 and 25 volume % Co, no significant deviation was found regarding the cutting forces.

As engineering plastics (non-reinforced and reinforced ones, as well polymer composites) are gaining popularity, several researchers are testing their machinability.

Mata et al. [21] were studying the cutting ability of polyether ether ketone (PEEK) reinforced with 30 % carbon fibre.

Hanafi et al. [22] also examined PEEK CF30. Dry turning conditions and TiN coated insert were chosen. In their experiments both three components of the cutting force were measured, the resultant cutting force and the specific forces were calculated. Empirical models were generated for the calculated values with the help of response surface methodology (RSM) and fuzzy algorithm. The application of the methods was compared.

Fetecau and Stan [23] turned two types of polytetrafluorethylene (PTFE) based composites: PTFE CG 32-3 (32 % carbon, 3 % graphite) and PTFE GR 15 (15 % regenerated graphite). In their experimental runs, cutting parameters (v_c, f, a_p) were changed; furthermore, three polycrystalline diamond tools (PCD) were used having different nose radii. It was stated that the generated forces depend primarily on feed and depth of cut; however, the main cutting force gives a nearly constant value as a function of cutting speed and tool nose radius. In the case of each material, predictive models were defined, consisting only of the main effects.

The application of light metals, as a reason of their advantageous qualities, is showing a growing trend in the past decades. The investigation of these materials and their alloys is an important research field.

Joardar et al. [24] dry turned SiC metal matrix composites with a PCD tool. An empirical model was determined to estimate cutting forces, in which not only cutting parameters were input parameters but also the amount of Si.

Çolak [25] determined optimum cutting parameters of turning of Ti6Al4V titanium alloy with conventional and high pressure assisted cooling conditions by a genetic algorithm. The optimization was carried out with empirical equations regarding three factors: cut surface roughness, material removal

rate, and machining performance. Tool wear was also examined. The longest tool life resulted from the highest cooling pressure.

De Augustina et al. [26] carried out turning studies on aluminium alloy UNS A97075 under dry conditions. Having used tools with different nose radii, cutting force components were measured. It was stated that in the case of low feed values both tools provided similar forces.

Horváth et al. [27] dealt with the machinability of aluminium in the case of fine turning. The cutting ability of two types of widely used dye-cast alloys (AS12 – eutectic and AS17 – hyper-eutectic alloys) was investigated by using five different diamond tools. Phenomenological models were generated to estimate surface roughness, depending on input cutting parameters (v_c, f, a_p), as well as on workpiece and tool edge materials as qualitative factors [28]. In contrast, the statistical parameters of cut surface roughness (*Rsk* – skewness; *Rku* – kurtosis) were examined. It was stated that those are independent of cutting parameters and are only functions of the tool edge geometry [29]. In addition, a dynamometer was constructed especially for measuring small force components (0 N to 100 N) [30]. A new force model for fine turning was also determined [31].

Regarding non-conventional cutting technologies, it is very important to know cutting forces and be able to typify them exactly.

Venkatesan et al. [32] give an overview of laser assisted machining (LAM) and disclose some options of the future development of the technology. Using the method of localized heating, cutting forces and tool wear can be reduced, however the quality of the surface and the amount of the removed material can be increased.

Further investigations are needed to determine cutting forces if kinematic, geometrical, and technological relations differ from conventional longitudinal turning.

Kundrák et al. [33] made an analysis of rotational turning (where an extremely high material removal rate can be achieved). Geometrical parameters of chip cross-section and cutting parameters were defined.

As mentioned above, in recent years, several researchers dealt with generating predictive models in order to estimate cutting forces. A wide range of methods was applied: creating linear equations, empirical models, using genetic algorithms, fuzzy logic, and the response surface method. In contrast, only a few studies provided mathematical formulae for predicting all three force components. Furthermore, most of the models operated with cutting parameters, raw material, etc.

In contrast to these studies, in this article, the authors show the application of a force model adapted for precise turning when the chip removal process primarily befalls on the tool nose radius. Consequently, novel geometric features of the non-deformed chip cross-section were introduced (h_{eq} and l_{eff}), based on both cutting parameters (a_p, f) and tool geometry (κ_r, r_ε). With the help of these parameters, equations were developed to estimate cutting force components (F_c, F_f, F_p). However, the models are based on the widely known Kienzle-Victor formula [34], by h_{eq} and l_{eff} the characteristics of precision turning are taken into consideration. The applicability and expansibility of the new force model adapted for fine turning were proved in the case of three different types of raw materials (C45 – non-alloy steel, KO36 – stainless steel, AS12 – die-cast eutectic aluminium alloy).

1 MATERIALS AND METHODS

1.1 Materials Used

The experimental runs were carried out on three widely used materials those technological properties are however significantly different.

A generally used non-alloy steel (C45, 1.0503) was chosen that is appropriate for heat treatments. It is a material for products (vehicular and other engineering parts) being loaded with low and medium stress (tools, wear-proof parts). The chemical composition in weight % is the following: C = 0.42 to 0.5; Si ≤ 0.4; Mn = 0.5 to 0.8; P ≤ 0.045; S ≤ 0.045; Cr ≤ 0.4; Mo ≤ 0.1; Ni ≤ 0.4; Cr+Ni+Mo ≤ 0.63.

The second material was an austenite stainless steel (KO36, 1.4541), which is one of the most widely used materials in the industrial technology because of its excellent weldability and machinability. It is typically used for products those face an increased level of mechanical and chemical load (food-, milk- and chemical industry, containers, bottles). Moreover, the arms and aerospace industries use the alloy. The chemical composition in weight% is: C ≤ 0.8; Si ≤ 1; Mn ≤ 2; Cr = 17 to 19; Ni = 9 to 12.

Finally, our experiments were carried out on a die-cast eutectic aluminium alloy (AS12) that has excellent mechanical and technological properties moreover, its castability is quite good. Its typical areas of use are vehicular and engineering mass products. AS12 is composed of: Si = 12.2 to 13.2; Fe = 0.35 to

0.55; Cu ≤ 0.04; Mn ≤ 0.09; Mg ≤ 0.04; Ni ≤ 0.04; Zn ≤ 0.09; Ti ≤ 0.09 in weight %.

1.2 Tools Used

The non-alloy steel (C45) was cut with a CVD-coated (TiN/TiCN/Al2O3/TiN) carbic insert. Code: DCMT 11T304 FG TT8115 CVD, manufacturer: TaeguTec. In the case of the stainless steel (KO36), a non-coated CerMet insert was used. Code: DCMT 11T304 PC CT3000, manufacturer: TaeguTec. The cutting studies of the die-cast aluminium alloy (AS12) were carried out with a non-coated sintered carbide insert (Code: DCGT 11T304 FL K10, manufacturer: TaeguTec).

1.3 Machines, Devices Used

Cutting tests were carried out on a Dugard Eagle BNC 1640 CNC lathe (P_{max} = 11 kW, spindle speed: 100 l/min to 4500 1/min). The cutting force components were measured by a dynamometer system which is based on a modified tool holder (its exploded view is shown in Fig. 2), developed by the author [30] especially in order to be able to determine the cutting forces during fine turning those are expected to be relatively small. The tool holder that is suitable to measure each force component was combined with a KISTLER 5019 Multichannel Charge Amplifier. The sampling rate was 2000 Hz. The sensitivity of the constructed dynamometer (see Fig. 2.) depending on the directions of the measured force components are: –3.463 pC/N for F_c; –7.47 pC/N for F_f and –7.05 pC/N for F_p. The exact values of the cutting forces were evaluated by DynoWare Software.

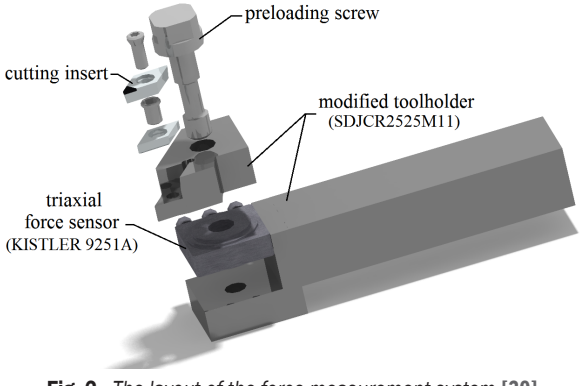

Fig. 2. *The layout of the force measurement system* [30]

1.4 Force Model Adapted for Fine Turning Technologies

A widely, even in industrial estimations used force model is the Kienzle-Victor equation, Eq. (1) [34] that is based on the geometrical parameters of the chip cross-section (chip thickness and width, see Fig. 3).

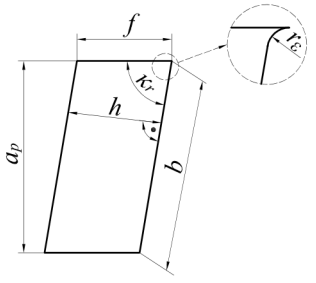

Fig. 3. *Chip cross-section for the Kienzle-Victor model*

Those can be easily calculated from the feed, the depth of cut and the side cutting edge angle (see Eqs. (1) and (2)). The removed chip cross- section can be defined by Eq. (3).

$$b = \frac{a_p}{\sin \kappa_r}, \tag{1}$$

$$h = f \cdot \sin \kappa_r, \tag{2}$$

$$A = a_p \cdot f = b \cdot h. \tag{3}$$

In the Kienzle-Victor model, specific cutting force was introduced (in the direction of the main cutting force) as the ratio of the main cutting force and the removed chip cross-section (see Eq. (4)).

$$k_c = \frac{F_c}{A}. \tag{4}$$

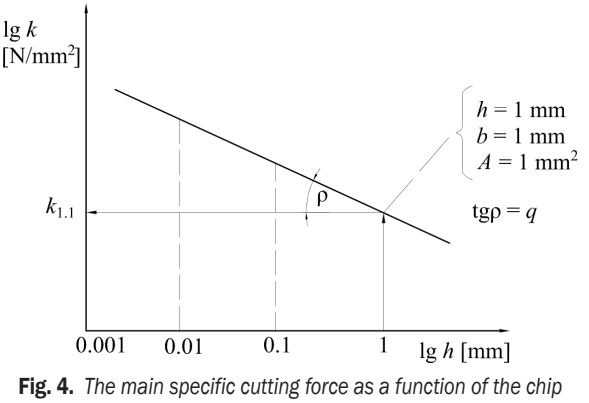

Fig. 4. *The main specific cutting force as a function of the chip thickness on a logarithmic scale chart (based on* [34])

As the specific cutting force depends strongly on the chip thickness [34] (Fig. 4), Kienzle and Victor determined the main value of the specific cutting force in their model (see Eq. (5)), where b = 1 mm; h = 1 mm; A = 1 mm^2.

$$k_c = \frac{k_{c1.1}}{h^{q_c}}. \quad (5)$$

The cutting force model of Kienzle-Victor for the main cutting force can be seen in Eq. (6) [34]:

$$F_c = k_c \cdot A = \frac{k_{c1.1}}{h^{qc}} \cdot b \cdot h = k_{c1.1} \cdot h^{1-q_c} \cdot b. \quad (6)$$

The Eq. (6) is appropriate for estimating the main cutting force in case of rough turning, where the effect of the nose radius on the chip cross-section is neglected (see Fig. 3).

However, in the case of fine turning, when the chip removal takes places primarily not on the side cutting edge, but also on the nose radius ($a > r_\varepsilon$) or only on the nose radius ($a << r_\varepsilon$), the above-mentioned Kienzle-Victor model cannot be used. The geometry of the chip cross-section, shown on Fig. 5, is significantly different, as the removed chip is relevantly smaller than in the case of roughing. Therefore, new parameters must be introduced, instead of chip thickness and width, to characterise the chip cross-section of fine turning.

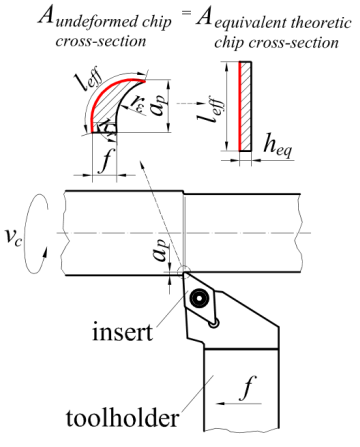

Fig. 5. *Chip cross-section in case of fine turning*

Cutting on or near the nose radius, using the new parameters of the chip cross-section is well-founded. Theoretical chip width, the so called effective cutting length can be calculated according to Eq. (7) [35].

$$l_{eff} = \frac{a_p - r_\varepsilon \cdot (1 - \cos\kappa_r)}{\sin\kappa_r} + r_\varepsilon \cdot \left(\kappa_r + \arcsin\frac{f}{2 \cdot r_\varepsilon} \right). \quad (7)$$

From the removed cross-section equivalent, chip thickness can be defined (see Eq. (9)).

$$A = a_p \cdot f = l_{eff} \cdot h_{eq}, \quad (8)$$

$$h_{eq} = \frac{A}{l_{eff}} = \frac{a_p \cdot f}{l_{eff}}. \quad (9)$$

The specific cutting forces (all three components) can be determined by Eq. (10) which is the extended version (for each three direction) of Eq. (4).

$$k = \frac{F}{A} = \frac{F}{a_p \cdot f} = \frac{F}{l_{eff} \cdot h_{eq}}. \quad (10)$$

It can be stated that the specific cutting forces depend, not obviously, on the removed chip cross-section (the same cross-section can be resulted by many different set cutting values). In contrast, those can be defined by the geometrical parameters (h_{eq} and l_{eff}). That is why the Kienzle-Victor equation extended by Horváth [31] is used, where the specific cutting force for fine turning can be calculated by Eq. (11).

$$k = C \cdot h_{eq}^q \cdot l_{eff}^y. \quad (11)$$

Furthermore, a contradiction can be found because regarding fine turning technologies a theoretical chip cross-section defined by l_{eff} = 1 mm and h_{eq} = 1 mm does not exist. Moreover, as chip thickness is reduced, the steepness of the increment of specific cutting force is not constant [36] and [37]. A new main value of the specific cutting force is to introduce ($k_{1,0.1}$), where l_{eff} = 1 mm and h_{eq} = 0.1 mm. In that case $k_{1,0.1}$ characterizing fine turning can be defined according to Eq. (12).

$$k_{1.0,1} = C \cdot h_{eq}^q \cdot l_{eff}^y = C \cdot 0.1^q \cdot 1^y = C \cdot 0.1^q = C \cdot 10^{-q}, \quad (12)$$

$$C = \frac{k_{1.0,1}}{0,1^q} = \frac{k_{1.0,1}}{10^{-q}} = k_{1.0,1} \cdot 10^q. \quad (13)$$

The cutting force model (see Eq. (14)) is determined by using Eqs. (11) and (13) [31]:

$$F = k \cdot A = k \cdot h_{eq} \cdot l_{eff} = k_{1.0,1} \cdot 10^q \cdot h_{eq}^{1+q} \cdot l_{eff}^{1+y}. \quad (14)$$

1.5 Cutting Studies

The experiment was built to involve the whole technological spectrum of fine turning. To this end feed was varied in seven (f = 0.03 mm to 0.15 mm) and depth of cut in three levels (a_p = 0.25 mm to 0.7 mm). Experimental runs are shown in Table 1 with their set cutting and geometrical parameters.

As a result of the value of tool nose radius (r_ε = 0.4 mm) in the case of the highest depth of cut (a_p = 0.7 mm) the chip removal befalls even on a short part of the side cutting edge. In contrast, at the lowest

level (a_p = 0.25 mm) it is only the nose radius that takes place in the chip formation.

Table 1. *Experimental runs*

Exp. runs	a_p [mm]	f [mm]	l_{eff} [mm]	h_{eq} [mm]	A [mm²]
1.	0.25	0.03	0.493	0.015	0.0075
2.	0.25	0.05	0.503	0.025	0.0125
3.	0.25	0.07	0.513	0.034	0.0175
4.	0.25	0.09	0.523	0.043	0.0225
5.	0.25	0.11	0.533	0.052	0.0275
6.	0.25	0.13	0.543	0.060	0.0325
7.	0.25	0.15	0.554	0.068	0.0375
8.	0.5	0.03	0.743	0.020	0.015
9.	0.5	0.05	0.753	0.033	0.025
10.	0.5	0.07	0.763	0.046	0.035
11.	0.5	0.09	0.774	0.058	0.045
12.	0.5	0.11	0.784	0.070	0.055
13.	0.5	0.13	0.794	0.082	0.065
14.	0.5	0.15	0.804	0.093	0.075
15.	0.7	0.03	0.944	0.022	0.021
16.	0.7	0.05	0.954	0.037	0.035
17.	0.7	0.07	0.964	0.051	0.049
18.	0.7	0.09	0.974	0.065	0.063
19.	0.7	0.11	0.984	0.078	0.077
20.	0.7	0.13	0.994	0.092	0.091
21.	0.7	0.15	1.004	0.105	0.105

Several researchers were studying the connection between cutting speed and the generated forces. It can be stated that the alteration of cutting speed has a negligible effect on cutting forces in comparison to feed and depth of cut **[12]**, **[13]**, **[16]**, **[23]**, **[38]** to **[40]**. Cutting tests were carried out with a constant cutting speed in case of each material. The set values are shown in Table 2.

Table 2. *Constant cutting speed values for each material*

Material	C45	KO36	AS12
v_c [m/min]	300	210	600

2 RESULTS

In the case of all three materials, the cutting force components were measured twice (F_c, F_f, F_p – see Fig. 1). The means are shown in Table 3.

2.1 Investigation of Specific Cutting Forces

The components of the specific cutting force were determined by Eq. (4). The constant values of the specific cutting force model adapted for fine turning (see Eq. (11)) were calculated by three parametric

Table 3. *Mean values of the cutting force components*

Exp. runs	C45			KO36			AS12		
	F_c [N]	F_f [N]	F_p [N]	F_c [N]	F_f [N]	F_p [N]	F_c [N]	F_f [N]	F_p [N]
1.	41.2	32.9	41.1	41.1	35.9	58.5	7.3	2.4	3.2
2.	50.9	36.0	50.2	53.8	37.9	60.9	10.7	3.1	4.0
3.	63.0	39.4	57.1	68.2	38.8	62.7	14.1	3.6	4.8
4.	70.2	42.0	63.8	75.0	42.5	66.2	16.8	4.0	5.5
5.	78.2	45.1	66.2	83.5	45.5	74.6	18.9	4.1	5.9
6.	88.4	49.0	71.6	92.5	50.8	76.9	21.1	4.4	6.3
7.	100.0	52.4	75.6	103.3	51.2	79.4	24.0	4.9	7.1
8.	70.0	72.3	44.9	75.6	82.3	56.3	14.0	5.8	2.8
9.	95.9	81.1	54.7	102.0	93.8	59.8	21.5	7.3	3.9
10.	125.5	89.2	63.8	128.3	102.2	62.2	28.5	8.6	4.9
11.	142.0	93.9	73.0	155.0	107.2	65.9	34.5	9.5	5.2
12.	160.8	103.5	82.2	170.8	110.2	67.5	39.8	10.3	5.8
13.	183.5	108.6	87.1	196.4	113.6	70.0	44.1	10.5	6.0
14.	198.2	114.5	92.3	222.8	118.4	74.1	48.3	10.8	6.3
15.	90.7	92.4	40.9	105.0	137.5	44.4	19.3	8.3	2.7
16.	124.0	109.0	51.4	145.8	169.8	49.2	29.8	11.3	3.8
17.	167.0	122.0	59.7	195.4	184.9	51.3	37.8	13.0	4.6
18.	185.0	134.9	70.5	219.3	197.4	53.8	45.0	14.1	5.1
19.	216.2	148.4	80.7	265.3	208.0	55.3	51.9	14.7	5.6
20.	246.0	154.3	89.7	293.0	215.0	58.9	58.5	14.8	5.8
21.	278.0	162.4	94.8	315.5	225.0	64.9	67.2	15.9	5.9

Table 4. The constant values of the specific cutting force model Eq. (11)

	k_c			k_f			k_p		
	c_c	q_c	y_c	c_f	q_f	y_f	c_p	q_p	y_p
C45	982	–0.408	0.094	268	–0.764	0.591	238	–0.557	–1.121
KO36	1193	–0.390	0.260	322	–0.820	1.155	98	–0.810	–1.370
AS12	358	–0.259	0.125	39	–0.635	0.751	22	–0.442	–1.542

power function regression. Table 4 shows the materials and the connecting constants.

Regarding the specific cutting force components (k_c, k_p, k_f), taking the appropriate values from Table 4 and substituting them into Eq. (11) results in a difference within ±10 % between the measured and calculated values, in the case of all three materials.

As regards both components, the main values of the specific cutting forces can be defined within the technological limits of fine turning. That means a theoretical chip cross-section, where h_{eq} = 0.1 mm and l_{eff} = 1 mm (see Table 5). By using these parts, cutting force components can be calculated easily (see Eqs. (15) to (23)).

Table 5. *Main values of the specific cutting forces in case of fine turning*

	C45	KO36	AS12
$k_{c1,0.1}$	2513	2928	650
$k_{f1,0.1}$	1556	2127	168
$k_{p1,0.1}$	858	633	61

Fig. 6. shows the components of the specific cutting force, as a function of the equivalent chip thickness (h_{eq}) and the theoretical cutting length (l_{eff}) on logarithmic scale charts. In comparison to the Kienzle-Victor model (see Fig. 4), in the case of fine turning, specific cutting force values depend on the thickness of the removed chip; however, the influence of the effective cutting length is also significant (especially regarding feed and thrust force components). Consequently, the Kienzle-Victor equation has to be extended Eq. (11), so the new model takes into consideration both geometrical parameters of the theoretical chip cross-section (h_{eq} and l_{eff}).

2.2 Cutting Force Models

Having determined the main values of the specific cutting force for fine turning (Tables 4 and 5), the generated forces can be calculated for each material and each direction. The force models are as follows:

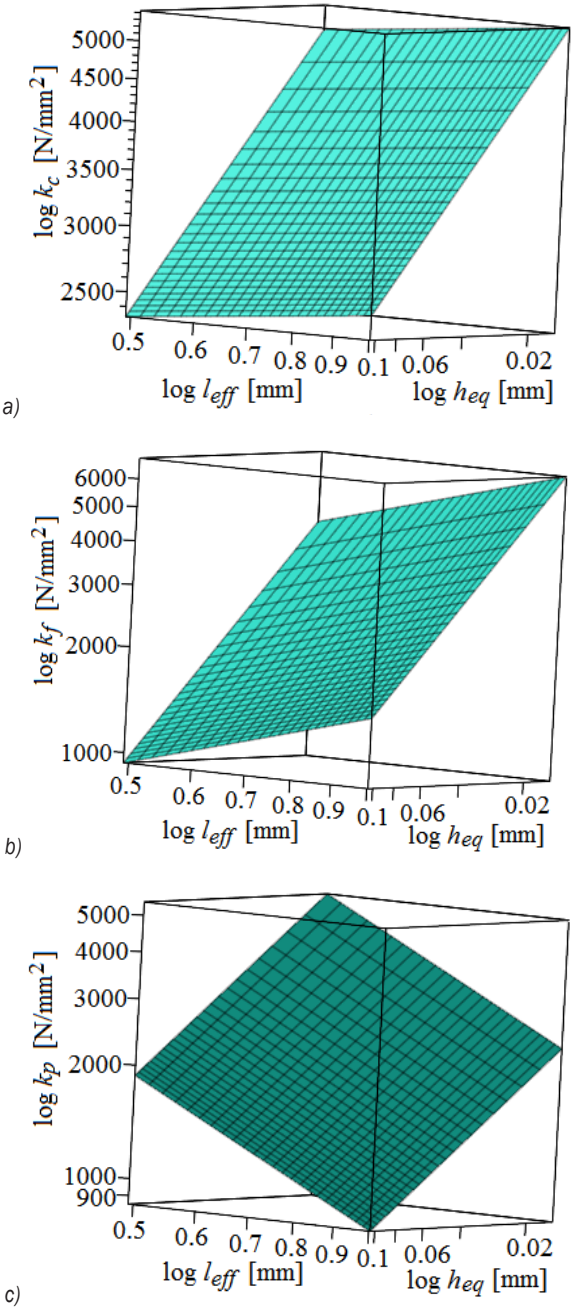

Fig. 6. *The specific cutting force components as a function of equivalent chip thickness and effective cutting length (in case of C45); a) in the directions of F_c, b) in the directions F_f, and c) in the directions F_p*

$$F_{c\_C45} = 2513 \cdot 10^{-0.408} \cdot h_{eq}^{0.592} \cdot l_{eff}^{1.094}, \quad (15)$$

$$F_{f\_C45} = 1556 \cdot 10^{-0.764} \cdot h_{eq}^{0.236} \cdot l_{eff}^{1.591}, \quad (16)$$

$$F_{p\_C45} = 858 \cdot 10^{-0.557} \cdot h_{eq}^{0.443} \cdot l_{eff}^{-0.121}, \quad (17)$$

$$F_{c\_KO36} = 2928 \cdot 10^{-0.390} \cdot h_{eq}^{0.610} \cdot l_{eff}^{1.260}, \quad (18)$$

$$F_{f\_KO36} = 2127 \cdot 10^{-0.820} \cdot h_{eq}^{0.180} \cdot l_{eff}^{2.155}, \quad (19)$$

$$F_{p\_KO36} = 633 \cdot 10^{-0.810} \cdot h_{eq}^{0.190} \cdot l_{eff}^{-0.370}, \quad (20)$$

$$F_{c\_AS12} = 650 \cdot 10^{-0.259} \cdot h_{eq}^{0.741} \cdot l_{eff}^{1.125}, \quad (21)$$

$$F_{f\_AS12} = 168 \cdot 10^{-0.635} \cdot h_{eq}^{0.365} \cdot l_{eff}^{1.751}, \quad (22)$$

$$F_{p\_AS12} = 61 \cdot 10^{-0.442} \cdot h_{eq}^{0.558} \cdot l_{eff}^{-0.542}. \quad (23)$$

2.3 Examination of the Model

Fig. 7 shows residuals of the measured and calculated values of the force components. It was stated that the deviations follow normal distribution, and their expected values are nearly zero. Furthermore, each force model (see Eqs. (15) to (23)) provides an adequate accuracy (within a deviation of 10 %), so those can be applied during the process planning procedure.

3 CONCLUSION

In this article, a force model adapted for fine turning was shown in the case of finishing of three widely used materials the technological properties of which are, however, significantly different. About the application of the model the conclusions are as follows:

- in case of fine turning, h chip thickness and b chip width are not proper to characterise the non-deformed chip cross-section, because it is primarily the nose radius that takes place in the chip formation. That is why new geometrical parameters are introduced: h_{eq} equivalent chip thickness and l_{eff} effective cutting length;
- it was proved that specific cutting forces in case of all three components are affected notably by l_{eff} and are not only a function of h_{eq} (especially in the

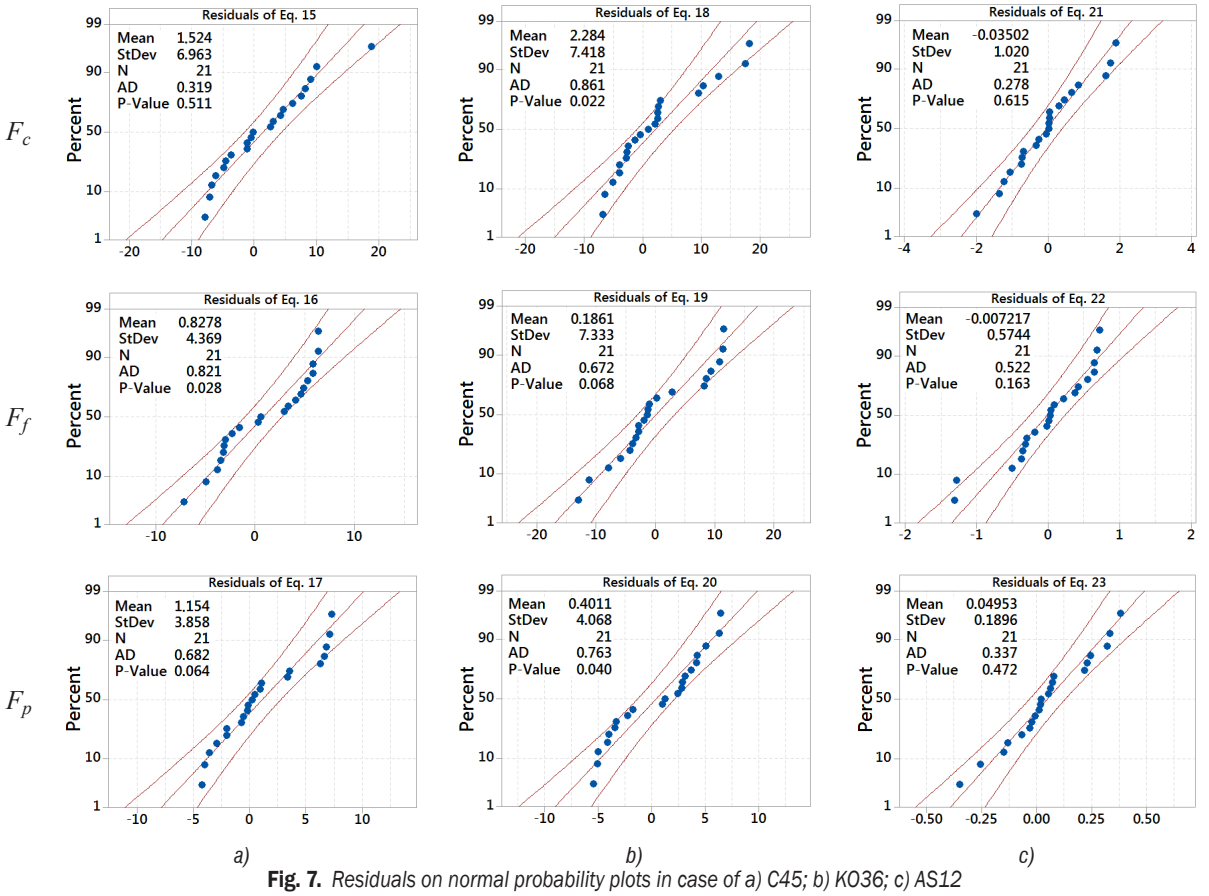

Fig. 7. *Residuals on normal probability plots in case of a) C45; b) KO36; c) AS12*

case of k_f and k_p). Consequently, both geometrical parameters are needed in the specific cutting force model (Eq. (11)) despite the Kienzle-Victor equation (the case of bigger chip cross-sections);

- the investigations revealed that specific cutting force components are affected by both theoretical parameters of chip cross-section (h_{eq} and l_{eff}). The effect of l_{eff} was the lowest on k_c and was the most influential in case of k_p (see Fig. 6);
- it was stated that the model adapted for fine turning forces can be used in the case of materials having technologically significantly different properties. Thus, the application of the equations is independent of the workpiece material;
- since in the case of fine turning the removed chip cross-section cannot be compared with the one used in the Kienzle-Victor model, a novel main value of the specific cutting force ($k_{1,0.1}$) was introduced for the technology instead of $k_{1.1}$. The main values of the specific cutting force were determined for each material and each direction ($k_{c1,0.1\_C45}$ = 2513 N/mm^2; $k_{f1,0.1\_C45}$ = 1556 N/mm^2; $k_{p1,0.1\_C45}$ = 858 N/mm^2; $k_{c1,0.1\_KO36}$=2928 N/mm^2; $k_{f1,0.1\_KO36}$ = 2127 N/mm^2; $k_{p1,0.1\_KO36}$ = 633 N/mm^2; $k_{c1,0.1\_AS12}$ = 650 N/mm^2; $k_{f1,0.1\_AS12}$ = 168 N/mm^2; $k_{p1,0.1\_AS12}$ = 61 N/mm^2);
- based on the specific cutting forces and the parameters of the undeformed chip cross-section (h_{eq} and l_{eff}) cutting force models were generated (in case of all three examined materials and each directions) with the help of which the components of the cutting force can be estimated. Moreover, the errors of force models follow normal distribution and their expected values are approximating zero;
- the above-mentioned models are adapted for precision turning when the chip removal process primarily takes place on the tool nose radius. The technological limits of fine turning where the generated force models are applicable is a_p = 0.25 mm to 0.7 mm; f = 0.03 mm to 0.15 mm;
- the constructed new force model is adapted to estimate the cutting forces in the case of precision turning that is useful in the technological process planning procedure to predict the generated force components with an adequate accuracy.

4 NOMENCLATURE

A	chip cross-section, [mm^2]
a_p	depth of cut, [mm]
AS12	die-cast eutectic aluminium alloy
b	chip width, [mm]
C, q, y	empirically defined constants of the specific cutting force model in case of fine turning
C45	non-alloy quality steel
f	feed, [mm]
F	resultant cutting force, [N]
F_c	main cutting force, [N]
F_f	feed force, [N]
F_p	thrust force, [N]
h	chip thickness, [mm]
h_{eq}	equivalent chip thickness, [mm]
$k_c; k_f; k_p$	specific cutting forces in the directions of F_c, F_f, F_p, [N/mm^2]
$k_{c1,0.1}$, $k_{f1,0.1}$, $k_{p1,0.1}$	main values of the specific cutting force in the directions of F_c, F_f, F_p, in case of fine turning, [N/mm^2]
$k_{c1.1}$	main value of the specific cutting force (Kienzle-Victor model), [N/mm^2]
KO36	austenite stainless steel
κ_r	side cutting angle, [°]
l_{eff}	effective cutting length of the edge of the tool, [mm]
PCD	polycrystalline diamond
r_ε	nose radius of the tool, [mm]
v_c	cutting speed, [m/min]

5 ACKNOWLEDGEMENTS

Supported by the ÚNKP-16-4/I. New National Excellence Program of the Ministry of Human Capacities, Hungary.

6 REFERENCES

[1] Rusinek, R., Wiercigroch, M., & Wahi, P. (2015). Orthogonal cutting process modelling considering tool-workpiece frictional effect. *Procedia CIRP*, vol. 31, p. 429-434, **DOI:10.1016/j.procir.2015.03.033**.

[2] Kulkarni, A.P., Joshi, G.G., Karekar, A., Sargade, V.G. (2014). Investigation on cutting temperature and cutting force in turning AISI 304 austenitic stainless steel using AlTiCrN coated carbide insert. *International Journal of Machining and Machinability of Materials*, vol. 15, no. 3-4, p. 147-156, **DOI:10.1504/IJMMM.2014.060546**.

[3] Čep, R., Janásek, A., Sadílek, M., & Čepová, L. (2012). Tungaloy Ceramic Cutting Tools at Interrupted Machninig. *Engineering Review*, vol. 32, no. 2, p. 112-118.

[4] Suresh, R., Basavarajappa, S., Samuel, G.L. (2012). Some studies on hard turning of AISI 4340 steel using multilayer coated carbide tool. *Measurement*, vol. 45. no. 7, p. 1872-1884, **DOI:10.1016/j.measurement.2012.03.024**.

[5] López de Lacalle, L.N., Lamikiz, A., Sánchez, J. A., Salgado, M.A. (2004). Effects of tool deflection in the high-speed milling of inclined surfaces. *The International Journal of Advanced Manufacturing Technology*, vol. 24, no. 9, p. 621-631, **DOI: 10.1007/s00170-003-1723-x**.

[6] Cukor, G., Jurković, Z. (2010). Optimization of turning using evolutionary algorithms. *Engineering Review*, vol. 30, no. 2, p. 1-10.

[7] Singaravel, B., Selvaraj, T. (2015). Optimization of machining parameters in turning operation using combined TOPSIS and AHP method. *Tehnički Vjesnik - Technical Gazette*, vol. 22, no. 6, p. 1475-1481, **DOI:10.17559/TV-20140530140610**.

[8] Selvaraj, D.P., Chandramohan, P., Mohanraj, M. (2014). Optimization of surface roughness, cutting force and tool wear of nitrogen alloyed duplex stainless steel in a dry turning process using Taguchi method. *Measurement*, vol. 49, p. 205-215, **DOI:10.1016/j.measurement.2013.11.037**.

[9] Puh, F., Jurkovic, Z., Perinic, M., Brezocnik, M., & Buljan, S. (2016). Optimization of machining parameters for turning operation with multiple quality characteristics using Grey relational analysis. *Tehnički vjesnik – Technical Gazette*, vol. 23, no. 2, p. 377-382, **DOI:10.17559/TV-20150526131717**.

[10] Hassine, H., Barkallah, M., Bellacicco, A., Louati, J., Riviere, A., Haddar, M. (2015). Multi objective optimization for sustainable manufacturing, application in turning. *International Journal of Simulation Modelling*, vol. 14, no. 1, p. 98-109, **DOI:10.2507/IJSIMM14(1)9.292**.

[11] Karpuschewski, B., Schmidt, K., Beňo, J., Maňková, I., Frohmüller, R., Prilukova, J. (2015). An approach to the microscopic study of wear mechanisms during hard turning with coated ceramics. *Wear*, vol. 342-343, p. 222-233, **DOI:10.1016/j.wear.2015.08.021**.

[12] Nayak, M., Sehgal, R. (2015). Effect of tool material properties and cutting conditions on machinability of AISI D6 steel during hard turning. *Arabian Journal for Science and Engineering*, vol. 40, no. 4, p. 1151-1164, **DOI:10.1007/s13369-015-1578-0**.

[13] El Hakim, M.A., Shalaby, M.A., Veldhuis, S.C., Dosbaeva, G.K. (2015). Effect of secondary hardening on cutting forces, cutting temperature, and tool wear in hard turning of high alloy tool steels. *Measurement*, vol. 65, p. 233-238, **DOI:10.1016/j.measurement.2014.12.033**.

[14] Kundrák, J., Mamalis, A.G., Gyani, K., Bana, V. (2011). Surface layer microhardness changes with high-speed turning of hardened steels. *The International Journal of Advanced Manufacturing Technology*, vol. 53, no. 1, p. 105-112, **DOI:10.1007/s00170-010-2840-y**.

[15] Chen, T., Li, S., Han, B., Liu, G. (2014). Study on cutting force and surface micro-topography of hard turning of GCr15 steel. *The International Journal of Advanced Manufacturing Technology*, vol. 72, no. 9, p. 1639-1645, **DOI:10.1007/s00170-014-5778-7**.

[16] Meddour, I., Yallese, M. A., Khattabi, R., Elbah, M., Boulanouar, L. (2015). Investigation and modeling of cutting forces and surface roughness when hard turning of AISI 52100 steel with mixed ceramic tool: cutting conditions optimization. *The International Journal of Advanced Manufacturing Technology*, vol. 77, no. 5, p. 1387-1399, **DOI:10.1007/s00170-014-6559-z**.

[17] Wojciechowski, S., Chwalczuk, T., Twardowski, P., Krolczyk, G.M. (2015). Modeling of cutter displacements during ball end milling of inclined surfaces. *Archives of Civil and Mechanical Engineering*, vol. 15, no, 4, p. 798-805, **DOI:10.1016/j.acme.2015.06.008**.

[18] Wojciechowski, S., Maruda, R.W., Nieslony, P., Krolczyk, G.M. (2016). Investigation on the edge forces in ball end milling of inclined surfaces. *International Journal of Mechanical Sciences*, vol. 119, p. 360-369, **DOI:10.1016/j.ijmecsci.2016.10.034**.

[19] Wojciechowski, S., Twardowski, P., Pelic, M., Maruda, R.W., Barrans, S., Krolczyk, G.M. (2016). Precision surface characterization for finish cylindrical milling with dynamic tool displacements model. *Precision Engineering*, vol. 46, p. 158-165, **DOI:10.1016/j.precisioneng.2016.04.010**.

[20] Zębala, W., Kowalczyk, R. (2015). Estimating the effect of cutting data on surface roughness and cutting force during WC-Co turning with PCD tool using Taguchi design and ANOVA analysis. *The International Journal of Advanced Manufacturing Technology*, vol. 77, no. 9, p. 2241-2256, **DOI:10.1007/s00170-014-6382-6**.

[21] Mata, F., Hanafi, I., Beamud, E., Khamlichi, A., Jabbouri, A. (2012). Modelling of machining force components during turning of PEEK CF30 by TiN coated cutting tools using artificial intelligence. *International Journal of Machining and Machinability of Materials*, vol. 11, no. 3, p. 263-279, **DOI:10.1504/IJMMM.2012.046885**.

[22] Hanafi, I., Khamlichi, A., Cabrera, F.M., López, P.J.N., Jabbouri, A. (2012). Fuzzy rule based predictive model for cutting force in turning of reinforced PEEK composite. *Measurement*, vol. 45, no. 6, p. 1424-1435, **DOI:10.1016/j.measurement.2012.03.022**.

[23] Fetecau, C., Stan, F. (2012). Study of cutting force and surface roughness in the turning of polytetrafluoroethylene composites with a polycrystalline diamond tool. *Measurement*, vol. 45, no. 6, p. 1367-1379, **DOI:10.1016/j.measurement.2012.03.030**.

[24] Joardar, H., Das, N.S., Sutradhar, G., Singh, S. (2014). Application of response surface methodology for determining cutting force model in turning of LM6/SiCP metal matrix composite. *Measurement*, vol. 47, p. 452-464, **DOI:10.1016/j.measurement.2013.09.023**.

[25] Çolak, O. (2014). Optimization of machining performance in high-pressure assisted turning of Ti6Al4V alloy. *Strojniški vestnik - Journal of Mechanical Engineering*, vol. 60, no. 10, p. 675-681, **DOI:10.5545/sv-jme.2013.1079**.

[26] de Agustina, B., Bernal, C., Camacho, A.M., Rubio, E.M. (2013). Experimental analysis of the cutting forces obtained in dry turning processes of UNS A97075 aluminium alloys. *Procedia Engineering*, vol. 63, p. 694-699, **DOI:10.1016/j.proeng.2013.08.248**.

[27] Horváth, R., Drégelyi-Kiss, Á., Mátyási, Gy. (2014). Application of RSM method for the examination of diamond tools. *Acta Polytechnica Hungarica*, vol. 11, no. 2, p. 137-147, **DOI:10.12700/APH.11.02.2014.02.8**.

[28] Horváth, R., Drégelyi-Kiss, Á. (2015). Analysis of surface roughness of aluminum alloys fine turned: United phenomenological models and multi-performance optimization. *Measurement*, vol. 65, p. 181-192, **DOI:10.1016/j.measurement.2015.01.013**.

[29] Horváth, R., Czifra, Á., Drégelyi-Kiss, Á. (2015). Effect of conventional and non-conventional tool geometries to

skewness and kurtosis of surface roughness in case of fine turning of aluminium alloys with diamond tools. *The International Journal of Advanced Manufacturing Technology*, vol. 78, no.1, p. 297-304, **DOI:10.1007/s00170-014-6642-5**.

[30] Horváth, R., Pálinkás, T., Mátyási, G., Drégelyi-Kiss, Á.G. (2017). The design, calibration and adaption of a dynamometer for fine turning. *International Journal of Machining and Machinability of Materials*, vol. 19, no. 1, p. 1-16, **DOI:10.1504/IJMMM.2017.081183**.

[31] Horváth, R. (2015). A New Model for Fine Turning Forces. *Acta Polytechnica Hungarica*, vol. 12, no. 7, p. 109-128, **DOI:10.12700/APH.12.7.2015.7.7**.

[32] Venkatesan, K., Radhakrishnan, R., Kuppan, P. (2014). A review on conventional and laser assisted machining of aluminium based metal matrix composites. *Engineering Review*, vol. 34, no. 2, p. 75-84.

[33] Kundrák, J., Gyáni, K., Deszpoth, I., Sztankovics, I. (2014). Some topics in process planning of rotational turning. *Engineering Review*, vol. 34, no. 1, p. 23-32.

[34] Kienzle, O., Victor, H. (1957). Spezifische schnittkräfte bei der metallbearbeitung, *Werkstattstechnik und Maschinenbau*, vol. 47, no. 5, p. 224-225.

[35] Bus, C., Touwen, N.A.L., Veenstra, P.C., Van Der Wolf, A.C.H. (1971). On the significance of equivalent chip thickness. *Annals of the CIRP*, vol. 19, p. 121-124.

[36] Biró, I., Czampa, M., Szalay, T. (2015). Experimental model for the main cutting force in face milling of a high strength structural steel. *Periodica Polytechnica Engineering*, vol. 59, no. 1, p. 8-15, **DOI:10.3311/PPme.7516**.

[37] Biró, I., Szalay, T. (2016). Extension of empirical specific cutting force model for the process of fine chip-removing milling. *The International Journal of Advanced Manufacturing Technology*, vol. 88, no. 9, p. 2735–2743, **DOI:10.1007/s00170-016-8957-x**.

[38] Aouici, H., Yallese, M.A., Chaoui, K., Mabrouki, T., Rigal, J. (2012). Analysis of surface roughness and cutting force components in hard turning with CBN tool: Prediction model and cutting conditions optimization. *Measurement*, vol. 45, no. 3, p. 344-353, **DOI:10.1016/j.measurement.2011.11.011**.

[39] Gokkaya, H., Taskesen, A. (2008). The effects of cutting speed and feed rate on Bue-Bul formation, cutting forces and surface roughness when machining AA6351 (T6) Alloy. *Strojniški vestnik – Journal of Mechanical Engineering*, vol. 54, no. 7-8, p. 521-530.

[40] Velchev, S., Kolev, I., Ivanov, K. (2009). Research on the influence of the cutting speed on the specific cutting force during turning. *Strojniški vestnik - Journal of Mechanical Engineering*, vol. 55, no. 6, p. 400-405.

Strojniški vestnik - Journal of Mechanical Engineering 63(2017)9, 501-509

DOI:10.5545/sv-jme.2016.4272 Original Scientific Paper
Received for review: 2016-12-15
Received revised form: 2017-06-02
Accepted for publication: 2017-07-10

The Effect of the Thickness-to-Die Diameter Ratio on the Sheet Metal Blanking Process

Kaan Emre Engin[1,*] – Omer Eyercioglu[2]
[1]Adiyaman University, Faculty of Technology, Automotive Engineering Department, Turkey
[2]Gaziantep University, Engineering Faculty, Mechanical Engineering Department, Turkey

The blanking process has a wide range of usage in the sheet metal production industry. The effectiveness of the process rests on the balance between the surface quality of the blanks and energy conservation during the process. The effects of different process parameters on surface quality and energy efficiency have been studied by researchers, but there is a gap concerning the effect of the thickness-to-die diameter ratio on surface quality and energy efficiency. In this study, four different thickness-to-die diameter ratios (t/D_m=1/5, t/D_m=1/10, t/D_m=1/30 and t/D_m=1/50) with five different clearances (1 %, 3 %, 5 %, 10 %, and 20 % of thickness) were used to blank 2-mm-thick round workpieces made of AISI 304 stainless steel. Both experimental and FEM studies were accomplished. A special die set was manufactured and a hydraulic press was used for experimental studies. For FEM studies, Deform-2D was used. Investigations were made on the effects of different thickness-to-die diameter ratios on the blanking force, cutting energy crack propagation angles, and zone distribution related to surface quality. Results gathered from FEM simulations and experimental studies were coherent with each other.

Keywords: blanking process, blanking parameters, shear zone, clearance

Highlights

- *A common stainless steel (AISI 304) with 2 mm thickness were blanked by four different thickness-to-die diameter ratios (t/D_m = 1/5, t/D_m = 1/10, t/D_m = 1/30 and t/D_m = 1/50) and under five different clearances (1 %, 3 %, 5 %, 10 %, and 20 % of thickness) for each ratio.*
- *Both experimental and FEM investigations were accomplished. A special die set with changeable die and punches were manufactured and a hydraulic press with different loading capabilities was used for experimental investigations. Deform-2D was used for FEM investigations.*
- *The ideal cutting condition is the point at which the cutting energy is lowest and surface quality is at best.*
- *It was determined that the ideal cutting condition can be achieved at 3 % clearance for t/D_m = 1/5 and t/D_m = 1/10 and at 5 % clearance for t/D_m = 1/30 and t/D_m = 1/5.*
- *The change in t/D_m ratio changes punch load, stroke depth and cutting energy. The ratio difference also has a small effect on the clearance value.*

0 INTRODUCTION

The blanking process has an important usage in sheet metal forming applications. The process of blanking can be described as the shearing of the workpiece (sheet metal) into the desired shape (blank), which is pressed on to the lower die by a blankholder and then perforated by the upper die (punch). The sheet metal part undergoes large elastoplastic deformations that lead to the development of damage and eventually complete fracture of the material [1].

Although the general aspects of blanking seem simple, many parameters govern the process, and all of them have their own effects on the quality of the blanks. The general process parameters include the clearance, material type and thickness, cutting velocity, tool geometry, tool wear, and kinematic of the press [2].

For many years, researchers have been attempting to determine the effects of some of these parameters and related outcomes in the blanking process using experimental and numerical (finite element) methods. Some recent examples are as follows. Lubis and Mahardinka [3] studied the effect of clearance and cutting velocity on the sheared surface of copper sheets experimentally and observed the positive effects of high cutting velocities. Swillo and Czyzewski [4] examined the effect of different clearances on the material fracture by experimental and numerical methods. Wu et al. [5] used three different clearances for blanking high strength steels and proposed a new calculation method to characterize strain distribution in the sheared region. Mucha [6] attempted to observe the effect of clearance, tool coatings, and tool materials on the wear of blanking tools. Col et al. [7] investigated the tool wear of AlCrN coated punches during blanking with experimental methods. Wang et al. [8] also tried to observe the different wear characteristics of different die materials in high strength steel blanking. Bolka et al. [9] studied the identification of the material characteristics and damage correlation through in and out-of- plane direction for blanking

*Corr. Author's Address: Adiyaman University, Altinsehir Mah., No:13, Adiyaman, Turkey, kengin@adiyaman.edu.tr

with experimental methods. Subramonian et al. attempted to determine the interaction between the punch, stripper plate and sheet material under various speeds in blanking; furthermore, the effect of punch velocity on the blanking load was investigated in this study [10] and in another [11]. Kanca et al., showed the effect of blanking speed on the surface quality of mild [12] and stainless-steel blanks [13]. Al-Momani et al. [14] developed and compared two models based on an artificial neural network and a multiple regression analysis to predict the burr height as a representation of surface quality. Hu et al. [15] used a FEM method to investigate the heat generation at the shear zone due to different blanking speeds. Magesh et al. [16] examined the effect of different clearances on the shearing and wrinkling behaviour of AISI 316 stainless steel by using a FEM method. Hambli et al. proposed using a FEM method and neural network analysis to optimize the clearance between punch and die [17] and [18]. Mole et al. [19] proposed a new FEM method to optimize the blank shape. Behrens et al. [20] focused on the effect of speed and clearance to the blank load and sheared surface geometry distribution. Soares et al. [21] examined the effect of clearance on the sheared edge quality of thick sheets (8 mm) by FE- simulations.

It can be understood that research studies involving blanking parameters are many and cover various aspects of the procedure by experimental and FEM methods. However, it was realized that the size of a blank should also have an effect because the desired blanked product for different industrial applications can vary greatly in size. One of the most important advantages of blanking is that different sizes can be produced efficiently by proper tooling. The researchers who tried to investigate different aspects of blanking did not consider the size parameter and its outcomes, which led to a gap in the blanking literature.

In this paper, four different thickness-to-die diameter ratios ($t/D_m = 1/5$, $t/D_m = 1/10$, $t/D_m = 1/30$ and $t/D_m = 1/50$) with five different clearances (1 %, 3 %, 5 %, 10 %, and 20 % of thickness) were used to blank round workpieces made of AISI 304 stainless steel. Both experimental and numerical methods were used to determine the effect of ratio differences and clearances on the blanking force, cutting energy, and crack propagation angles related to surface quality.

1 PROCESS PARAMETERS

1.1 Finite Element Model

Experimental methods to observe blanking often rely on trial-and-error procedures that require excessive time and money. One of the most economical and less time-consuming approaches to observe blanking is modelling the process by using the finite element method (FEM). The user can simulate the process by defining all variables, including material properties, speed of the punch, contact conditions at all the interfaces, etc.

For this study, the Deform-2D package, which is a product of the Scientific Forming Technologies Corporation (STFC) was used to make the FEM models. This FEM code is based on an implicit Lagrangian computational routine [18]. The blanking process was considered axisymmetric, and a 2D model was used to simulate the process parameters. Thus, modelling only one half of the tooling is enough for executing the runs.

The blanking setup considered for simulations is given in Fig. 1. The setup has four components: The punch, lower die, sheet material, and a blank holder to hold the sheet stock for unwanted bending during the blanking process. The sheet material was considered to be a plastic object whereas the punch, die and blank holder were considered rigid bodies. Friction between the workpiece and tools was assumed to follow constant shear friction.

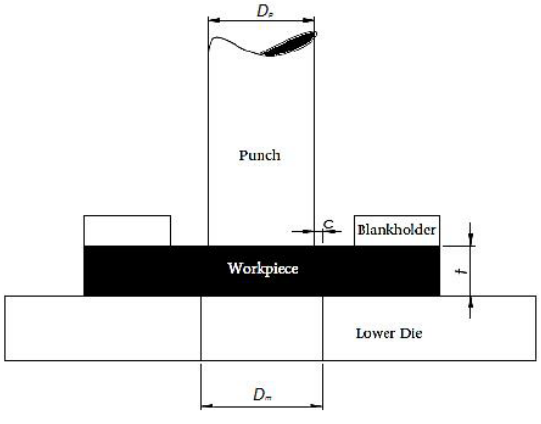

Fig. 1. *The blanking setup for simulations*

The frictional force in this type of definition is expressed in Eq. 1 as;

$$f_s = mk, \tag{1}$$

where f_s is the frictional stress, k is the shear yield stress, and m is the friction factor. This states that the friction is a function of the yield stress of the deforming body.

In the blanking process, large plastic strain generation happens in the narrow shear zone. It was assumed that the material was isotropic and that yielding occurred according to the Von Mises yield criterion. The flow stress is expressed in Eq. (2) as:

$$\bar{\sigma} = K\bar{\varepsilon}^{n}, \tag{2}$$

where $\bar{\sigma}$ is the effective stress, $\bar{\varepsilon}$ is the effective strain, K is the material constant, and n is the strain-hardening exponent [22].

Normalized Cockroft and Latham was chosen as the fracture criterion. This criterion predicts the fracture strain more precisely than the other criterions in metal forming processes [22]. The criterion states that the fracture occurs when the effective strain reaches the critical value, expressed in Eq. (3) as:

$$\int_{0}^{\varepsilon^{-f}} \left(\frac{\sigma^{*}}{\bar{\sigma}} \right) d\bar{\varepsilon} = C, \tag{3}$$

where σ^* is the maximum principal tensile stress, ε^{-f} the fracture strain and C is the critical value. The effective stress and effective strain are defined as $\bar{\sigma}$ and $\bar{\varepsilon}$. The critical value C can be evaluated with a tensile test and does not depend on the working operation. C for AISI 304 was found experimentally by executing a tensile test.

During the blanking process, shearing of the workpiece happens in a narrow zone called the shear band. The behaviour of the shear band in shear hat test was studied by Pepelnjak et al., and they showed that the variation of medial diameter and shearing surface change is less than 1 % [23]. The stress ratio $\left(\sigma^{*}/\bar{\sigma}\right)$ is assumed to be constant throughout that band where the deformation is highly concentrated. Therefore, this assumption may be implemented into the Cockroft and Latham criterion and approximated by $\varepsilon^{-f} = C^{*}$ at the shear band. This approach postulates that a crack initiation occurs at the point of the sheet whose effective strain first reaches the fracture strain of the work material [17]. During the simulations, element deletion occurs when the critical values are satisfied. In the DEFORM program, the simulation stops time to time to execute element deletion; this feature has two governing parameters which are "fracture steps" and "fracture elements". Fracture steps value determines the step interval at which the simulation stops and performs element deletion. This value was chosen as '1', which is the minimum value. This means that element deformation is taken into account in each step. Fracture elements are the number of the elements that must be above the critical damage value for the simulation to stop and perform element deletion. This value was chosen as '4' as the system default.

As mentioned, the deformation and crack propagation happen in a narrow zone within the punch die clearance. If critical values are satisfied, the simulation stops and performs element deletion in this zone, according to the fracture steps and fracture elements values. However, element deletion from the components in simulation causes volume loss and may lead to incorrect calculations. To prevent and limit volume degradation, a very fine mesh must be used, and mesh elements should be concentrated where a probable fracture occurrence is expected. First, 10,000 isoparametric quadratic elements with 0.03 mm element size were used as the element meshes of the sheet; these are the highest element number values that can be defined in Deform. Then, by using equally spaced mesh density windows created specifically for different ratios, mesh elements were equally concentrated (to the greatest degree possible) around the deformation zone. These mesh windows move with the punch and constantly try to discretize the sheet surface within specific mesh densities when remeshing. The geometrical model of the blanking process and the FEM meshes of the workpiece were given in Fig. 2.

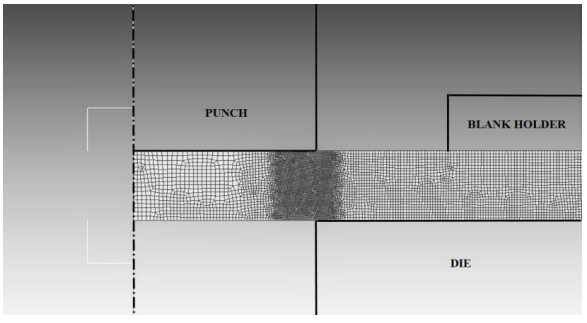

Fig. 2. *The geometrical model of the blanking process and the FEM meshes of the workpiece*

1.2 Ideal Cutting Condition and Crack Propagation Angles

The ideal cutting condition occurs when the punch load is the lowest for energy conservation, and the quality of the blanked part is so good that no extra labour is needed to correct the defects on the blanked part surfaces. This means that the shear zone (indentation) depth is at least one third of the sheet thickness, and no

burr is forming. The ideal cutting condition is achieved when the angle of real crack propagation direction β coincides with the angle of ideal crack propagation direction θ. The real crack propagation direction is the actual direction of crack propagation, which is formed on the blank surface, whereas the ideal crack propagation direction is the desired path of the crack propagation towards the cutting edges of the punch and lower die. It can be mentioned that values of β closer to values of θ result in smoother surfaces.

If the crack propagations do not coincide, secondary crack formation occurs that creates rough surfaces. The directions of angle β and angle θ are illustrated in Fig. 3. As it is evident from Fig. 3, the real crack propagation direction does not coincide with the ideal crack propagation direction, creating secondary cracks. The equalization of ideal crack propagation angle θ and the angle of the direction of real crack propagation β giving the ideal cutting condition can be expressed in Eq. (4) as:

$$\Phi = \beta - \theta \cong 0. \tag{4}$$

The ideal crack propagation angle can be expressed in Eq. (5) as:

$$\theta = Arc\tan(\frac{c}{t-u_p}), \tag{5}$$

where c is the clearance; t is the sheet metal (workpiece) thickness and u_p is the punch penetration corresponding to the first crack initiation within the sheet.

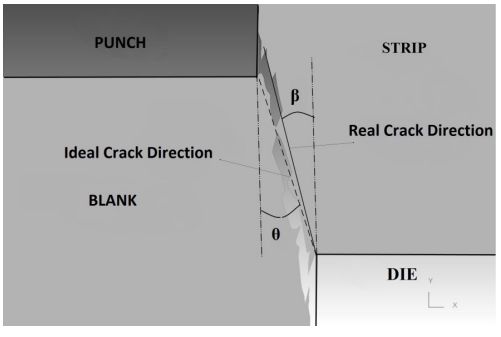

Fig. 3. *Illustration of real crack propagation angle β, ideal crack propagation angle θ, and secondary cracks*

2 EXPERIMENTAL

2.1 Material Model and Experimental Setup

AISI 304 stainless steel was used for both simulation and experimental studies. AISI 304 is a very common type of stainless steel used in various industrial applications varying in different forms from simple hypodermic needles to marine and nuclear applications [24]. The engineering and flow curve of AISI 304 were obtained from tensile tests. A Shimadzu AG-X Plus tensile testing machine was used with a constant loading velocity of 0.01 s^{-1}. The test was repeated 10 times at room temperature, and the engineering stress-strain curve was obtained. The flow curve of AISI 304 was calculated by using the well-known true stress-strain equations expressed in Eqs. (6) and (7) as:

$$\sigma_t = \sigma(1+\varepsilon), \tag{6}$$

$$\varepsilon_t = \ln(1+\varepsilon), \tag{7}$$

where σ_t and σ are true and engineering stresses, whereas ε_t and ε are true and engineering strains, respectively.

The obtained flow curve was identified in the Deform program's database so that simulation results could meet the experimental results. The true (flow curve) and engineering stress-strain curves of AISI 304 were given in Fig. 4.

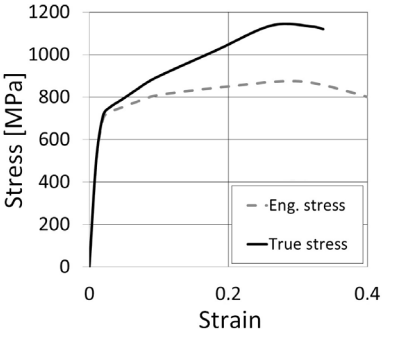

Fig. 4. *Engineering and true stress-strain curves of AISI 304*

The isometric and exploded view of the designed die and its components were given in Fig. 5. The die consists of six components; upper die block (1), punch (2), punch holder (3), fixed stripper (4), lower die (5) and lower die block (6).

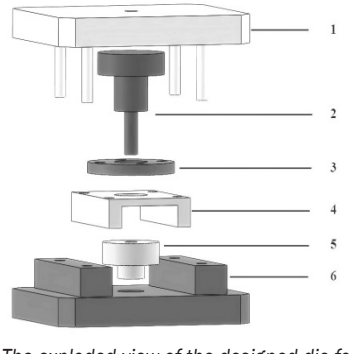

Fig. 5. *The exploded view of the designed die for experiments*

The upper die block, punch holder, fixed stripper and lower die block were made of St 37 steel whereas the guide rods on the upper die block, punch and lower die were made of heat treated AISI 4140 for long durability.

The predetermined size of the blank should play a major role in the process. The same clearance values for blanks with different diameters are unlikely although their thicknesses are the same.

So, four different thicknesses to die diameter ratios ($t/D_m = 1/5$, $t/D_m = 1/10$, $t/D_m = 1/30$ and $t/D_m = 1/50$) were used to evaluate the effects of sizes. The thickness of the workpiece was taken 2 mm. The lower die diameters were calculated according to the ratios as 10 mm, 20 mm, 60 mm and 100 mm. Five different clearance values (1 %, 3 %, 5 %, 10 %, and 20 % of thickness) were used, and punch diameters were calculated according to the clearance formula expressed in Eq. (8) as:

$$C = 100\frac{D_m - D_p}{2t}[\%], \tag{8}$$

where D_m is the lower die diameter, D_p is the punch diameter, and t is the workpiece thickness.

Calculated punch diameters were given in Table 1. Manufactured punches and die for $t/D_m = 1/5$ were given in Fig. 6 as an example. The diameters of punches according to clearances from left to right were 1 % (9.96 mm), 3 % (9.88 mm), 5 % (9.80 mm), 10 % (9.60 mm), and 20 % (9.20 mm). The clearance between the punch and die must be precise, so punches are manufactured within a ±0.01 mm tolerance limit.

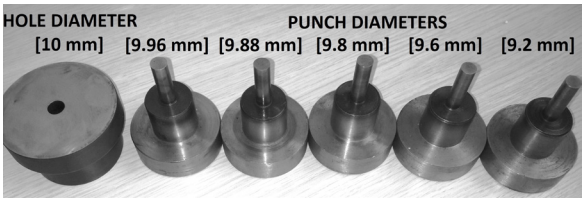

Fig. 6. One set of manufactured punches (t/D_m=1/5)

Table 1. *Punch diameters used in simulation and experimental studies*

C	Punch diameters [mm]			
	Ratio 1/5	Ratio 1/10	Ratio 1/30	Ratio 1/50
1 %	9.96	19.96	59.96	99.96
3 %	9.88	19.88	59.88	99.88
5 %	9.80	19.80	59.80	99.80
10 %	9.60	19.60	59.60	99.60
20 %	9.20	19.20	59.20	99.20

All experiments were done by using a 300 kN capacity hydraulic press. Speed had been kept constant, and a 0.01 m/s punch speed was used to execute the blanking processes.

3 RESULTS AND DISCUSSION

The microscopic image of a blank and the image taken from FE simulation were given in Fig. 7. As can be seen, crack propagations and related zones are similar between experimental and simulation results. The numerical values gathered from experiments and simulations (punch load, stroke, blanking energy, etc.) are also similar. The punch load difference between simulation and real experimental values for $t/D_m = 1/10$ at 5 % clearance were given in Fig. 8.

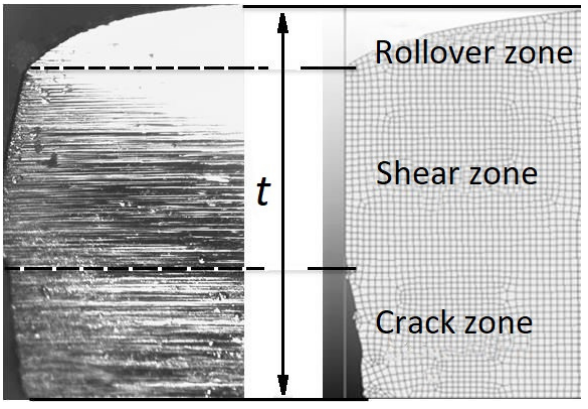

Fig. 7. *The microscopic image and the simulation image of a blank ($t/D_m = 1/10$, $t = 2$ mm, clearance: 5 %)*

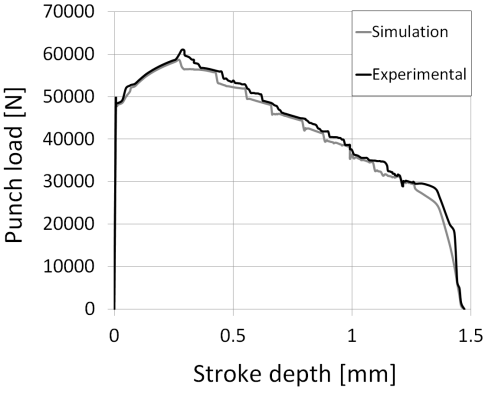

Fig. 8. *Punch load difference between experimental and simulation results. (t/Dm=1/10, clearance: 5 %)*

3.1 Punch Load, Cutting Energy and Surface Quality

Punch load plays an important role in blanking process. Although the gathered punch load value is

the result of the process, and it cannot be adjusted for specific conditions, minimum required punch load for a blanking process is simply calculated in Eq. (9) as [25];

$$F = L \times t \times \tau, \tag{9}$$

where F is the blanking force [N], L is the forming circumference [mm], t is the strip thickness [mm] and τ is the shear strength [MPa].

The punch load differences between four different t/D_m ratios at 5 % clearance were given in Fig. 9. As can be seen from Fig. 9, the punch load increases with increasing blank size as expected, and stroke depth increases with increasing t/D_m ratios.

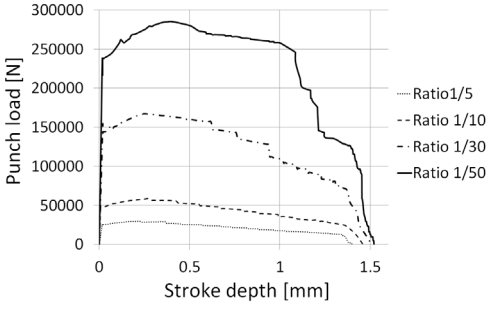

Fig. 9. *Punch load difference between different t/D_m ratios at 5% clearance*

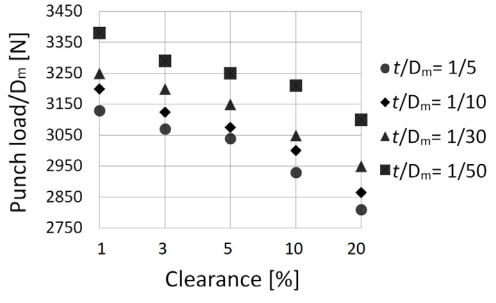

Fig. 10. *Relative punch load versus clearance for different t/D_m ratios*

The differences in punch loads for four t/D_m ratios under different clearances were given in Fig. 10. Relative punch load (F/D_m) were used to make comparisons.

Fig. 10 shows that the punch load at every clearance increases with increasing t/D_m ratios. Additionally, as the clearance increases for each ratio, the punch loads required to cut the blanks decrease. It may be assumed that the usage of higher clearances might be more beneficial for energy saving but taking only the punch load into consideration may lead to incorrect interpretations. Instead, taking cutting energy into consideration which is the ratio between punch load and stroke depth gives more realistic insight into the situation. Especially with changing clearance, punch load and stroke depth also change, which causes alteration in the cutting energies.

In contrast, surface quality should be taken into consideration along with cutting energy parameters. A burr-free part with good crack propagation can save on extra deburring operations, labour and extra money as well as energy efficiency. Clearance values also determine the crack propagation and zone distribution in the shear zone. It can be stated that the ideal cutting condition is where the spent energy is low and the blank's surface quality is good.

Cutting energy differences between t/D_m ratios under different clearances were given in Fig. 11.

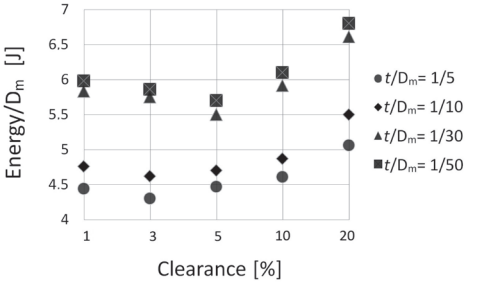

Fig. 11. *Relative cutting energy difference between t/D_m ratios under different clearances*

Fig. 11 shows that the lowest cutting energies were achieved at 3 % clearance for $t/D_m = 1/5$ and $t/D_m = 1/10$ ratios and at 5 % clearance for $t/D_m = 1/30$ and $t/D_m = 1/50$ ratios.

Fig. 12 shows experimental and simulation images of the crack propagation on a blank ($t/D_m = 1/5$ at 5 % clearance) as an example.

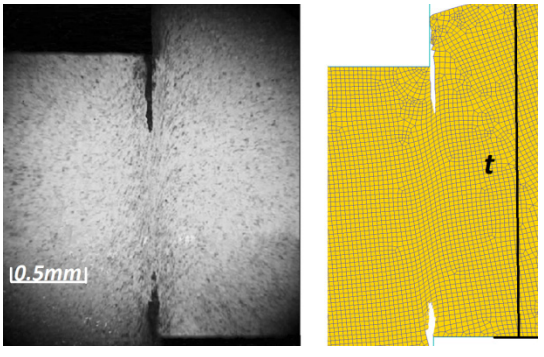

Fig. 12. *Experimental and simulation images of crack propagation ($t/D_m = 1/5$, $t = 2$ mm, clearance: 5 %)*

The difference between real crack propagation angle β and ideal crack propagation angle θ was

calculated according to $\Phi=\beta-\theta$ condition. The condition postulates that the closer Φ is to zero, the smoother the blanked surface is. The closest values to zero were found when the clearance was 3 % for $t/D_m=1/5$ and $t/D_m=1/10$ and 5 % clearance for $t/D_m=1/30$ and $t/D_m=1/50$ ratios. Furthermore, as the clearance increased, the difference between real crack propagation angle β and ideal crack propagation angle θ increased which resulted in low surface quality. The differences between angles are shown in Fig. 13.

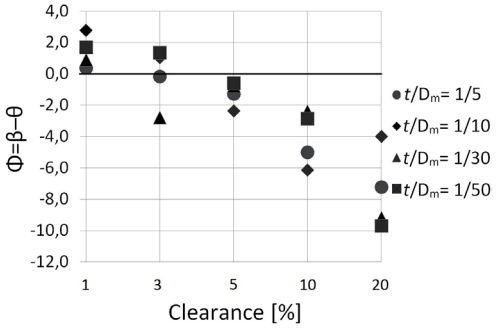

Fig. 13. *The difference between real crack propagation angle (β) and ideal crack propagation angle (θ)*

Zone distribution on the shear surface of a blank is closely related with clearance value. The amount of shear zone is also the expression of good surface quality whereas an increase in the crack zone means the opposite. The blanks for each t/D_m ratio were given in Fig. 14.

Fig. 15 shows the microscopic image of the shear surface of the blank ($t/D_m=1/10$, clearance: 5 %). The shear zone is the burnished part at the lower portion of the surface and crack zone is the rougher part on the upper portion.

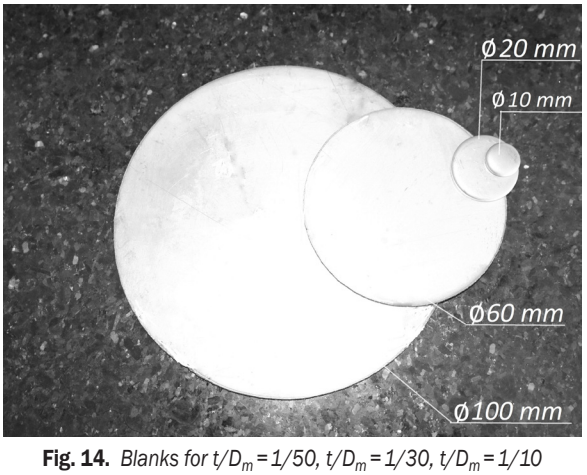

Fig. 14. *Blanks for $t/D_m=1/50$, $t/D_m=1/30$, $t/D_m=1/10$ and $t/D_m=1/5$*

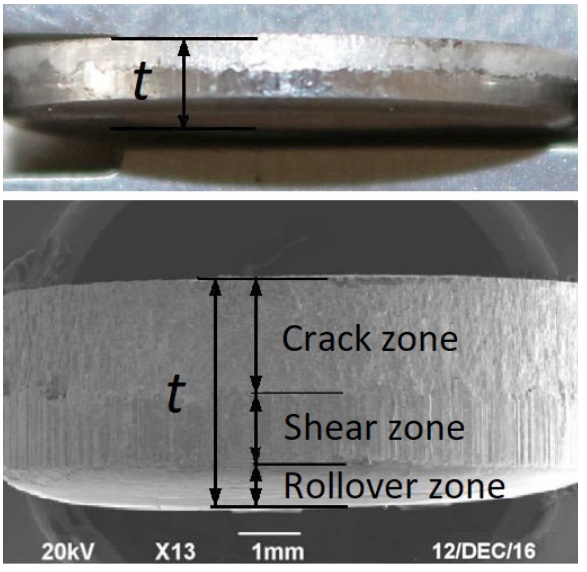

Fig. 15. *Shear, crack and rollover zone distribution on a blank ($t/D_m=1/10$, $t=2$ mm, clearance: 5 %)*

Fig. 16 shows the shear zone length percentage for all t/D_m ratios.

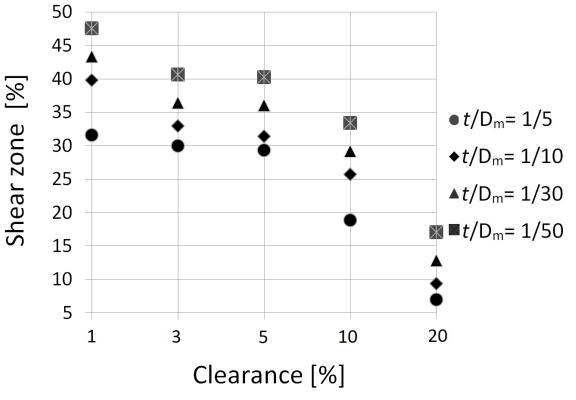

Fig. 16. *Shear zone percentage for t/D_m ratios*

Fig. 16 shows that clearance affects the shear zone depth. The overly tight clearance increased the shear zone depth, but it also increased the blanking load according to Fig. 10. This situation can cause more energy to be consumed and probable early tool wear.

When the clearance became too loose, shear zone depth decreased. From Fig. 16, it can be understood that the crack zone started to dominate sheared surfaces after exceeding 10 % clearance for all t/D_m ratios. It is also evident from Fig. 13 that the real crack propagation direction diverges from the ideal direction at higher clearances, which can cause protruded surfaces.

For higher ratios, the difference of shear zone percentage between 3 % and 5 % clearance is slight. Therefore, it is important to adjust the clearance value where the shear zone is long and blanking energy is low. The combined interpretation of the results leads to the point that 3 % clearance is suitable for $t/D_m = 1/5$ and $t/D_m = 1/10$ ratios and 5 % clearance is suitable for $t/D_m = 1/30$ and $t/D_m = 1/50$ ratios when blanking AISI 304 stainless steel.

4 CONCLUSIONS

In this study, four different thickness-to-die diameter ratios ($t/D_m = 1/5$, $t/D_m = 1/10$, $t/D_m = 1/30$ and $t/D_m = 1/50$) with five different clearances (1 %, 3 %, 5 %, 10 %, and 20 % of the thickness) were used to blank round workpieces made of AISI 304 stainless steel. The punch load, cutting energy, crack propagation angles, and zone distributions on the blanks were observed. The following conclusions can be made;

- Blanking energy, crack propagation angles and zone distribution are related. Tool adjustment, especially the clearance adjustment should be made to achieve both aspects. There is an optimal clearance value that aligns all these parameters at the same time.
- The results have shown the ideal clearance value not only depends on material thickness, but also the thickness-to-die diameter ratio of the blank. The ideal clearance for AISI 304 at which energy saving and good surface quality can be achieved is 3 % for $t/D_m = 1/5$ and $t/D_m = 1/10$ (blanks with small circumferences) and 5 % for $t/D_m = 1/30$ and $t/D_m = 1/50$ (blanks with big circumferences).
- The increase in t/D_m ratio also increases punch load, stroke depth and as a result cutting energy. When the circumference of the material with the same thickness increases, the clearance value also shows a small tendency to increase.

5 REFERENCES

[1] Lemiale, V., Chambert, J., Picart, P. (2009). Description of numerical techniques with the aim of predicting the sheet metal blanking process by FEM simulation. *Journal of Materials Processing Technology*, vol. 209, no. 5, p. 2723-2734, **DOI:10.1016/j.jmatprotec.2008.06.019**.

[2] Sidhu, K.B., Peshekhodov, I., Behrens, B.-A. (2008). Numerical modelling of high speed blanking considering thermoviscoplastic effects. *3rd International Conference on High Speed Forming*, p. 97-106.

[3] Lubis, Z.D., Mahardika, M. (2016). Influence of clearance and punch velocity on the quality of pure thin copper sheets blanked parts. *IOP Conference Series: Materials Science and Engineering*, vol. 157, no. 1, p. 1-6, **DOI:10.1088/1757-899X/157/1/012012**.

[4] Swillo, S., Czyzewski, P. (2013). An experimental and numerical study of material deformation of a blanking process. *Computer Methods in Materials Science*, vol. 13, no. 2, p. 333-338.

[5] Wu, X., Bahmanpour, H., Schmid, K. (2012). Characterization of mechanically sheared edges of dual phase steels. *Journal of Materials Processing Technology*, vol. 212, no. 6, p. 1209-1224, **DOI:10.1016/j.jmatprotec.2012.01.006**.

[6] Mucha, J. (2010). An experimental analysis of effects of various material tool's wear on burr during generator sheets blanking. *The International Journal of Advanced Manufacturing Technology*, vol. 50, no. 5, p. 495-507, **DOI:10.1007/s00170-010-2554-1**.

[7] Çöl, M., Kir, D., Erişir, E. (2013). Wear and blanking performance of AlCrN PVD-coated punches. *Materials Science*, vol. 48, no. 4, p. 514-520, **DOI:10.1007/s11003-013-9532-3**.

[8] Wang, C., Chen, J., Yu, X., Xia, C., Ren, F. (2014). Experimental investigations on wear resistance characteristics of different die materials for advanced high-strength steel blanking in close section. *Proceedings of the Institution of Mechanical Engineers, Part B: Journal of Engineering Manufacture*, vol. 228, no. 11, p. 1515-1525, **DOI:10.1177/0954405414521192**.

[9] Bolka, Š., Slavič, J., Boltežar, M. (2015). Identification of out-of-plane material charac-teristics through sheet-metal blanking. *Strojniški vestnik - Journal of Mechanical Engineering*, vol. 61, no. 4, p. 217-226, **DOI:10.5545/sv-jme.2014.2302**.

[10] Subramonian, S., Altan, T., Campbell, C., Ciocirlan, B. (2013). Determination of forces in high speed blanking using FEM and experiments. *Journal of Materials Processing Technology*, vol. 213, no. 12, p. 2184-2190, **DOI:10.1016/j.jmatprotec.2013.06.014**.

[11] Gaudillière, C., Ranc, N., Larue, A., Maillard, A., Lorong, P. (2013). High speed blanking: An experimental method to measure induced cutting forces. *Experimental Mechanics*, vol. 53, no. 7, p. 1117-1126, **DOI:10.1007/s11340-013-9738-1**.

[12] Kanca, E., Eyercioğlu, O., Karahan, I.H., Günen, A., Göv, K. (2016). Effects of blanking speed on the shear surface of mild steel (St37). *Acta Physica Polonica A*, vol. 130, no. 1, p. 370-374, **DOI:10.12693/APhysPolA.130.370**.

[13] Kanca, E., Karahan, I.H., Eyercioglu, O., (2008). Shear-surface improvement of the austenitic stainless steel AISI 304 using high-speed punching. *Optoelectronics and Advanced Materials-Rapid Communications*, vol. 2, no. 12, p. 822-827.

[14] Al-Momani, E.S., Mayyas, A.T., Rawabdeh, I., Alqudah, R. (2012). Modeling blanking process using multiple regression analysis and artificial neural networks. *Journal of Materials Engineering and Performance*, vol. 21, no. 8, p. 1611-1619, **DOI:10.1007/s11665-011-0079-x**.

[15] Hu, D.C., Chen, M.-H., Ouyang, J.D., Yin, L.M. (2015). Finite element analysis of the thermal effect in high-speed blanking of thick sheet metal. *The International Journal of Advanced Manufacturing Technology*, vol. 80, no. 9, p. 1481-1487, **DOI:10.1007/s00170-015-6954-0**.

[16] Magesh, V., Sundar, S., Karuppudaiyan, S. (2016). Finite element analysis of wrinkling and shearing of sheet metal

forming. *Indian Journal of Science and Technology*, vol. 9, no. 34, p. 1-5, **DOI:10.17485/ijst/2016/v9i34/95252**.

[17] Hambli, R., Guerin, F. (2003). Application of a neural network for optimum clearance prediction in sheet metal blanking processes. *Finite Elements in Analysis and Design*, vol. 39, no. 11, p. 1039-1052, **DOI:10.1016/S0168-874X(02)00155-5**.

[18] Hambli, R., Richir, S., Crubleau, P., Taravel, B. (2003). Prediction of optimum clearance in sheet metal blanking processes. *International Journal of Advanced Manufacturing Technologies*, vol. 22, no. 1, p. 20-25, **DOI:10.1007/s00170-002-1437-5**.

[19] Mole, N., Cafuta, G., Štok, B., (2013). A method for optimal blank shape determination in sheet metal forming based on numerical simulations. *Stojniški vestnik - Journal of Mechanical Engineering*, vol. 59, no. 4, p. 237-250, **DOI:10.5545/sv-jme.2012.989**.

[20] Behrens, B., Bouguecha, A., Vucetic, M., Krimm, R., Hasselbusch, T., Bonk, C. (2014). Numerical and experimental determination of cut-edge after blanking of thin steel sheet of DP1000 within use of stress based damage model. *Procedia Engineering*, vol. 81, p. 1096-1101, **DOI:10.1016/j.proeng.2014.10.200**.

[21] Soares, J.A., Gipiela, M.L., Lajarin, S.F., Marcondes, P.V.P. (2013). Study of the punch–die clearance influence on the sheared edge quality of thick sheets. *The International Journal of Advanced Manufacturing Technology*, vol. 65, no. 1-4, p. 451-457, **DOI:10.1007/s00170-012-4184-2**.

[22] Samuel, M. (1998). FEM simulations and experimental analysis of parameters of influence in the blanking process. *Journal of Materials Processing Technology*, vol. 84, no. 1-3, p. 97-106, **DOI:10.1016/S0924-0136(98)00083-1**.

[23] Pepelnjak, T., Magoč, V., Barišič, B. (2012). Analysis of shear hat test in digital environment. *Metalurgija*, vol. 51, no. 2, p. 153-156.

[24] ASM Aerospace Specification Metals Inc. (2016). AISI Type 304 Stainless Steel, from *http://asm.matweb.com/search/SpecificMaterial.asp?bassnum=MQ304A*, accessed on 2016-11-27.

[25] Misumi (2016). Press Dies Tutorial, from *http://www.misumitechcentral.com/tt/en/press/2012/05/124-press-forming-force-1-blanking-force.html*, accessed on 2016-11-28.

Strojniški vestnik - Journal of Mechanical Engineering 63(2017)9, 510-518

DOI:10.5545/sv-jme.2017.4442 Original Scientific Paper
Received for review: 2017-03-09
Received revised form: 2017-06-13
Accepted for publication: 2017-06-29

The Effect of Process Parameters on the Microstructure and Mechanical Performance of Fiber Laser-Welded AA5182 Aluminium Alloys

Celalettin Yuce[1,*] – Mumin Tutar[1] – Fatih Karpat[1] – Nurettin Yavuz[1] – Gökhan Tekin[2]
[1] Uludag University, Department of Mechanical Engineering, Turkey
[2] Coskunöz A.Ş., Turkey

The laser welding of aluminium alloys is an important industrial technology but many challenges remain. The objective of this research is to investigate the effect of laser welding parameters on the quality of the fiber laser lap welded AA5182 aluminium alloy. The influences of the laser power, welding speed and focal point position on the mechanical and microhardness properties of the joints were experimentally investigated. The mechanical properties of the joints were evaluated by performing tensile tests. From the experimental results, optimum process parameters were determined, and microstructural examination and microhardness tests were conducted to better understand the performance of the joints. It was found that there is a correlation between the tensile shear loads of the joints and heat input per unit length. At the optimized parameters, the welded joint showed good weld appearance without macro defects, and the joint had an adequate tensile shear load.

Keywords: fiber laser welding, aluminium alloys, mechanical characterization, microstructural analysis

Highlights

- *Laser power has an increasing effect on the tensile shear load of the joints to a certain value.*
- *The highest tensile load was obtained for 2750 W laser power, 20 mm/s welding speed, and a 100-mm focal point position.*
- *In the fusion zone of the optimum sample, nearly 12 % magnesium loss and some interdendritic shrinkage cavities were detected.*
- *The fusion zone (FZ) of the sample which has a highest tensile shear load, mostly consists of columnar dendritic microstructure and could be divided into two different zones as internal FZ and external FZ.*

0 INTRODUCTION

The growing demand for more fuel-efficient vehicles to reduce energy consumption and air pollution is a challenge for the transport industry. Aluminium is a key material for lightweight structures in vehicles. It allows a mass saving of up to 50 % over competing materials in most applications without compromising safety [1]. Furthermore, aluminium has many advantageous properties, e.g. low density, high strength, excellent formability, good corrosion resistance and recycling potential.

Welding is one of the essential processes for vehicle body manufacturing. Selecting the appropriate welding method is necessary to obtain a proper performance of the welded joint. Over the previous two decades, with the wide application of aluminium alloys in automotive, aerospace and other industries, laser welding has become critical joining method. With its high process speeds, single-sided access, no direct tool contact with the workpiece, and being amenable robotic automation, it proved to be an ideal assembly technology for car body fabrication [2]. In comparison to other conventional welding processes, laser welding offers the benefit of a narrow heat-affected zone that helps to minimize metallurgical problems [3]. Although aluminium alloys have many advantages, there are some problems are encountered with welding these alloys [4]. The wide range of temperatures in vaporization and solidification can lead to keyhole instability, blowholes, porosity and various defects in the welding metallurgy, such as hot cracking [5]. The loss of alloying elements is another problem Furthermore, there is a poor coupling of the laser energy due in part to the high density of free electrons in the solid, making aluminium one of the best reflectors of light [6].

These problems from the welding aluminium alloys and mechanical properties of the joints are directly influenced by process parameters; the effect of these parameters on the weld quality was investigated by several researchers in the literature. Sanchez-Amaya et al. [6] investigated laser welded 5083 and 6082 aluminium alloys under conduction mode and found that welding speed was more influential than laser power on the final size of the weld bead. Yang et al. [7] examined the effect of the incident beam position, incident beam angle and beam separation distance on weld quality. The results indicated that weld penetration was increased significantly as the

*Corr. Author's Address: Uludag University, Department Mechanical Engineering, Turkey, cyuce@uludag.edu.tr

incident beam angle increased. Ancona et al [8] conducted laser butt welding of AA5083 aluminium alloy. They used the design of the experiment technique to investigate the effects of the variables on the mechanical properties and porosity level and stated that in terms of tensile load the best results were found for high powers and high welding speeds. Kim et al. [9] investigated the effects of the parameters on the AA5052 aluminium alloy weldability. They indicated that the bead quality was improved when the beam was defocused in comparison to focus on the material surface position. Wang et al. [10] reported the effect of different beam oscillating pattern on the weld characterization of aluminium alloys. They indicated that beam oscillation has no effect on weld strength but an obvious effect on elongation.

Katayama et al. [11] investigated the effect of process parameters on the penetration and defect formation of the bead on plate welded AA5083 aluminium alloys. They reported that the weld beads were narrower and deeper with an increase in the power density. El-Batahgy and Kutsuna [12] clarified the effect of welding parameters on the porosity level and solidification cracking and they found that the tendencies for porosity and solidification cracking were increased at high welding speed conditions. Chang et al. [13] showed that the welding defect rate of the pulsed wave type was larger than that of the continuous type, and the crack rate was reduced with decreasing welding speed. Kim and Park [14] investigated the effect of the process variables on the tensile strength of the laser welded 5J32 aluminium alloy. Wang et al. [15] stated that the solidification duration of the molten pool is the key factor for porosity. Zhang et al. [16] evaluated the microstructural and mechanical properties of the laser welded new type of Al–Zn–Mg–Cu alloy sheets. They stated that the ultimate tensile strength of the joint was 69.7% of that of the base material tensile strength and those samples of the tensile tests were always fractured at the weld bead. Yang et al. [17] investigated the application of dual-beam laser in the conduction welding mode for aluminium panels in a coach-peel joint configuration. They stated that cross-beam laser joined parts provided the best weld surface quality.

In recent decades, the laser welding of aluminium alloys has attracted more attention owing to its remarkable advantages over other joining processes. Many experimental and theoretical studies have been made to understand the laser welding phenomenon in several industries [18] to [20]. However, there is still a lack of information about the effect of fiber laser welding process parameters on the microstructural and mechanical properties of materials with large heat conductivity or with volatile chemical elements, such as the 5xxx series. For these alloys, proper welding parameter range is usually narrow and difficult to be found because the keyhole and weld pool may violently fluctuate in the welding process [21]. In the present study, laser lap welding was performed with AA5182 aluminium alloy in order to conduct basic investigations into the effects of welding process parameters on the mechanical and microstructural properties of the joints. The process parameters considered in the experiments were the laser power, welding speed, and focal point position. The weldability evaluation used microstructural and microhardness examination of the cross section, and tensile tests to express the mechanical properties.

1 MATERIALS AND METHOD

The present study was performed on rolled sheets of AA5182 aluminium alloy with a thickness of 2 mm. Its chemical composition is shown in Table 1. AA5182 alloy is an important commercial aluminium alloy with high strength, high ductility, high corrosion resistance, and good formability. It has been widely used for the manufacturing of automobile components. In recent years, it has also been considered for car body sheets.

Table 1. *Chemical composition of AA5182 alloy*

Element	Si	Fe	Mn	Mg	Cu	Zn
[wt %]	0.2	0.3	0.4	4.5	0.1	0.25

The dimensions of each sheet were 140 mm in length, 140 mm in width, and 2 mm in thickness. The gap between two sheets was kept tight during welding. Before welding strict chemical cleaning was applied to the welded surfaces in order to reduce possible oxide film and other residues. The configuration and geometry of overlap joint and clamped welding sample are shown in Figs. 1a and b.

Welds were made using an IPG Ytterbium fiber laser system (YLS—3000) attached to a Kuka robotic arm. The maximum average power of the laser was 3000 W of the continuous laser with 1070 nm wavelength. During the welding, the incident angle of the laser was fixed at 6° (i.e. forward inclination) to prevent damage to the optics due to back reflection. Helium was utilized as a shielding gas with a flow rate of 11 l/min from a side nozzle angle at 45º directed forward. The process variables of this study were laser power, welding speed, and focal point position. At a focal point position of 100 mm laser beam is focused

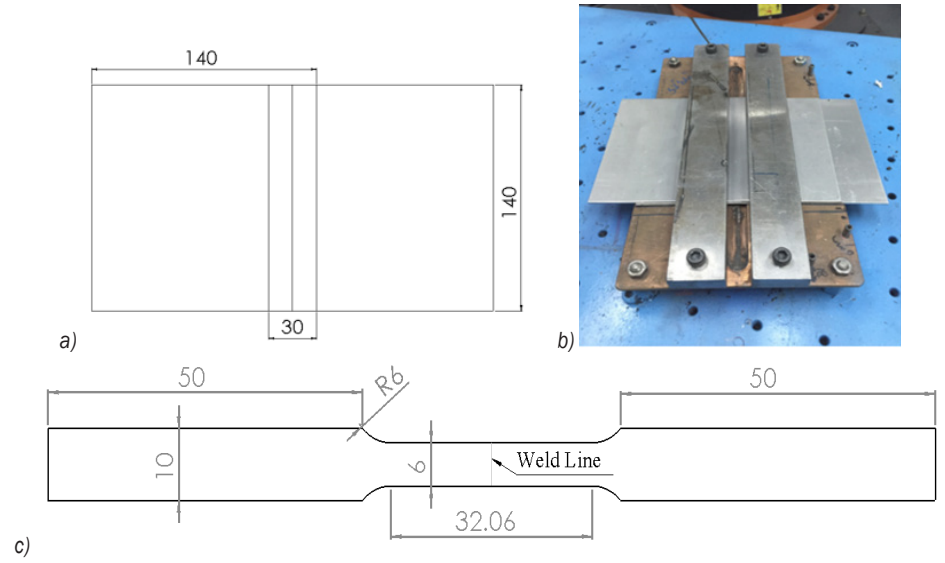

Fig. 1. *a) Geometry of laser welded lap joint, b) clamped sample, and c) dimension of the tensile test specimen*

on the top sheet surface. Welding conditions and levels of the process variables are shown in Table 2. The levels of the process parameters were chosen based on previous studies in the literature and pilot experiments were carried out to determine the practical operating range of each individually selected process parameters in order to produce a weld of acceptable quality.

For the metallographic characterization and microhardness measurement, the welded joints were cross-sectioned through the weld bead centre, using an electrical-discharge cutting machine. The cross-sectioned samples were mounted in Bakelite, then ground and polished successively with a 1 µm and 0.3 µm Al_2O_3 suspension, respectively. Two different etching procedures were conducted to reveal the grain boundaries and weld zone microstructure. The first of these was 0.5 ml HF in 100 ml H_2O solution. To reveal some microstructures, subsequently, polished specimens were tint etched using Weck's reagent which consists of 100 ml H_2O, 4 g $KMnO_4$, and 1 g NaOH. Then, etched samples were analysed for microstructural changes, atomic percent of the alloying elements and possible defects using a Nikon DIC optic microscope (OM) with a Clemex image analysis system and Zeiss EVO 40 XVP scanning electron microscope (SEM) complemented by energy-dispersive spectroscopy (EDS). Vickers microhardness measurements were performed on a DUROLINE-M microhardness tester using a diamond pyramid indenter with a 50-g load, and 10 s dwell time; five readings were taken from which the average was determined. To determine the tensile shear load of the laser welded joints, the test samples were prepared based on the ASTM-E8 standards (Fig. 1c). Tensile shear tests were performed using a fully computerized UTEST-7014 tensile testing machine at room temperature using a constant crosshead speed of 5 mm/min.

2 RESULTS AND DISCUSSION

2.1 Effect of Process Parameters on the Tensile Shear Load

The major welding parameters that affect the quality of laser welded joints are laser power, welding speed, and focal point position. Compared with steel, due to the Al alloys having higher initial reflectivity to laser beams and greater thermal conductivity, greater power densities are needed to achieve keyhole welding. Therefore, laser power, spot size, and the welding speed are important variables for the welding process. All the average tensile test results for the different process variables were reported in Table 2. An average of four test results of the tensile load (TL) was calculated for each sample and the maximum standard deviation was 0.20.

The effect of the laser power of 2.25 kW, 2.5 kW, 2.75 kW and 3 kW on the tensile load of the joint was investigated at a constant welding speed of 20 mm/s and 100 mm focal point position. Tensile test results were shown in Fig. 2. As shown in the results, laser power has a positive effect on the tensile shear load of the joints to a certain value. With increasing laser power after 2.75 kW at a constant welding speed (20

mm/s) tensile load of the joint was decreased. When the laser power was too high, excessive heat input caused excessive penetration and evaporation of the weld bead; therefore, the tensile load of the joints was decreased. However, if the laser power was too low, the coupling of laser energy to workpiece and penetration may be lost. A decrease in the depth of penetration was observed as the heat input decreased due to the low laser power levels. Thus, the tensile load of the weld was decreased. Therefore, to obtain a maximum tensile load, both laser power and heat input per unit length should be at a certain level. In this study, the maximum tensile load was obtained at the laser power of 2.75 kW at a constant welding speed of 20 mm/s and focal point position of 100 mm.

Table 2. *Parameter combinations and average tensile test results*

Laser power [kW]	Welding speed [mm/s]	Focal point position [mm]	Avg. TL [kN]
For constant laser power and focal position			
3	10	100	0.70
3	20	100	1.53
3	30	100	1.23
3	40	100	1.08
For constant welding speed and focal position			
2.25	20	100	1.18
2.5	20	100	1.30
2.75	20	100	1.60
3	20	100	1.53
For constant laser power and welding speed			
2.75	20	95	1.38
2.75	20	100	1.60
2.75	20	105	1.08
2.75	20	110	0.96

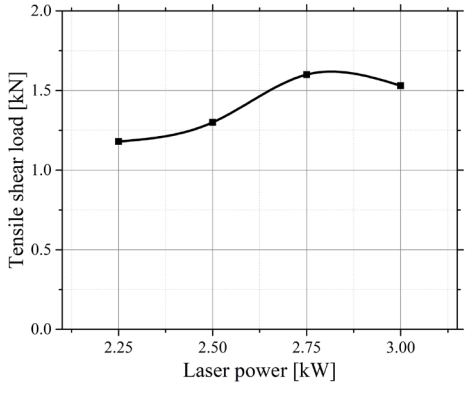

Fig. 2. *Effect of laser power on TL of joints*

The effect of four different welding speeds (10 mm/s, 20 mm/s, 30 mm/s, and 40 mm/s) on the tensile load of the joint was investigated at a constant laser power of 3 kW and focal point position of 100 mm. The results of tensile tests are shown in Fig. 3. As can be seen, tensile load values of the joints were relatively low at a welding speed of 10 mm/s. This is because too low a welding speed leads to excessive melting, loss of material, and weld perforation due to excessive heat input. At a constant laser power and the focal point position, the maximum tensile load was obtained at a welding speed of 20 mm/s. Because the penetration depth was inversely proportional to the welding speed for a given focal position and power, an increase in welding speed at constant power results in a corresponding decrease in penetration depth because of the reduction in the heat input [13]. Therefore, at welding speeds of 30 mm/s and 40 mm/s, the tensile load of the joints was decreased.

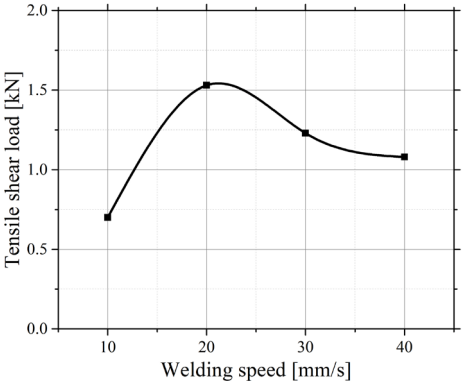

Fig. 3. *Effect of welding speed on TL of joints*

Focal point position is the distance between the laser head and material surface. It determined the spot size and consequently the energy density on the sheet surface. The effect of focal point positions of 95 mm, 100 mm, 105 mm, and 110 mm on the tensile load of the joint was investigated at a constant welding speed of 20 mm/s and laser power of 2.75 kW. Tensile load results are shown in Fig. 4. When the focal point position was 100 mm, the diameter of the laser spot was minimal. At this focal point position (100 mm), the laser beam was focused on the top aluminium sheet surface. Increasing or decreasing the point position resulted in the remarkable effect on the penetration depth and surface quality of the joints. When the focal point position was 100 mm, the maximum penetration depth occurred. Therefore, the tensile load of this level was maximum. The focal position was 105 mm and 110 mm penetration depth was shallow. However, if the focal point position was too far below the sheet surface, in this case, 95 mm, weld depth and weld width decreased, and the tensile load of the joint

decreased. Furthermore, when the focal point position was too far above the sheet surface (105 mm and 110 mm) the diameter of the laser spot was increased and energy density on the surface was decreased [11]. Thus, penetration depth and tensile load decreased.

According to the obtained experimental results, tensile load, penetration depth, and weld seam width were related to the process parameters. All the parameters and material properties and thicknesses should be considered when selecting the appropriate process parameters to obtain desired weld quality. It was found that penetration depth was related to the heat input so laser power and welding speed were determined properly. For complete penetration, using lower laser power with lower welding speed is required, but it is not acceptable from the view of productivity and the visual quality of the weld bead. Conversely, under increased welding speed and decreased laser power conditions, the heat input was decreased and full penetration did not occur. In terms of weld seam width, laser power was proportional to weld seam width. Weld seam width was increased as laser power increased. Welding speed affected the weld in the opposite way. Furthermore, focal point position influenced the weld width. The best performance was obtained for 2.75 kW laser power, 20 mm/s welding speed and the 100-mm focal point position.

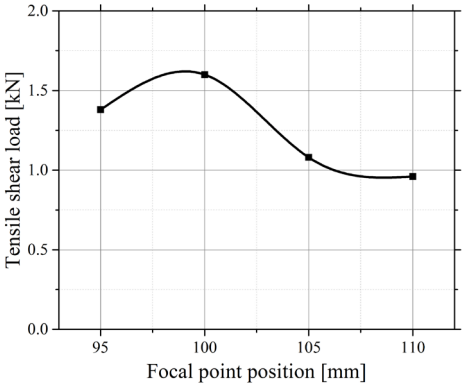

Fig. 4. Effect of focal position on TL of joints

2.2 Microhardness and Microstructural Examination

A selected sample, which has a maximum tensile load, was used for the evaluation of mechanical properties via microhardness measurement and microstructural examination using OM and SEM-EDS. Micrographs of the selected welded joint made using 2.75 kW laser power, 20 mm/s welding speed, 100 mm focal point position are shown in Fig. 5.

Typically, three distinct zones were observed: the fusion zone (FZ), the heat-affected zone (HAZ), and base metal (BM). Although it was the sample showing best performance, in this sample, partial penetration was obtained. FZ mostly consists of columnar dendritic microstructures and could be divided into two different zones: internal FZ and external FZ.

With a narrow transition zone containing columnar and misoriented dendrites, the internal FZ is characterized by a fine precipitation of the second phases in a solid solution matrix of aluminium (Fig. 5a). External FZ showed a columnar dendritic structure due to a high cooling rate depending on the direction of heat flow (Fig. 5b). In addition, a few grain-sized HAZ were obtained near the fusion line (Fig. 5c).

The sample was also examined for possible defects. There was no crack in the FZ, however, some small defects were observed. The most discussed defect was hydrogen-related pores in the welding of aluminium alloys. Due to the deposition of supersaturated hydrogen in the weld pool, it was gathering and growing until finally it was too late for it to escape during the cooling process so it forms large regular circle-shaped pores with smooth walls, as can be seen in Fig. 6a.

The pores could also form because of the surface contamination resulting from inadequate cleaning and shielding gas or engulfed metal vapor. Especially, in the keyhole regime conventional heat transfer between solid-liquid interface and collapse of liquid metal causes the occurrence of pores [22] and [23]. The optimum sample was also analysed with EDS. The analyses results showed that in the fusion zone nearly 12 % magnesium loss was encountered, with respect to the BM. This finding is in good agreement with the studies in the literature [24] and [25]. It is believed that the pore in Fig. 6b could be formed due to these reasons. Furthermore, some interdendritic shrinkage cavities have been detected.

In the SEM examination of the optimum sample, white particles were found in the fusion zone. They were considered to be iron-bearing particles. Additionally, it should be noted that some interdendritic cavities were found (Fig. 7a). The side surfaces of some cavities, shown with arrows, have a bright white layer (Fig. 7b). Due to the similarity of as-welded microstructure with as-cast microstructure and the presence of oxygen content in the FZ (confirmed with EDS analysis), these layers could be considered oxide layers [26] and [27]. Although shielding gas was used and pre-cleaning of the sheet surfaces was carried out, the presence of the oxides means that

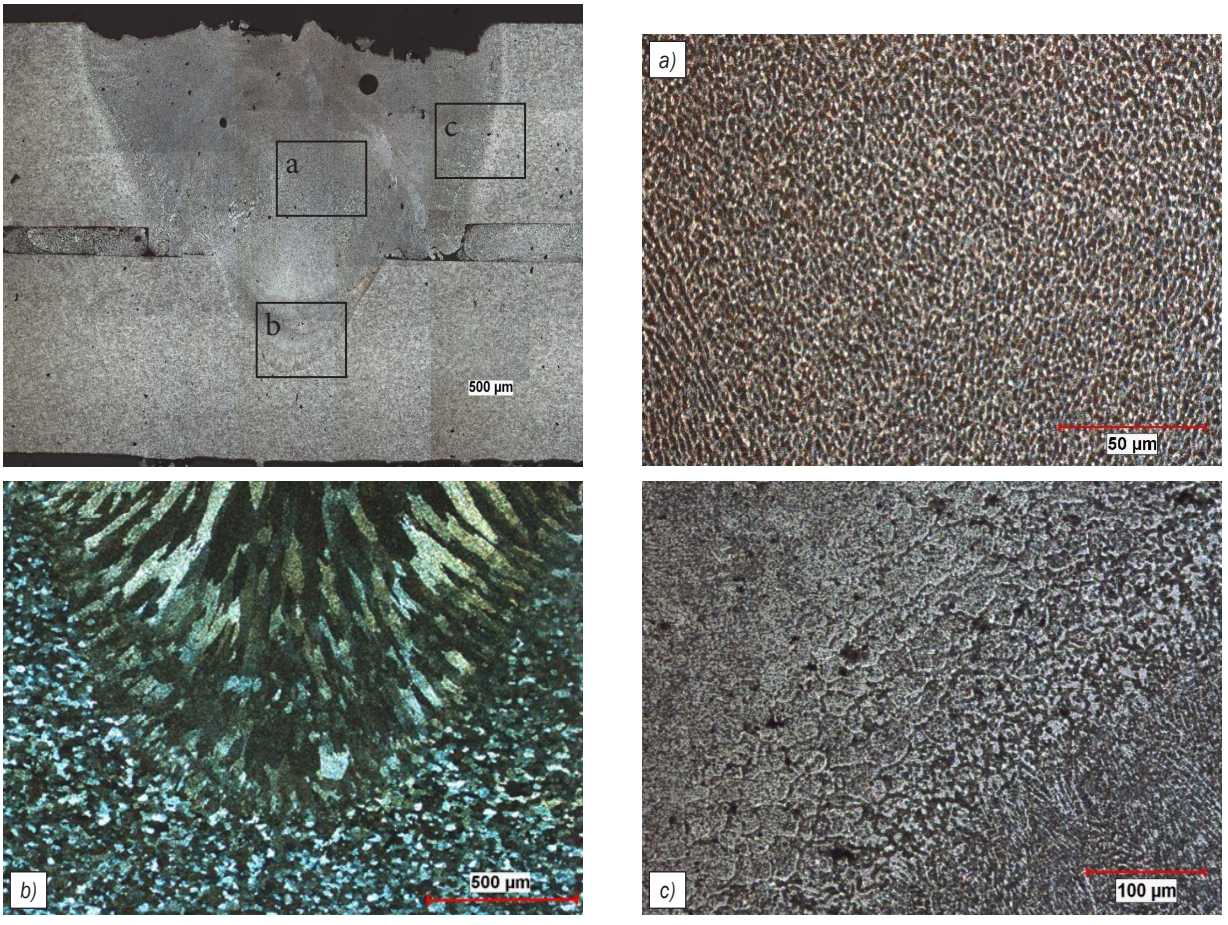

Fig. 5. *Optical micrographs showing the optimum sample weld cross section, FZ and HAZ in detail: a) the internal FZ b) the external FZ, and c) the edge of the HAZ*

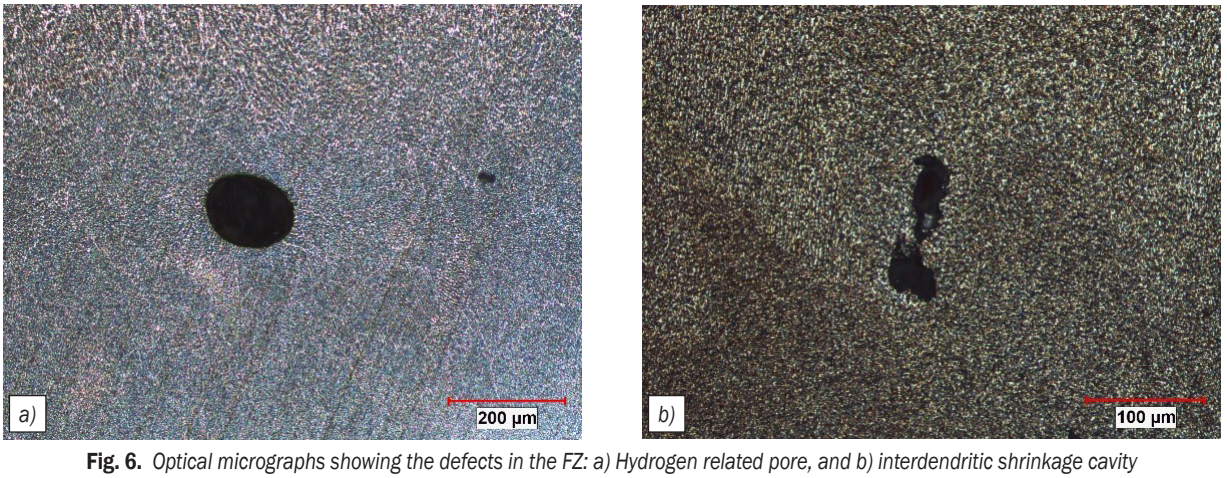

Fig. 6. *Optical micrographs showing the defects in the FZ: a) Hydrogen related pore, and b) interdendritic shrinkage cavity*

the shielding gas rate and/or pre-cleaning can be considered insufficient for the process parameters of the selected sample.

Microhardness tests were performed in order to characterize the weld-affected area, including FZ (external and internal part), HAZ and the BM surrounding the bead. The microhardness map is shown in Fig. 8, measured on a cross-section according to ASTM E 384-99. Microhardness value of the BM was 83 HV. The hardness of the internal

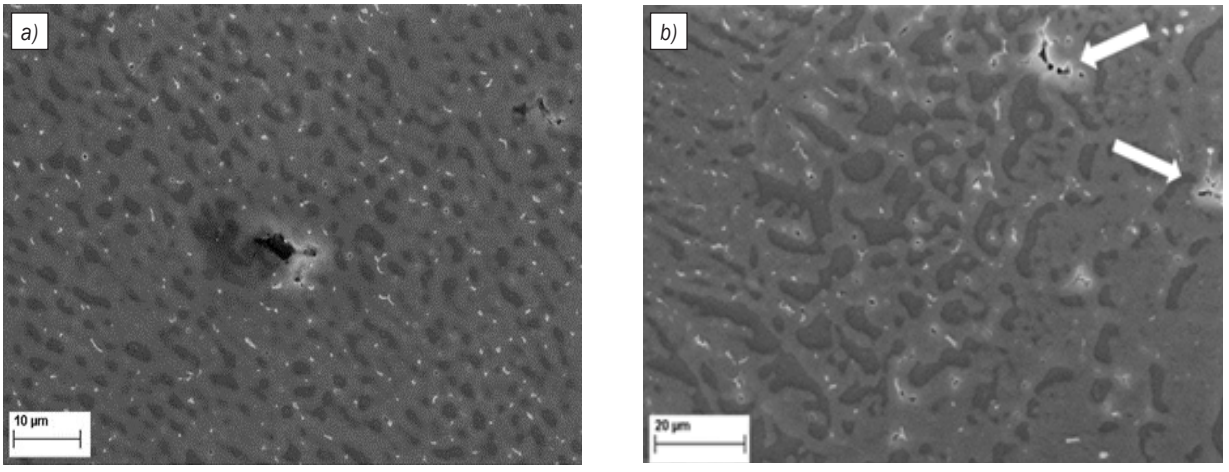

Fig. 7. *SEM micrographs of: a) iron-bearing particles, and b) interdendritic cavity surfaces*

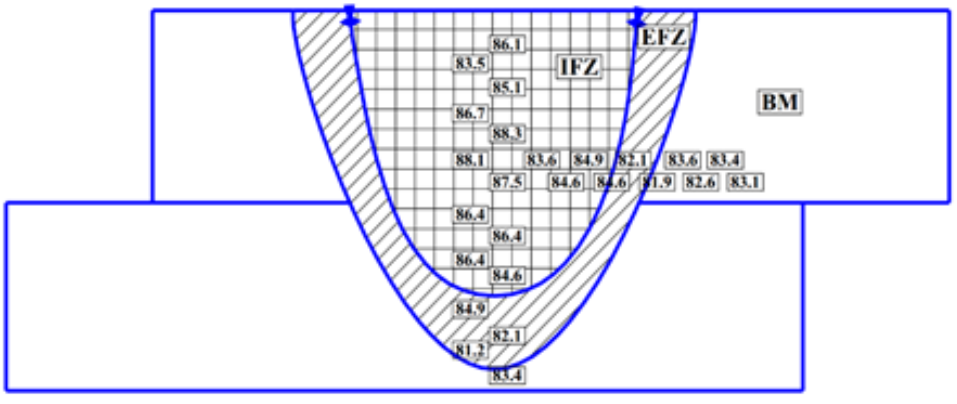

Fig. 8. *Microhardness profiles of the optimum sample*

FZ (IFZ) and external FZ (EFZ) are 86.8 HV and 83.5 HV, respectively. As can be seen, the microhardness value of the FZ is slightly higher than that of the BM. The increase of the microhardness in the FZ has been reported by some researchers, especially in the non-heat treatable alloys with O temper condition **[6]** and **[25]**. This is due to the microstructural refinement of the fusion zone with respect to the metal base. Since the width of the HAZ was smaller than the step size of microhardness measurement, the microhardness of the HAZ could not be measured clearly with the selected force. However, the hardness of the HAZ is roughly 82 HV.

3 CONCLUSIONS

In the present work, the fiber laser lap-welding experiments of AA5182 aluminium alloys were conducted. The effects of the laser power, welding speed and focal point position on the tensile load of the joints were investigated. Microstructural and microhardness examination of the optimum sample, which has the highest tensile load, was conducted.

According to the obtained experimental results, tensile load, penetration depth, and weld seam width were related to the process parameters. Concerning the tensile loads and bead profiles of the joints, it is observed that excessive heat input caused excessive penetration and evaporation of the weld bead so the tensile load of the joints was decreased. Conversely, insufficient heat input resulted in a decrease of the penetration depth, so tensile load was decreased. Therefore, heat input per unit length which depends on the laser power and welding speed should be selected carefully. Furthermore, experimental results showed that focal point position had an effect on the weld width and penetration depth. In this work, the highest tensile load was obtained for 2750 W laser power, 20 mm/s welding speed, and 100 mm focal point position.

The microstructural examination was conducted using OM, SEM, and EDS analyses. The microstructure of different zones of the optimum sample was examined. FZ mostly consists of columnar dendritic microstructures and could be divided into two different zones: internal FZ and external FZ. A few grain-sized HAZ were obtained in the vicinity of the fusion line. Small size defects were observed in the FZ. These were considered to be induced depositions of supersaturated hydrogen and interdendritic shrinkage cavities. As a result of the microhardness examination, due to the microstructural refinement of the fusion zone, hardness values were slightly increased in this zone. According to the EDS analysis in the fusion zone, nearly 12 % magnesium loss encountered, with respect to the BM. Moreover, in the SEM examination, iron-bearing particles were found in the fusion zone.

4 ACKNOWLEDGEMENTS

The authors acknowledge the Uludag University Commission of Scientific Research Projects under Contract No. OUAP(MH)-2016/6 for supporting this research. And a part of this research was supported by the Coskunöz Holding Research and Development Department at Bursa, Turkey.

5 REFERENCES

[1] Hirsch, J. (2014). Recent development in aluminum for automotive applications. *Transactions of Nonferrous Metals Society of China* vol. 24, no. 7, 1995-2002, **DOI:10.1016/S1003-6326(14)63305-7**.

[2] Rejc, J., Munih, M. (2016). Robust visual touch-up calibration method in robot laser spot welding application. *Strojniški vestnik - Journal of Mechanical Engineering*, vol. 62, no. 12, p. 697-708, **DOI:10.5545/sv-jme.2016.3708**.

[3] Pakdil, M., Cam, G., Kocak, M., Erim, S. (2011). Microstructural and mechanical characterization of laser beam welded AA6056 Al-alloy. *Materials Science and Engineering A*, vol. 528, no. 24, p. 7350-7356, **DOI:10.1016/j.msea.2011.06.010**.

[4] Cao, X., Wallece, W., Immarigeon, J.-P., Poon, C. (2007). Research and progress in laser welding of wrought aluminum alloys. II. Metallurgical microstructures, defects, and mechanical properties. *Materials and Manufacturing Processes*, vol. 18, no. 1, p. 23-49 **DOI:10.1081/AMP-120017587**.

[5] Viscusi, A., Leitão, C., Rodrigues, D.M., Scherillo, F., Squillace, A., Carrinoa, L. (2016). Laser beam welded joints of dissimilar heat treatable aluminium alloys. *Journal of Materials Processing Technology*, vol. 236, p. 48-55, **DOI:10.1016/j.jmatprotec.2016.05.006**.

[6] Sánchez-Amaya, J.M., Delgado, T., González-Rovira, L., Botana, F.J. (2009). Laser welding of aluminium alloys 5083 and 6082 under conduction regime. *Applied Surface Science*, vol. 255, no. 23, p. 9512-9521, **DOI:10.1016/j.apsusc.2009.07.081**.

[7] Yang, Z.B., Tao, W., Li, L.Q., Chen, Y.B., Li, F.Z., Zhang, Y.L. (2012). Double-sided laser beam welded T-joints for aluminum aircraft fuselage panels: Process, microstructure, and mechanical properties. *Materials & Design*, vol. 33, p. 652-658, **DOI:10.1016/j.matdes.2011.07.059**.

[8] Ancona, A., Lugara, P.M., Sorgente, D., Tricarico, L. (2007). Mechanical characterization of CO_2 laser beam butt welds of AA5083. *Journal of Materials Processing Technology*, vol. 191, no. 1-3, p. 381-384, **DOI:10.1016/j.jmatprotec.2007.03.048**.

[9] Kim, J.-K., Lim, H.-S., Cho, J.-H., Kim, C.-H. (2008). Weldability during the laser lap welding of Al 5052 sheets. *Archives of Materials Science and Engineering*, vol. 31, no. 2, p. 113-116.

[10] Wang, L., Gao, M., Zhang, C., Zeng, X. (2016). Effect of beam oscillating pattern on weld characterization of laser welding of AA6061-T6 aluminum alloy. *Materials & Design*, vol. 108, p. 707-717, **DOI:10.1016/j.matdes.2016.07.053**.

[11] Katayama, S., Nagayama, H., Mizutani, M., Kawahito, Y. (2009). Fibre laser welding of aluminum alloy. *Welding International*, vol. 23, no. 10, p. 744-752, **DOI:10.1080/09507110902836911**.

[12] El-Batahgy, A., Kutsuna, M. (2009). Laser beam welding of AA5052, AA5083, and AA6061 aluminum alloys. Advances in Materials Science and Engineering, Article ID 974182, **DOI:10.1155/2009/974182**.

[13] Chang, C.C., Chou, C.P., Hsu, S.N., Hsiung, G.Y., Chen, J.R. (2010). Effect of laser welding on properties of dissimilar joint of Al-Mg-Si and Al-Mn aluminum alloys. *Journal of Materials Science & Technology*, vol. 26, no.3, p. 276-282, **DOI:10.1016/S1005-0302(10)60046-1**.

[14] Kim, D.Y., Park, Y.W. (2012). Weldability evaluation and tensile strength estimation model for aluminum alloy lap joint welding using hybrid system with laser and scanner head. *Transactions of Nonferrous Metals Society of China*, vol. 22, suppl. 3, p. 596-604, **DOI:10.1016/S1003-6326(12)61771-3**.

[15] Wang, J., Wang, G.Z., Wang, C.M. (2015). Mechanisms of the porosity formation during the fiber laser lap welding of aluminum alloy. *Metalurgija*, vol. 54, no. 4, p. 683-686.

[16] Zhang, L., Li, X., Nie, Z., Huang, H., Sun, J. (2015). Microstructure and mechanical properties of a new Al–Zn–Mg–Cu alloy joints welded by laser beam. *Materials & Design*, vol. 83, p. 451-458, **DOI:10.1016/j.matdes.2015.06.070**.

[17] Yang, G., Ma, J., Carlson, B., Wang, H.P. Kovacevic, R. (2017). Effect of laser beam configuration on microstructure evolution and joint performance in laser joining AA 6111 panels. *Materials & Design*, vol. 123, p. 197-210, **DOI:10.1016/j.matdes.2017.03.050**.

[18] Kim, S., Lee, W., Kim, D. (2015). One-step distortion simulation of pulsed laser welding with multi-physics information. *International Journal of Simulation Modelling*, vol. 14, no. 1, p. 85-97, **DOI:10.2507/IJSIMM14(1)8.291**.

[19] Shibib, K.S., Minshid, M.A., Tahir, M.M. (2009). Finite element analysis of spot laser of steel welding temperature history. *Thermal Science*, vol. 13, no. 4, p. 143-150, **DOI:10.2298/TSCI0904143S**.

[20] Vegelj, D., Zajec, B., Gregorčič, P., Možina, J. (2014). Adaptive pulsed-laser welding of electrical laminations. *Strojniški*

vestnik - Journal of Mechanical Engineering, vol. 60, no. 2, p. 106-114, **DOI:10.5545/sv-jme.2013.1407**.

[21] Pang, S., Chen, W., Zhou, J., Liao, D. (2015). Self-consistent modeling of keyhole and weld pool dynamics in tandem dual beam laser welding of aluminum alloy. *Journal of Materials Processing Technology*, vol. 217, p. 131-143, **DOI:10.1016/j.jmatprotec.2014.11.013**.

[22] Haboudou, A., Peyre, P., Vannes, A.B., Peix, G. (2003). Reduction of porosity content generated during Nd:YAG laser welding of A356 and AA5083 aluminium alloys. *Materials Science and Engineering A*, vol. 63, no. 1-2, p. 40-52, **DOI:10.1016/S0921-5093(03)00637-3**.

[23] Yang, J., Gang, S., Li, X., Chen, L., Xu, F. (2010). Typical joint defects in laser welding of Aluminium-Lithium alloy. *Proceedings of the 36th International MATADOR Conference*, p. 595-598, **DOI:10.1007/978-1-84996-432-6_130**.

[24] Sibillano, T., Ancona, A., Berardi, V., Schingaro, E., Basile, G., Lugarà, P.M. (2006). A study of the shielding gas influence on the laser beam welding of AA5083 aluminium alloys by in-process spectroscopic investigation. *Optics and Lasers in Engineering*, vol. 44, no. 10, p. 1039-1051, **DOI:10.1016/j.optlaseng.2005.09.002**.

[25] Sanchez-Amaya, J.M., Delgado, T., Damborenea, J., Lopez, V., Botana, F.J. (2009). Laser welding of AA 5083 samples by high power diode laser. *Science and Technology of Welding and Joining*, vol. 14, no, 1, p. 78-86, **DOI:10.1179/136217108X347629**.

[26] Li, Y.J., Arnberg, L. (2004). A eutectoid phase transformation for the primary intermetallic particle from Alm(Fe,Mn) to Al3(Fe,Mn) in AA5182 alloy. *Acta Materialia*, vol. 52, no. 10, p. 2945-2952, **DOI:10.1016/j.actamat.2004.02.041**.

[27] Li, Y.J., Arnberg, L. (2004). Solidification structures and phase selection of iron-bearing eutectic particles in a DC-cast AA5182 alloy. *Acta Materialia*, vol. 52, no. 9, p. 2673-2681, **DOI:10.1016/j.actamat.2004.02.015**.

Strojniški vestnik - Journal of Mechanical Engineering 63(2017)9, 519-528

DOI:10.5545/sv-jme.2016.4282 Original Scientific Paper
Received for review: 2016-12-19
Received revised form: 2017-05-23
Accepted for publication: 2017-07-03

Neural Network-Based High-Accuracy Motion Control of a Class of Torque-Controlled Motor Servo Systems with Input Saturation

Lei Liu – Jian Hu* – Yuangang Wang – Zhiwei Xie
Nanjing University of Science & Technology, School of Mechanical Engineering, China

The torque-controlled motor servo system is widely used in many industrial applications. However, input saturation often occurs due to the limitation of the actuator output ability, which may worsen the system control performance. In this paper, in order to inhibit the impact of input saturation on the system, a single-hidden-layer neural network based observer is designed to estimate the value of input saturation, which could later be compensated in the proposed controller. In addition, an adaptive law is introduced to estimate the unknown parameters, and a nonlinear robust term is designed to overcome the time-varying disturbances and other compensation errors. The Lyapunov theorem is used to prove the stability of the proposed controller with the neural network-based observer. Extensive comparative experimental results are obtained to verify the high-performance of the proposed control strategy.

Keywords: torque-controlled motor, input saturation, adaptive robust control, neural network, disturbance

Highlights

- *Input saturation has been considered when establishing the model of motor servo system.*
- *Both the parametric uncertainty and the external disturbance have been considered when designing the controller.*
- *A single-hidden-layer neural network has been adopted to estimate the input saturation, which cannot be measured.*
- *Experimental results show the effectiveness of the proposed control strategy.*

0 INTRODUCTION

The torque-controlled motor servo system has been widely used in the industrial applications in recent years due to its low pollution and high efficiency compared with its hydraulic counterpart [1]. How to design a high-performance controller for the motor servo system has been a topic of great interesting in domestic and foreign research fields [2]. Adaptive control of nonlinear systems has received much attention for obtaining the global asymptotical stability of the closed-loop system [3]. However, all kinds of uncertainties always exist in the system, and these uncertainties could deteriorate the systematic control performance severely [4]. Input saturation is one such uncertainty in the motor servo system, and the typical input saturation is shown in Fig. 1. When the input of the actuator reaches a certain limit value, the output of the actuator does not increase with the increase of the input, which is defined as input saturation. Input saturation can deteriorate the dynamic performance and even result in the instability of the system [5].

To deal with the input saturation, one approach is to introduce an additional system to analyse the effect of it. The states of the auxiliary system are employed for controller design and stability analysis [6]. In [7], an auxiliary design system is introduced to analyse the input saturation effect. In [8], in order to overcome the problem of input saturation, a new

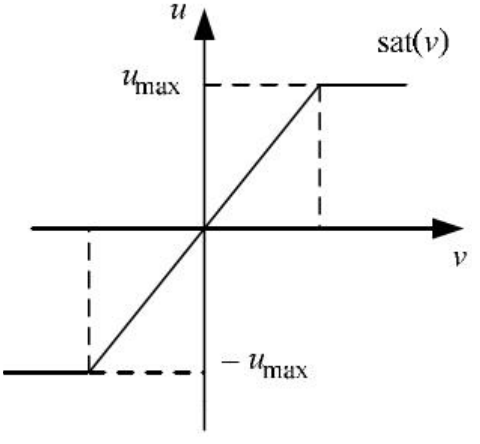

Fig. 1. *The diagram of typical input saturation nonlinearity*

auxiliary design system and Nussbaum gain functions are incorporated into the control scheme. The control performance could be improved by establishing this kind of auxiliary system, but the model of the system becomes complex, which makes it difficult to be used in engineering applications. A second approach simply takes the input saturation as a kind of disturbance, and an observer is designed for it. An RBF neural network disturbance observer [9], a sliding-mode observer [10] and fuzzy state observer [11] are developed to estimate

*Corr. Author's Address: Nanjing University of Science & Technology, No.200, Xiaolingwei, Nanjing, China, hujian_njust@163.com

the unknown disturbance, and the estimation error converges to a compact set if the observer's parameters are selected appropriately. In [12], the effects of the control singularity and unknown input saturation along with the external disturbance are approximated by a disturbance observer. In [13], fuzzy logic systems are used to approximate the unknown nonlinear functions. Then, the disturbance including the input saturation could be observed and compensated in the controller. Thus, a better tracking accuracy could be obtained and the stability of the system could be guaranteed. However, when the external disturbance is large while the input saturation is relatively small, it is very difficult to eliminate the effect caused by input saturation with the disturbance compensation term.

Another approach involves the establishment of a smooth function to approximate the input saturation nonlinear characteristics [14] to [16]. In [14], a dynamic signal and smooth function in a non-affine structure subject to the control input signal are introduced to handle the un-modelled dynamics and input saturation. In [15], the input saturation is approximated by a smooth function, and a fuzzy state observer is designed for estimating the unmeasured states. In [16], a smooth nonlinear function of the control input signal is first introduced to approximate the saturation function to overcome the effect of non-differential saturation nonlinearity. This method restricted the input saturation nonlinearity, but the authenticity of the system is lost. There are still some other ways to deal with the effects of input saturation. For example, the non-affine problem of input saturation is solved by a mean value theorem in [17]. A new adaptive sliding mode control scheme is proposed to guarantee the globally asymptotic convergence of a motion system despite the presence of control input constraint, parametric uncertainties, and external disturbances in [18]. This method could directly overcome the impact of input saturation on the system by adjusting the controller's parameters, but the tracking performance is not sufficient. A single controller is introduced in [19] to constrain the influence caused by input saturation. It can obtain better tracking accuracy, but the robustness of the system simultaneously decreased.

According to the above analysis, all the proposed controllers have both advantages and disadvantages. In this paper, an adaptive robust control method is proposed to improve the tracking accuracy of motion systems driven by torque-controlled motors with input saturation. Considering the universal approximation ability of neural networks (NN) [20] and [21], a kind of single-hidden layer parameter linearized NN [22] is designed to approximate the input saturation, and the input saturation is compensated effectively later in the controller. The experiment results verify the validity of the proposed controller. This method considers both the input saturation and the disturbance in the system, therefore, it has better performance than the other controllers do.

This paper is organized as follows. The dynamics of a motor servo system are established in Section 2. Section 3 designs an adaptive robust controller with a NN-based observer in detail. A Lyapunov stability proof and analysis has also been given in this part. Extensive experiments are carried out in Section 4, and the conclusions are given in Section 5.

1 DYNAMICS OF A TORQUE-CONTROLLED MOTOR SERVO SYSTEM

In this part, an accurate model of a torque-controlled motor servo system is established. A torque-controlled motor servo system is usually composed of a torque-controlled motor, a servo driver, a position controller, a reducer, sensors, and so on [23] and [24]. The systematic diagram is shown in Fig. 2.

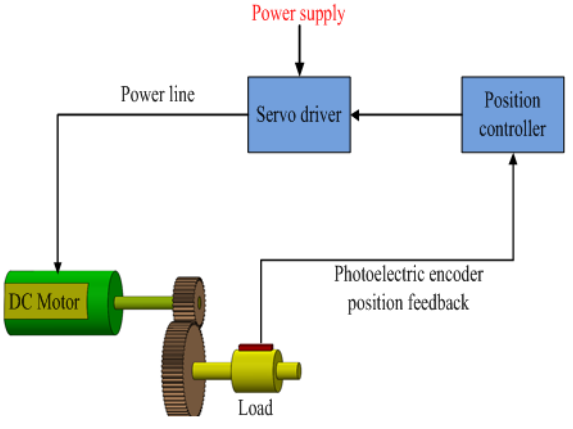

Fig. 2. *Specific composition diagram of the motor servo system*

In order to improve the tracking precision of the system, the system parametric uncertainty and other nonlinearities, such as the external disturbance, should be considered when establishing the system's model. The external disturbance of the system should be divided into two parts. One is the constant disturbance, and the other is the time-varying disturbance. Furthermore, the input saturation should also be considered when modelling. In addition, only the mechanical dynamical property is considered while the current's dynamic property is neglected when establishing the system's model since the electrical

response speed is much higher than the mechanical response speed. Considering all the above factors [25] and [26], the mathematic model of the torque-controlled motor servo system can be described as:

$$J_{\text{equ}}\ddot{y} = k_u \cdot u - B_{equ} \cdot \dot{y} - d_n - f(t), \tag{1}$$

where J_{equ} is the equivalent inertia of the motor and load, y is the position of the load, k_u is the voltage-torque coefficient, u is the control input, B_{equ} is the equivalent viscous friction coefficient, d_n is the constant disturbance, $f(t)$ is the time-varying disturbance.

Before the controller is designed, some hypotheses should be made as follows:

1) All the parameters of system are invariant variables or slowly time-varying variables. That is $\dot{J}_{equ} = \dot{k}_u = \dot{B}_{equ} = \dot{d}_n = 0.$
2) All the parameters are bounded, and the upper/lower bounds for all these parameters are known.

Assuming that the input saturation exists in the actuator. u is the output of the actuator, the maximum value of u is u_{max}, v is the control input of the actuator, δ is the input saturation. $u = \delta + v$, $u = sat(v)$, the function $sat(v)$ can be expressed as:

$$sat(v) = \begin{cases} u_{\max}, & v > u_{\max} \\ v, & |v| \le u_{\max} \\ -u_{\max}, & v < u_{\max} \end{cases}, \tag{2}$$

It is necessary to build a state space equation of the system for designing a controller for the system. Thus, a number of parameters are defined: $\theta_1 = J_{equ}/k_u$, $\theta_2 = B_{equ}/k_u$, $\theta_3 = d_n/k_u$. Then, the mathematical model, Eq. (1), can be rewritten as:

$$\theta_1\ddot{y} = v - \theta_2\dot{y} - \theta_3 - \tau(t) + \delta, \tag{3}$$

where $\tau(t) = f(t)/k_u$ indicates the time-varying disturbance and other systematic un-modelled nonlinearities.

Denote the state variables as:

$$\begin{cases} x_1 = y \\ x_2 = \dot{y} \end{cases}. \tag{4}$$

Then the state space equation of the system could be obtained as follows:

$$\begin{cases} \dot{x}_1 = x_2 \\ \theta_1\dot{x}_2 = v - \theta_2\dot{y} - \theta_3 - \tau(t) + \delta \end{cases}. \tag{5}$$

2 DESIGN OF A CONTROLLER WITH NEURAL NETWORK BASED OBSEVER

2.1 Neural Network Based Observer Design

In the mechanical-electrical servo system, the state of the system is nonlinear, time-varying, and uncertain; in other words, it is very difficult to know the precise value of overflow by using the sensor and other measuring tools. Designing an observer to observe the overflow of input saturation is necessary. A NN can approximate any smooth nonlinear function to within arbitrary accuracy when given a sufficient number of hidden layer neurons and input information. Thus, a single hidden-layer network is defined to approximate the unknown parameter δ.

The mathematical expression of the single-layer NN is as follows:

$$\delta = W^{*T}h(x) + \varepsilon_{approx}, \tag{6}$$

$$h_j = \exp\left(-\frac{\| x - c_j \|^2}{2b_j^2}\right), \tag{7}$$

where $x = [x_1\ x_2\ \ldots\ x_n]^T$ is the input of network, j is the j^{th} node of the hidden layer, $h = [h_j]^T$ is the output of network's Gauss radial function, $c_j = [c_{j1}\ c_{j2}\ \ldots\ c_{jn}]$ is centre vector value of the j^{th} node, $b = [b_1\ b_2\ \ldots\ b_m]^T$ is the width of the Gauss basis function, W^{*T} is ideal weights of NN, ε_{approx} is approximation error of the NN and $\varepsilon_{approx} \le \varepsilon_N$.

The input of the neural network is chosen as $x = [x_1, x_2]^T$, and then the real output of the network is:

$$\hat{\delta} = \hat{W}^T h(x), \tag{8}$$

where $\hat{W}$ represent the estimated value of W^*. Design the adaptive law of weights as follows:

$$\dot{\hat{W}} = \text{Proj}_{\hat{W}}\left\{\Gamma_2 h(x \cdot z_2)\right\}, \tag{9}$$

where

$$\text{Proj}_{\hat{W}}(\cdot i) = \begin{cases} 0, & \hat{W}_i = W_{i\max} \quad \text{and} \quad \cdot i > 0 \\ 0, & \hat{W}_i = W_{i\min} \quad \text{and} \quad \cdot i < 0 \\ \cdot i, & \text{otherwise} \end{cases}, \tag{10}$$

and Γ_2 is the adaptive law matrix of weights.

Define $\tilde{W} = \hat{W} - W^*$, thus

$$\begin{aligned} \delta - \hat{\delta} &= W^{*T}h(x) + \varepsilon_{approx} - W^T h(x) \\ &= (W^{*T} - W^T)h(x) + \varepsilon_{approx} \\ &= -W^T h(x) + \varepsilon_{approx}. \end{aligned} \tag{11}$$

Remark 1: Input saturation is an inevitable phenomenon in mechanical-electrical servo systems, so the impact of the input saturation should be restrained when designing the controller. How to compensate the overflow of input saturation is the key to solving the nonlinear problem. A single hidden-layer network-based observer can estimate the overflow δ and the estimation error of the single hidden-layer network can be close to 0 as long as the nodes in the hidden layer are enough in theory. That is to say, the single hidden-layer network can approximate δ within arbitrary accuracy. It is obvious that the value of δ could be replaced by estimation value δ when designing the controller later, and the control performance could be observably improved.

2.2 Design of a Controller

The system that is driven by a torque-controlled motor is a typical motor servo system, and the control system is a second-order system. The design process of a specific controller is as follows.

Step 1. In this step, x_2 is deemed a dummy control input. And x_2 is regarded as the dummy control input; afterwards, a control function x_{2eq} ought to be designed for x_2. The result in the tracking property is guaranteed. Denoting x_{1d} as the ideal position and $z_1=x_2-x_{1d}$ indicate the position tracking error. After that, the dynamic equation of error is as follows:

$$\dot{z}_1 = \dot{x}_1 - \dot{x}_{1d} = x_2 - \dot{x}_{1d}. \tag{12}$$

Let $z_2=x_2-x_{2eq}$ indicates the error between the virtual input and the real input, thus the Eq. (12) can be rearranged as follows:

$$\dot{z}_1 = z_2 + x_{2eq} - \dot{x}_{1d}. \tag{13}$$

Based on Eq. (13), the resulting virtual control law x_{2eq} could be designed as follows:

$$x_{2eq} = \dot{x}_{1d} - k_1 z_1, \tag{14}$$

where $k_1>0$. Substituting Eq. (14) into Eq. (13), we could obtain:

$$\dot{z}_1 = z_2 - k_1 z_1. \tag{15}$$

From Eq. (15), it is indicated that we want to turn z_2 converge into zero to turn z_1 converge into zero.

Step 2. The dummy control law x_{2eq} has been designed in Step 1. In this step, we need to design the real control law for v. The time derivative of z_2 can be given by:

$$\begin{aligned}\theta_1 \dot{z}_2 &= \theta_1 \dot{x}_2 - \theta_1 \dot{x}_{2eq} \\ &= v - \theta_2 x_2 - \theta_3 - \tau(t) + \delta - \theta_1 \dot{x}_{2eq} \\ &= v - \theta_1 \dot{x}_{2eq} - \theta_2 x_2 - \theta_3 - \tau(t) + \delta. \end{aligned} \tag{16}$$

To make z_2 converge to 0, the following control law v is proposed:

$$v = v_a + v_s, \tag{17}$$

$$v_a = \hat{\theta}_1 \dot{x}_{2eq} + \hat{\theta}_2 x_2 + \hat{\theta}_3 - \hat{\delta}, \tag{18}$$

$$v_s = v_{s1} + v_{s2}, \tag{19}$$

$$v_{s1} = -k_2 z_2, \quad v_{s2} = -\frac{h_s^2}{4\varepsilon_s} z_2, \tag{20}$$

where v_a is the feed-forward compensation term of the system model, v_{s1} is a linear robust feedback term to stabilize the system nominal model and $k_2>0$, v_{s2} is a nonlinear robust feedback term which is used to compensate for the time-varying disturbance and the model error.

Substituting Eqs. (18) and (11) into Eq. (16), later the Eq. (16) could be transformed to:

$$\begin{aligned}\theta_1 \dot{z}_2 &= \tilde{\theta}_1 \dot{x}_{2eq} + \tilde{\theta}_2 x_2 + \tilde{\theta}_3 - k_2 z_2 + \delta - \hat{\delta} + v_{s2} - \tau(t) \\ &= \tilde{\theta}_1 \dot{x}_{2eq} + \tilde{\theta}_2 x_2 + \tilde{\theta}_3 - k_2 z_2 \\ &\quad - \tilde{W}^T h(x) + \varepsilon + v_{s2} - \tau(t) \\ &= -\tilde{\theta}^T \begin{bmatrix} -\dot{x}_{2eq} & -x_2 & -1 \end{bmatrix} + v_{s2} \\ &\quad - \tilde{W}^T h(x) + \varepsilon - k_2 z_2 - \tau(t) \\ &= -\tilde{\theta}^T \varphi + v_{s2} - \tilde{W}^T h(x) + \varepsilon - k_2 z_2 - \tau(t), \end{aligned} \tag{21}$$

where θ_1, θ_2, θ_3 is unknown, and the value would be changed in the working process of the system, in order to design the controller simply, we should adopt the estimated value to replace the uncharted parameter when designing the controller, (for example $\hat{\theta}_1$, $\hat{\theta}_2$, $\hat{\theta}_3$). Thus, a parameter matrix $\theta = [\theta_1\ \theta_2\ \theta_3]$ and an estimated parameter matrix $\hat{\theta} = \begin{bmatrix} \hat{\theta}_1 & \hat{\theta}_2 & \hat{\theta}_3 \end{bmatrix}$ should be defined. Based on Assumption 2.1, we could obtain:

$$\theta \in \Omega_\theta = \{\theta : \theta_{\min} < \theta < \theta_{\max}\}, \tag{22}$$

$$|\tau(t)| < \delta_d, \tag{23}$$

where $\theta_{\min} = \begin{bmatrix} \theta_{1\min} & \theta_{2\min} & \theta_{3\min} \end{bmatrix}^T$, and $\theta_{\max} = \begin{bmatrix} \theta_{1\max} & \theta_{2\max} & \theta_{3\max} \end{bmatrix}^T$ is the upper/lower bounds of the system parameters, and the values of the upper and lower bounds are known, and δ_d is a constant.

Step 3. In this step, an estimator should be designed to estimate the unknown system parameters. In order to make both the estimated parameters and the model uncertainty bounded, design a discontinuous projection gradient type parameter adaptation law as follows:

$$\dot{\hat{\theta}} = \mathrm{Proj}_{\hat{\theta}}\left\{\Gamma_1 \varphi z_2\right\}, \tag{24}$$

where

$$\mathrm{Proj}_{\hat{\theta}}(\cdot i) = \begin{cases} 0, & \hat{\theta}_i = \theta_{i\max} \quad \text{and} \cdot i > 0 \\ 0, & \hat{\theta}_i = \theta_{i\min} \quad \text{and} \cdot i < 0 \\ \cdot i, & \text{otherwise} \end{cases}, \tag{25}$$

$$\varphi = \left[-\dot{x}_{2eq} \quad -x_2 \quad -1\right]^T. \tag{26}$$

φ is the parameter adaptive regression, Γ_1 is the adaptation law matrix, in addition, there are the following properties:

$$\hat{\theta} \in L_\infty, \quad \tilde{\theta}\left[\mathrm{Proj}_{\hat{\theta}}(\Gamma\varphi z_2) - \Gamma\varphi z_2\right] \le 0, \tag{27}$$

where $\tilde{\theta}=\theta-\hat{\theta}$ represents the error of parametric estimation.

Step 4. In this step, in order to overcome the parameters approximation error and approximation error of model uncertainty, a nonlinear robust feedback item u_{s2} should be designed to stabilize the system and improve the tracking performance.

Define $v_{s2} = (-h_s^2 z_2)/4\varepsilon_s$, where this represents all the errors' upper bound, and it means $|\tilde{\theta}^T\phi| + |\tilde{W}^T h(x)| + |\varepsilon| + \delta_d \le h_s$, ε_s is a positive real number which has the following characters:

$$\begin{cases} i: z_2\left[v_{s2} - \tilde{\theta}^T\varphi - \tilde{W}^T h(x) - \varepsilon - \tau(t)\right] \le \varepsilon_S \\ ii: z_2 \cdot v_{s2} \le 0 \end{cases}. \tag{28}$$

2.3 Stability Analysis

The specific diagram of control tactics is shown in Fig. 3. The strategy adopts an NN observer to estimate the state that cannot be measured, and the weight adaptive velocity is used to estimate the weights online. In addition, the parameter regression is used to estimate the unknown parameters; all the estimated parameters are required in the feed-forward compensator. A linear robust term v_{s1} is designed to overcome the constant disturbance of the system, and a nonlinear robust term v_{s2} is designed to compensate the time-varying disturbance and modelling errors.

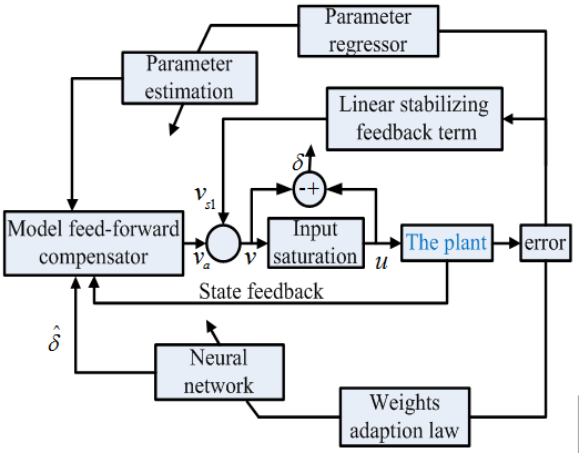

Fig. 3. *The neural network observer based robust adaptive control tactics graph*

Based on the controller designed earlier, we could obtain the following theorem:

Theorem 2.1. With the NN-based observer, Eqs. (8) and (9), the parameter adaption law in Eq. (24), the adaptive robust full state feedback control law in Eq. (17), we can obtain a specified transient and everlasting performance in the sense that limiting the tracking error to a small extent by a known function exponentially converges to the $(1/k_1)\sqrt{(2\varepsilon_s)/(\lambda\theta_{1\min})}$ with a converging law no fewer than λ.

Proof: See Appendix 7.1.

Remark 2: The consequence of theorem 2.1 denotes that the contrivable controller consists of a robust adaptive controller and NN-based observer, which has an exponential convergence transitory property with the exponentially converging rate λ, and the ultima tracking error was inhibited by adjusting the system's parameters online. The parameter adaption law could approximate the unknown system parameters, and the weight adaptive law could estimate the value of the weights. The constant disturbance of the system was compensated by the feed-forward compensation item which used the estimated parameters. Moreover, the input saturation was compensated by the output value of the NN based observer. Furthermore, the nonlinear robust feedback item was proposed to reduce the effect of parameter estimation error and weights estimation error, which could effectively improve the stability of the closed-loop system.

Theorem 2.2: With NN observer, Eqs. (8) and (9), parameter adaptive law, Eq. (24), adaptive robust

full state feedback control law, Eq. (17), the system could achieve asymptotic export tracking merely in the presence of parametric uncertainty.

Proof: See Appendix 7.2.

Remark 3: The consequence of theorem 2.2 denote that the adaptive robust controller based on an NN observer could obtain improved tracking performance, and the system could achieve asymptotic export tracking in the absence of the estimated error of NN.

3 EXPERIMENTAL RESULTS

The experimental platform of torque-controlled motor servo system is shown in Fig. 4. This experimental platform consists of a torque-controlled servomotor, a speed reducer, a slewing mechanism, a photoelectric encoder, sensors, a power supply, and an IPC. The photoelectric encoder could sample the position signals of the two servo-motor. The voltage signal is transmitted to the driver by using a (digital/analogue) D/A board card.

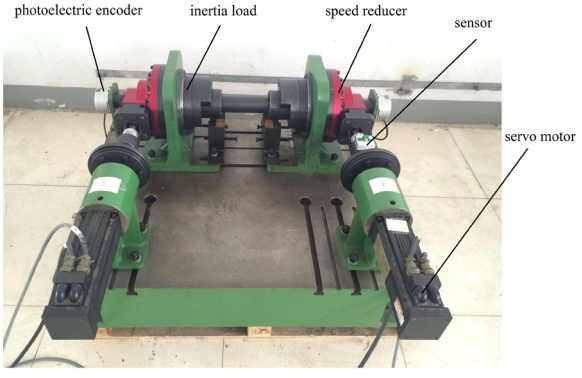

Fig. 4. *The experimental platform of torque-controlled motor servo system*

The parameters of the experimental platform are given as follows:

Table 1. *The parameters used in experiment*

Equivalent inertia J_{equ}	0.00138 kg·m²
Equivalent viscous friction coefficient B_{equ}	0.4 N·m·s/rad
Voltage-torque coefficient k_u	2.36 N·m/V

Three controllers are compared for a sinusoidal-like motion trajectory, and two cases are compared for this normal motion trajectory. Case 1 is "constant disturbance case": Setting the constant disturbance as $d_n=0.5$. Then, after a simple calculation, we can obtain: $\theta_1=0.01$, $\theta_2=0.294$, $\theta_3=0.36$. Case 2 is "time-varying disturbance case": The time-varying disturbance in the system was set as $f(t)=0.015\cdot x_1\cdot x_2$, and x_1, x_2 are state variables selected. The three controllers are as follows:

1) The proportional–integral–derivative controller (PID): in industrial control applications, the PID controller was used widely, its proportional integral differential control of position and speed loop has low dependence on the system model, and could obtain a high accuracy. In this experiment, the PID controller of position loop is used, and its three parameters could be adjusted by observing the position error. Denote the parameters of the proportional, integral and differential as $k_p=25$, $k_i=0.8$, $k_d=0$.
2) The adaptive robust controller (ARC): in the closed-loop system was realized by the control law, Eq. (17), and the parameter adaptive law, Eq. (24), which designed in the above, and the effect caused by input saturation was not considered in this case. In this experiment, the feedback gains are chosen as $k_1=35$, $k_2=002$. The upper and the lower bounds of parameters are $\theta_{\max}=[0.05, 0.5, 0.5]$, $\theta_{\min}=[0.005, 0.01, 0.01]$.
3) The adaptive robust controller with neural network based observer (ARCNN): The control gains are chosen as $k_1=20$, $k_2=0.01$, and $[v\ z_2]$ is the input of the NN, the parameters of the Gauss basis function was designed via the actual input extent of the network; therefore, choose $c_j=8\times[-1, -0.5, 0, 0.5, 1]$, $b_j=5$, in this case, and define the initial value of network weights as zero.

In order to verify the feasibility of the adaptive robust controller based on the NN observer, set the limitation of input saturation in actuator: $u_{\max}=0.45$, $u_{\min}=-0.45$. The desired output signal: $y_d=x_1(t)=2\times\sin(3.14t)[1-\exp(-0.01t)]$ [°]. To ensure that the performance of the designed controller is fully demonstrated, the sample time at least is set to 15 s.

Table 2. *The accuracy of the three controllers in Case 1: "constant disturbance case"*

Controller	Time [s]	Accuracy [°]
ARC	$t>5$	0.062
PID	$t>5$	0.045
ARCNN	$t>10$	0.0028

The position curve in the ideal state and the homologous tracking property of the three controllers in Case 1 are shown in Fig. 5, which shows that the PID controller and ARCNN controller could obtain the better position tracking performance than

ARC controller in terms of both transient and final tracking errors, the result of experimental indicate that the impact caused by input saturation could not be ignored in the control system. By comparing the control performance of the three controllers, the ARCNN controller has the best tracking property, and its maximum steady tracking error is about 0.0028°. Fig. 6 shows the voltage signals v and u; v is the voltage signal before the saturation constraint occurred, and u is the voltage signal after the saturation constraint occurred; from the picture we can see the error between v and u cannot be ignored, thus the effect of input saturation should be considered. Fig. 7 shows the overflow of input saturation and corresponding estimation. It can be seen that the NN observer could estimate the overflow immediately and thus the input saturation could be compensated effectively. In addition, ARCNN adopts the parameter adaptive law and the weights adaptive law to estimate uncertain parameters and weights, which are used in the feed-forward compensation item. Therefore, a high performance was realized, which also proved the validity of the adaptive control law.

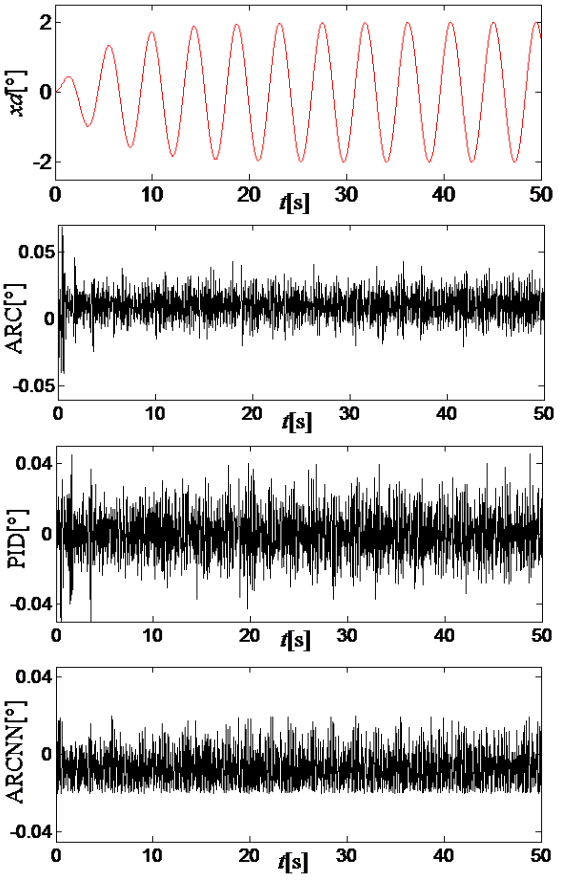

Fig. 5. *Tracking error of three controllers in Case 1*

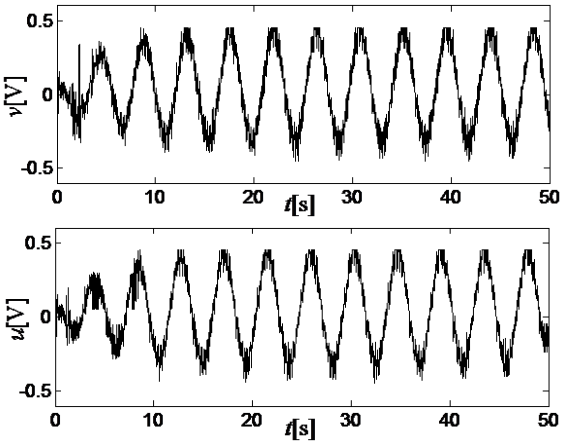

Fig. 6. *The voltage signal v, u in Case 1*

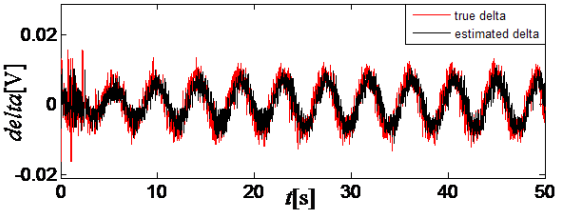

Fig. 7. *The true value and the estimated value of input saturation in Case 1*

Table 3. *The accuracy of the three controllers in Case 2: "time-varying disturbance case"*

Controller	Time [s]	Accuracy [°]
ARC	$t > 5$	0.056
PID	$t > 5$	0.045
ARCNN	$t > 5$	0.035

The position curve in the ideal state and the homologous tracking property of the three controllers in Case 2 is revealed in Fig. 8. As seen from the figure, the input saturation is compensated by NN or PID has the better tracking performance than uncompensated, which confirms that the accuracy of the estimation is very important. Fig. 9 indicate that the voltage before and after saturation constrain, as seen when $t \leq 1$ s, the output voltage exceeds the limitation of actuator input, the voltage signal is limited to the working voltage range of actuator owing to saturation constraint, which improved the tracking accuracy of the system, and reduces the shock range of the voltage signal at the same time. Fig. 10 shows the curve of δ and $\hat{\delta}$, from the figure, the NN could observe and estimate the overflow immediately when the input saturation rises, then the estimated value is used in the feed-forward compensation. The ARCNN controller has the best tracking performance and the position tracking error is

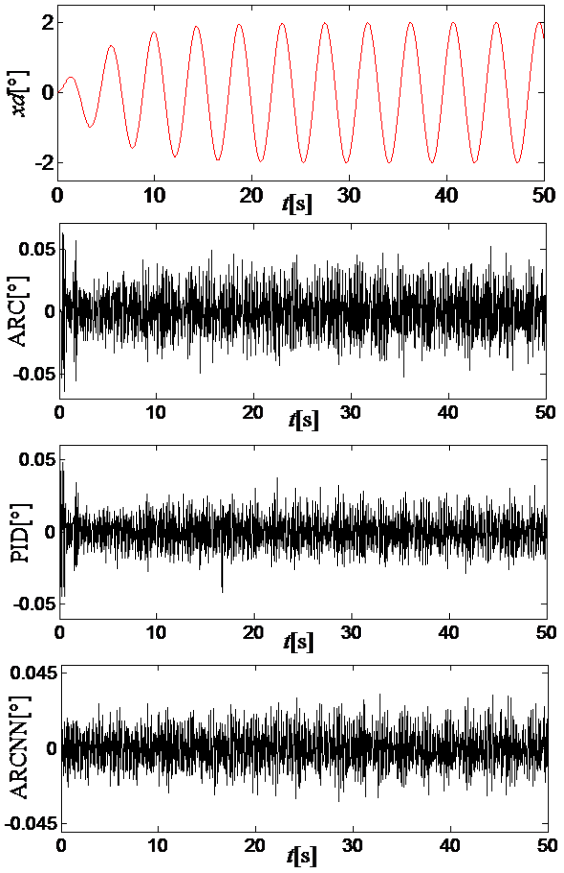

Fig. 8. *Tracking error of three controllers in Case 2*

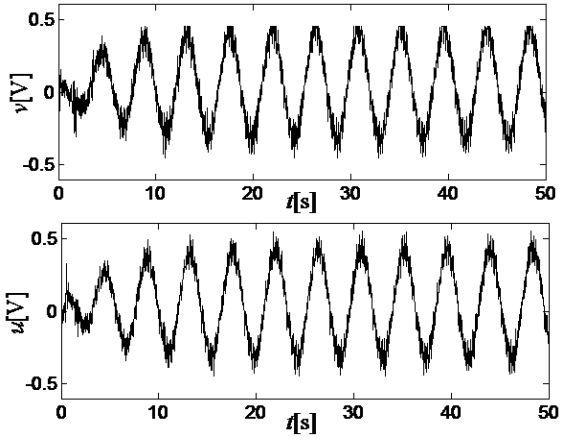

Fig. 9. *The voltage signal v, u in Case 2*

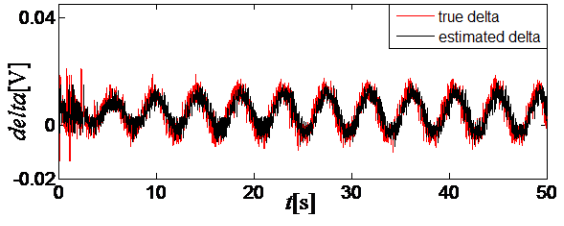

Fig. 10. *The true value and the estimated value of input saturation*

less than 0.0035°; this also proved the effectiveness of parameter adaptive estimation and NN weight estimation in the presence of constant disturbance and time-varying interference (adaptive parameter estimation curve is shown in Fig. 11).

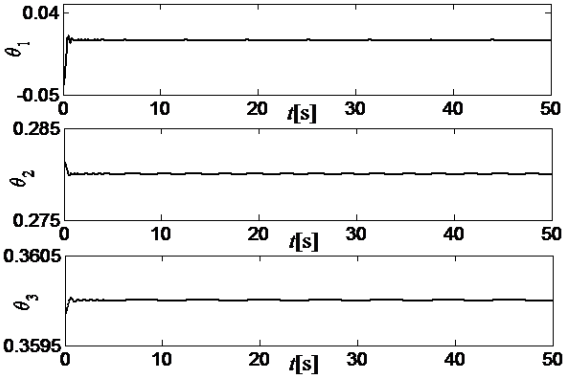

Fig. 11. *Adaptive parameter estimation curve of ARCNN in Case 2*

4 CONCLUSIONS

In this paper, considering the universal approximation ability of NN, a single hidden-layer NN based observer is designed to estimate the input saturation of the system, which is later compensated in the controller. An adaptive law is introduced to estimate the unknown parameters, and a nonlinear robust term is designed to overcome the time-varying disturbances. The NN weight adaption law has been deduced by using the Lyapunov method. The proposed controller pledges the asymptotic stability of the tracking performance under the condition that the NN estimation error is zero. The effectiveness of the proposed control strategy has been proved by comparing the experimental results. In the future, the input saturation and external disturbance should be estimated by designing a double- observer, which is helpful in improving the control precision of the motor servo system.

5 ACKNOWLEDGMENT

This work was supported by the National Natural Science Foundation of China under Grant 51505224, and the Natural Science Foundation of Jiangsu Province in China under Grant BK2015776.

6 REFERENCES

[1] Yao, J., Jiao, Z., Ma, D.. (2014). Adaptive robust control of dc motors with extended state observer. *IEEE Transactions*

on Industrial Electronics, vol. 61, no. 7, p. 3630-3637, **DOI:10.1109/TIE.2013.2281165**.

[2] Chen, M., Ge, S.S., Ren, B. (2011). Adaptive tracking control of uncertain MIMO nonlinear systems with input constraints. *Automatica*, vol. 47, no. 3, p. 452-465, **DOI:10.1016/j.automatica.2011.01.025**.

[3] Mesloub, M., Benchouia, M.T., Golea, A. (2017). A comparative experimental study of direct torque control based on adaptive fuzzy logic controller and particle swarm optimization algorithms of a permanent magnet synchronous motor. *The International Journal of Advanced Manufacturing Technology*, vol. 90, no. 1-4, p. 59-72, **DOI:10.1007/s00170-016-9092-4**.

[4] Zong, Q., Wang, F., Tian, B. (2014). Robust adaptive dynamic surface control design for a flexible air-breathing hypersonic vehicle with input constraints and uncertainty. *Nonlinear Dynamics*, vol. 78, no. 1, p. 289-315, **DOI:10.1007/s11071-014-1440-z**.

[5] Esfandiari, K., Abdollahi, F., Talebi, H. (2015). Adaptive control of uncertain nonaffine nonlinear systems with input saturation using neural networks. *IEEE transactions on Neural Networks and Learning Systems*, vol. 26, no. 10, p. 2311-2322, **DOI:10.1109/TNNLS.2014.2378991**.

[6] Li, Y., Tong, S., Li, T. (2013). Direct adaptive fuzzy back-stepping control of uncertain nonlinear systems in the presence of input saturation. *Neural Computing and Applications*, vol. 23, no. 5, p. 1207-1216, **DOI:10.1007/s00521-012-0993-3**.

[7] Gao, S., Dong, H., Ning, B., Chen, L. (2015). Neural adaptive control for uncertain nonlinear system with input saturation: State transformation based output feedback. *Neurocomputing*, vol. 159, p. 117-125, **DOI:10.1016/j.neucom.2015.02.012**.

[8] Chen, M., Ge, S. (2013). Direct adaptive neural control for a class of uncertain nonaffine nonlinear systems based on disturbance observer. *IEEE Transactions on Cybernetics*, vol. 43, no. 4, p. 1213-1225, **DOI:10.1109/TSMCB.2012.2226577**.

[9] Ammar, A., Bourek, A., Benakcha, A. (2017). Nonlinear SVM-DTC for induction motor drive using input-output feedback linearization and high order sliding mode control. *ISA Transactions*, vol. 67, p. 428-422, **DOI:10.1016/j.isatra.2017.01.010**.

[10] Yao, J., Jiao, Z., Ma, D. (2014). RISE-based precision motion control of dc motors with continuous friction compensation. *IEEE Transactions on Industrial Electronics*, vol. 61, no. 12, p. 7067-7075, **DOI:10.1109/TIE.2014.2321344**.

[11] Yao, J., Yang, G., Jiao, J., Ma, D. (2013). Adaptive robust motion control of direct-drive DC motors with continuous friction compensation. *Abstract & Applied Analysis*, vol. 2013, p. 1-14, **DOI:10.1155/2013/837548**.

[12] Wang, H., Liu, X., Liu, K. (2015). Adaptive neural data-based compensation control of non-linear systems with dynamic uncertainties and input saturation. *IET Control Theory Application*, vol. 9, no. 7, p. 1058-1065, **DOI:10.1049/iet-cta.2014.0709**.

[13] Sui, S., Tong, S. Li, Y. (2014). Predefined performance fuzzy adaptive tracking control for nonlinear stochastic systems with input saturation. *International Conference on Mechatronics and Control*, **DOI:10.1109/ICMC.2014.7231572**.

[14] Sun, W., Gao, H., Kaynak, O. (2011). Finite frequency H∞ control for vehicle active suspension systems. *IEEE Transactions on Control Systems Technology*, vol. 19, no. 2, p. 416-422, **DOI:10.1109/TCST.2010.2042296**.

[15] Wang, H, Chen, B. Liu, X., Liu, K., Lin, C. (2014). Adaptive neural tracking control for stochastic nonlinear strict-feedback systems with unknown input saturation. *Information Sciences*, vol. 269, p. 300-315, **DOI:10.1016/j.ins.2013.09.043**.

[16] Zhou, Q., Shi, P., Tian, Y., Wang, M. (2015). Approximation-based adaptive tracking control for MIMO nonlinear systems with input saturation. *IEEE Transactions on Cybernetics*, vol. 45, no. 10, p. 2119-2128, **DOI:10.1109/TCYB.2014.2365778**.

[17] Wu, J., Liu, K., Han, D. (2013). Adaptive sliding mode control for six-DOF relative motion of spacecraft with input constraint. *Acta Astronautica*, vol. 87, p. 64-76, **DOI:10.1016/j.actaastro.2013.01.015**.

[18] Zong, Q., Wang, F., Su, R. (2015). Robust adaptive back-stepping tracking control for a flexible air-breathing hypersonic vehicle subject to input constraint. *Institution of Mechanical Engineers*, vol. 229, no. 1, p. 10-25, **DOI:10.1177/0954410014525128**.

[19] Yao, J., Jiao, Z., Ma, D. (2014). Extended-state-observer-based output feedback nonlinear robust control of hydraulic systems with back-stepping. *IEEE Transactions on Industrial Electronics*, vol. 61, no. 11, p. 6285-6293, **DOI:10.1109/TIE.2014.2304912**.

[20] Uran, S., Šafarič, R. (2012). Neural-Network estimation of the variable plant for adaptive sliding-mode controller. *Strojniški vestnik - Journal of Mechanical Engineering*, vol. 58, no. 2, p. 93-101, **DOI:10.5545/sv-jme.2011.098**.

[21] Zilkova, J., Timko, J., Girovsky, P. (2012). Modelling and control of tinning line entry section using Neural Networks. *International Journal of Simulation Modelling*, vol. 11, no. 2, p. 97-109, **DOI:10.2507/IJSIMM11(2)4.210**.

[22] Hu, J., Liu, L., Wang, Y.G., Xie, Z. (2016). Precision motion control of a small launching platform with disturbance compensation using neural networks. *International Journal of Adaptive Control and Signal Processing*, vol. 31, no. 7, p. 971-984, **DOI:10.1002/acs.2743**.

[23] Alonge, F., Cirrincione, M., D'Ippolito, F., Pucci, M., Sferlazza, A. (2016). Adaptive feedback linearizing control of linear induction motor considering the end-effects. *Control Engineering Practice*, vol. 55, p.116-126, **DOI:10.5545/sv-jme.2011.098**.

[24] Hu, J., Qiu, Y., Liu, L. (2016). High-order sliding-mode observer based output feedback adaptive robust control of a launching platform with backstepping. *International Journal of Control*, vol. 89, no. 10, p. 2029-2039, **DOI:10.1080/00207179.2016.1147604**.

[25] Mrčela, T., Žeželj, D., Panić, N. (2009). Linear loading measurement line for static torque and its performance. *Tehnički vjesnik – Technical Gazette*, vol. 22, no. 5, p. 1093-1098.

[26] Ahmad, F., Hudha, K., Mazlan, S.A., Jamaluddin, H., Zamzuri, H., Kadir, Z.A., Aparow, V.R. (2017). Modelling and control of a fixed calliper-based electronic wedge brake. *Strojniški vestnik - Journal of Mechanical Engineering*, vol. 63, no. 3, p. 181-190, **DOI:10.5545/sv-jme.2016.3508**.

7 APPENDICES

Proof of Theorem 2.1: Without considering the neural network estimation error, the Lyapunov function is established as follows:

$$v_1(t) = \frac{1}{2}\theta_1 z_2^2, \tag{29}$$

$$\begin{aligned} v_1 &= \theta_1 \dot{z}_2 z_2 \\ &= -k_2 z_2^2 + (v_{s2} - \tilde{\theta}^T \varphi - \tilde{W}^T h(x) - \varepsilon_{approx}) z_2 \\ &\le -k_2 z_2^2 + \varepsilon_s = -k_2 (\frac{2V_1}{\theta_1}) + \varepsilon_s \le -\lambda V_1 + \varepsilon_s, \end{aligned} \tag{30}$$

where $\lambda = 2k_2 / \theta_{1\min}$, we can obtain:

$$V_1(t) \le V_1(0)\exp(-\lambda t) + \frac{\varepsilon_s}{\lambda}[1 - \exp(-\lambda t)]. \tag{31}$$

With the passage of time, the position tracking error and angular velocity tracking error will be limited to a certain extent.

$$|z_2| = \sqrt{\frac{2\varepsilon_s}{\lambda\theta_1}} \le \sqrt{\frac{2\varepsilon_s}{\lambda\theta_{1\min}}}, \tag{32}$$

$$|z_1| \le \frac{1}{k_1}\sqrt{\frac{2\varepsilon_s}{\lambda\theta_{1\min}}}. \tag{33}$$

Proof of theorem 2.2: when $\varepsilon_{approx}=0$, consider the following Lyapunov function candidate:

$$V_2 = \frac{1}{2}\theta_1 Z_2^2 + \frac{1}{2}\Gamma_1^{-1}\tilde{\theta}^T\tilde{\theta} + \frac{1}{2}\Gamma_2^{-1}\tilde{W}^T\tilde{W}, \tag{34}$$

$$\dot{V}_2 = \theta_1 \dot{z}_2 z_2 + \Gamma_1^{-1}\tilde{\theta}^T\dot{\tilde{\theta}} + \Gamma_2^{-1}\tilde{W}^T\dot{\tilde{W}}. \tag{35}$$

Since θ and W are invariant or slowly varying variables, we could have $\dot{\hat{\theta}} = \dot{\tilde{\theta}}, \dot{\hat{W}} = \dot{\tilde{W}}$. Then we could obtain:

$$\begin{aligned} \dot{V}_2 &= \theta_1 \dot{z}_2 z_2 + \Gamma_1^{-1}\tilde{\theta}^T\dot{\hat{\theta}} + \Gamma_2^{-1}\tilde{W}^T\dot{\hat{W}} \\ &= -k_2 z_2^2 + v_{s2} z_2 + \Gamma_1^{-1}\tilde{\theta}^T \mathrm{Proj}_{\hat{\theta}}\left\{\Gamma_1 \varphi z_2\right\} - \tilde{\theta}^T \varphi z_2 \\ &+ \Gamma_2^{-1}\tilde{W}^T \mathrm{Proj}_{\hat{W}}\left\{\Gamma_2 h(x) z_2\right\} - \tilde{W}^T\left\{h(x)\right\} z_2 \\ &\le -k_2 z_2^2 + v_{s2} z_2 \le -k_2 z_2^2. \end{aligned} \tag{36}$$

Strojniški vestnik - Journal of Mechanical Engineering 63(2017)9, 529-536

DOI:10.5545/sv-jme.2017.4526 Original Scientific Paper
Received for review: 2017-04-22
Received revised form: 2017-06-16
Accepted for publication: 2017-07-14

Wall Roughness Influence on the Efficiency Characteristics of Centrifugal Pump

Andrej Lipej[1] – Simon Muhič[1,*] – Duško Mitruševski[2]
[1] Faculty of Technologies and Systems, Slovenia
[2] SM Pumps, Ljubljana, Slovenia

Many different machines are developed in industry and in terms of energy conversion, their efficiency is one of the most important parameters. A lot of theoretical, experimental and numerical analyses are done in the development process in order to obtain required characteristics. Computational fluid dynamics (CFD) analyses are a very important part of the development process. To obtain accurate results it is important to pay attention to geometry definition, usage appropriate numerical model, quality of the computational grid, realistic boundary conditions and all of the other parameters regarding fluid and solid material properties. A very important issue is usually the correct selection of the turbulence model. In most CFD analyses, only smooth surface is taken into account without considering any wall roughness. Besides the usage of different physical and mathematical models and all required parameters, the wetted surface roughness can also be one of the important origins of the numerical results inaccuracy. In the paper, the analysis of the influence of different parameters such as the sand-grain equivalent parameter is presented. The influence of y^+ on the accuracy of the flow analysis with different absolute roughness of the surfaces is also analyzed. For basic relations, the flow in simple geometries like flow over flat plate and flow in circular pipe has been analyzed. The conclusions of the preliminary research work are used in the case of efficiency prediction of centrifugal pump with rough walls. The final numerical results are compared with the experimental ones and show better agreement in comparison with the flow over smooth walls.
Keywords: pump, CFD, wall roughness, turbulence

Highlights
- *Water pumps are very important hydraulic machines with significant electricity consumption, because of the huge number of the operating machines.*
- *The accuracy of numerical prediction of energetic characteristics is very important for the development process of centrifugal pumps.*
- *One of the important parameters in CFD analysis is wall roughness, which is the main reason why in the paper an investigation of the influence of roughness on the CFD results is performed.*
- *Using correct computational grid parameters is very important for the accuracy of numerical analyses.*

0 INTRODUCTION

Fluid flow over rough walls is theoretically explained quite well. There are many research works in this field. Well known relations also exist in non-dimensional form of the Darcy-Weisbach friction factor λ, Reynolds number Re, and relative roughness for fully developed flow in a circular pipe, presented in Moody diagram.

For solving Navier-Stokes equations in 3D arbitrary complex geometries, it is not possible to get analytical solution, but only numerical. The similar situation is also prediction of losses, caused by different surface roughness of the walls.

In the CFD analyses, the surface roughness can be analyzed in two ways. First, the complete surface shape can be taken into account, but such approach needs very fine computational grids and in the majority of industrial application it is not an appropriate method.

Another method is the usage of special parameters, which define the surface roughness. In some commercial software, the sand-grain equivalent parameter is used to predict the surface roughness. It is known from literature that sand-grain equivalent parameter does not depend only on the roughness amplitudes, but also on the shape and frequency of the roughness [1].

An important issue in the CFD analysis is the near wall treatment with different turbulence models and using the exact value for y^+ parameter is meaningful. This parameter is very important in the analysis of smooth surfaces, however, it is even more important when the surface is not hydraulically smooth.

The arithmetic average of the roughness profile R_a is defined as (Fig. 1):

$$R_a = \frac{1}{n}\sum_{i=1}^{n}|y_i|. \quad (1)$$

Literature review about the usage of CFD analysis of rough walls shows that the number of scientific papers about this topic is quite moderate. It is possible to find some papers about the connection of turbulence models and wall roughness [2] and [3]. Some authors

*Corr. Author's Address: Faculty of Technologies and Systems, Na Loko 2, Novo mesto, Slovenia, simon.muhic@fts-nm.si

performed some research work on the basic influence of the wall roughness on the turbulent boundary layer [4] to [6]. The paper [7] presents analysis of the losses in centrifugal pump with smooth and rough walls. In the paper, some figures about the difference between experimental and numerical obtained efficiency are presented. It is also possible to find research work about the degradation of an axial-turbine stage [8] as a consequence of wall roughness using the CFD analysis. Some papers dealing with wall roughness are devoted to different topics like mine ventilation networks [9] or just numerical analysis around blades [10] as well as numerical analysis of the flow in the pipes with rough walls [11].

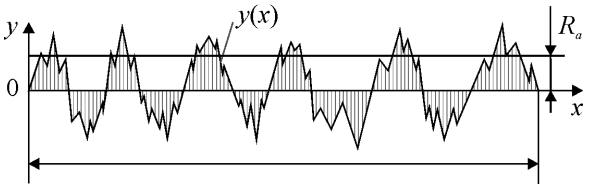

Fig. 1. *Roughness profile*

1 METHODS

Surface roughness has a significant influence on the engineering problems and leads to an increase in turbulence production near the rough walls. This also has an influence on increasing wall shear stress. Accurate prediction of near wall flows depends on the proper modelling of surface roughness [12].

The near wall treatment, which is used in ANSYS CFX-Solver (Scalable Wall Functions, Automatic Wall Treatment) is appropriate when walls are considered as hydraulically smooth. For rough walls, the logarithmic profile exists but moves closer to the wall and the near wall treatment becomes more complex, since it now depends on two variables: the dimensionless wall distance y^+ and the mean roughness height (R_a).

The arithmetic average of absolute roughness, which must be specified like the wall boundary conditions, is presented in many commercial software with the sand-grain roughness equivalent [12]. It is important to consider that the sand-grain roughness height is not equal to the geometric roughness of the surface. Wall friction depends on the type of roughness (shape, distribution, etc.) and not only on roughness height. Therefore, determining the appropriate equivalent sand-grain roughness height is crucial.

In this paper, we use basic relations for the incompressible fluid motion with the Reynolds-Averaged Navier-Stokes system of equations.

$$\frac{\partial \overline{u}_i}{\partial x_i} = 0, \qquad \frac{\partial \overline{u}_i}{\partial t} + \frac{\partial \overline{u}_i \overline{u}_j}{\partial x_j} = -\frac{1}{\rho}\frac{\partial \overline{p}}{\partial x_i} + \nu_t \nabla^2 \overline{u}_i + \frac{\partial \tau_{ij}}{\partial x_j}. \tag{2}$$

Usual logarithmic relation for the near wall velocity is presented by the equation:

$$u^+ = \frac{U_t}{u_\tau} = \frac{1}{\kappa}\ln(y^+) + C, \tag{3}$$

where

$$y^+ = \frac{\rho \Delta y u_\tau}{\mu}, \tag{4}$$

$$u_\tau = \left(\frac{\tau_\omega}{\rho}\right)^{\frac{1}{2}}. \tag{5}$$

The above logarithmic relation for the near wall velocity is different if wall roughness is taken into account. The new logarithmic velocity profile is:

$$u^+ = \frac{U_t}{u_\tau} = \frac{1}{\kappa}\ln(y^+) + B - \Delta B, \tag{6}$$

where B = 5.2. The ΔB is a function of the dimensionless roughness height, h^+, defined as:

$$h^+ = \frac{h u_\tau}{\nu}, \tag{7}$$

and the dimensionless sand-grain roughness:

$$h_s^+ = \frac{h_s u_\tau}{\nu}. \tag{8}$$

In addition, for sand-grain roughness, ΔB is defined by:

$$\Delta B = \frac{1}{\kappa}\ln(1 + 0.3 h_s^+). \tag{9}$$

Depending on the dimensionless sand-grain roughness h_s^+, three roughness regimes are defined:

- Hydraulically smooth: $0 \le h_s^+ \le 5$,
- Transitional-roughness: $5 \le h_s^+ \le 70$,
- Fully rough flow: $h_s^+ \ge 70$.

2 CFD ANALYSIS OF ROUGH WALLS

In the paper, we also present the numerical results of flow analysis in the centrifugal pump, where wall roughness was taken into account.

Technical roughness, which has peaks and valleys of arbitrary shape and different sizes, can be presented by an equivalent sand-grain roughness [1]. In the Eq. (8), the variable h_s means the equivalent of average roughness height.

In the last ten years, many papers have dealt with the numerical analysis of the pump characteristics. The results have been obtained using different types of computational grids, different turbulent models, steady state or unsteady approach and different software. The most analyses were done by using hydraulic smooth walls.

If the roughness is not taken into account, some losses in the flow are neglected or underestimated. These losses depend on the absolute size of roughness and on the velocity of the fluid. Therefore many times the comparison between the numerically obtained efficiency and experimental results show different discrepancies, depending on operating conditions.

Before we started analyzing the flow in the pump, we had to check some basic relations between computational mesh parameters, turbulence models and roughness height. In order to obtain these answers, two simple test cases were performed. First, the flow near a flat plate and second the flow in a pipe.

In Fig. 2 the velocity distribution near the flat plate wall for four different sand-grain equivalent sizes 0 μm, 10 μm, 35 μm and 100 μm is presented, for the computational grid near flat plate with the size of the first element near the wall 10 μm.

The upper graph shows the complete velocity distribution in the boundary layer, while the lower graph shows just the velocity distribution inside 100 μm space near the wall.

The flow boundary conditions and computational grid for all four results in Fig. 2 are completely the same. The difference is just the roughness height.

Similar velocity distribution is presented in Fig. 3, where different mesh size near the wall is used, with the size of the first element near the wall 40 μm.

It is known that wall roughness increases the wall shear stress and breaks up the viscosity sublayer in the turbulent flows. The consequence is also the downward shift in the near wall velocity profile (Eq. 6).

In Fig. 2 it can be seen that for the very low values of y^+ (lower than 5) the velocity near the wall is even higher for rough walls in comparison

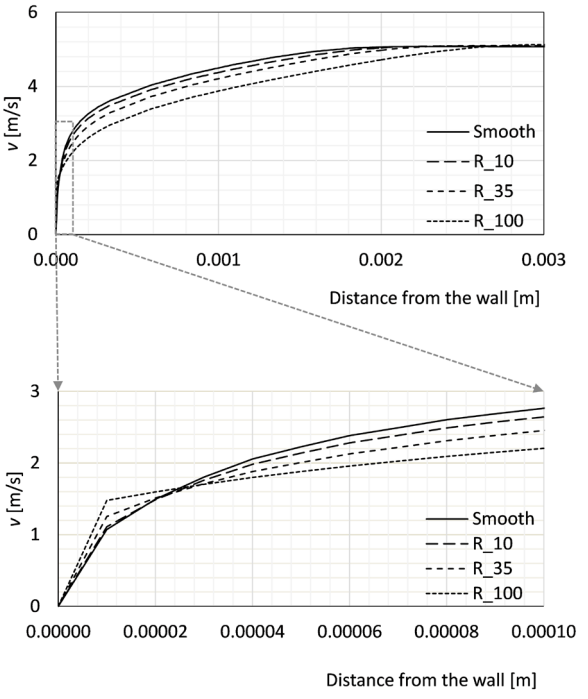

Fig. 2. *Velocity distribution in boundary layer*

with smooth walls. In Fig. 3, where y^+ is higher than 10, the situation is the opposite. The results show the influence of y^+ on the accuracy of the near wall velocity profile.

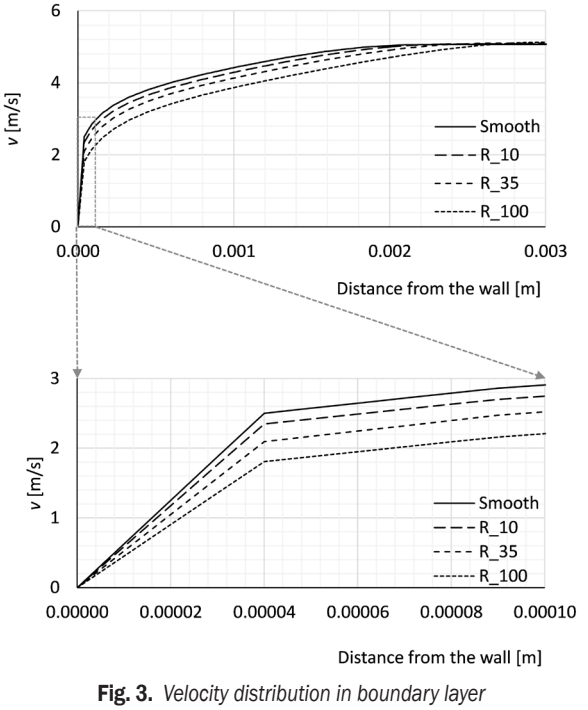

Fig. 3. *Velocity distribution in boundary layer*

The results in Figs. 2 and 3 show that too small y^+ is not suitable for the analysis of the losses, where rough walls are taken into account.

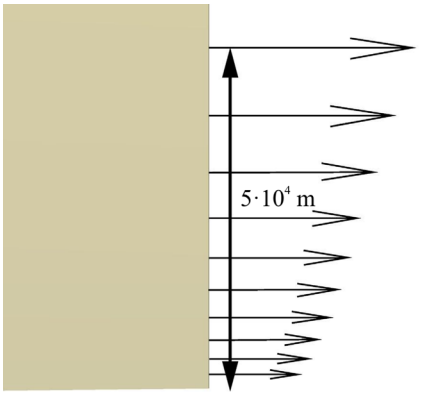

Fig. 4. *Velocity vectors in boundary layer*

The second test case of the flow analysis was the flow in the circular pipe (Fig. 4). The length of the pipe is 1.5 m and the diameter is 0.05 m. The results of this test show the influence of the computational mesh size near the wall on the accuracy of the results. The obtained CFD results were compared with the theoretical results, calculated using theoretical Moody friction factor (Eq. 10). In Fig. 5 a comparison of ratio between theoretical and numerical losses for different roughness heights and different size of dimensionless parameter y^+ is presented.

Theoretical results were obtained by the following equations:

$$\xi_{th} = \lambda \frac{L}{D} \frac{\rho u^2}{2}, \tag{10}$$

$$\lambda = \frac{1.325}{\left[\ln\left(\frac{h}{3.7D} + \frac{5.74}{\mathrm{Re}^{0.9}}\right)\right]^2}, \tag{11}$$

for $5000 \leq \mathrm{Re} \leq 10^8$ and $10^{-6} \leq h/D \leq 10^{-2}$.

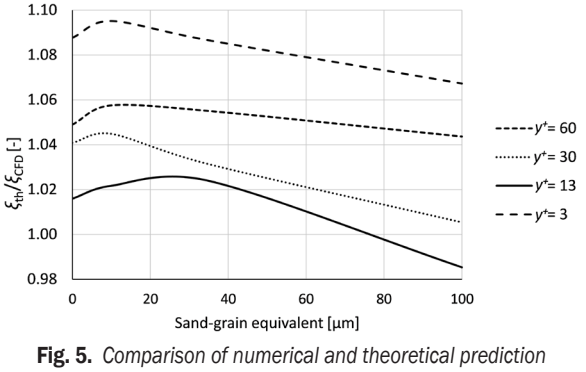

Fig. 5. *Comparison of numerical and theoretical prediction of losses of the flow in pipe*

The above results show that the influence of the y^+ is significant and we can conclude that a very small y^+ over predicts the losses in circular pipe. Very high values give better results but still over predict the losses.

3 CFD ANALYSIS OF THE FLOW IN PUMP

Comparison of the centrifugal pump efficiency obtained by measurement and numerical results, where only smooth walls were taken into account, shows that efficiency difference is not a constant for different operating regimes, but is much higher at full load than at part load. The reasons for such results can be different. We know that real walls are rough (Fig. 6) thus taking wall roughness into account in the numerical analysis can probably improve the results.

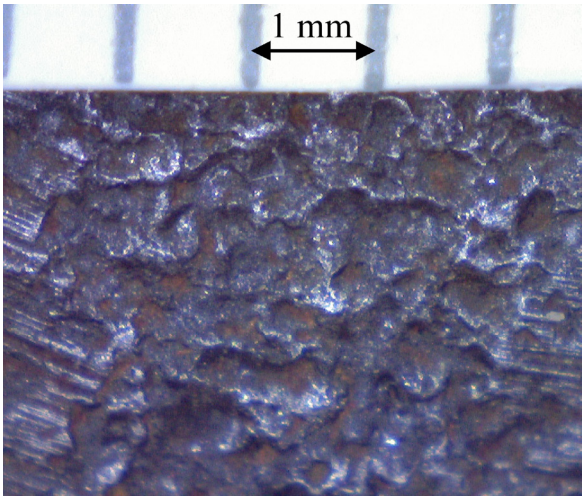

Fig. 6. *Microscope view of pump impeller surface made of cast iron*

Because of the above-mentioned differences, the efficiency analysis for different wall roughness and for at least five flow rates from part load to full load regime (Table 1) was performed.

Table 1. *Operating points and roughness height*

Flow rate = Q/Q_{BEP}	Roughness [μm]
0.73	0
0.87	50
1.00	100
1.13	
1.27	

A numerical analysis of the pump was done for five flow rates and for each operating point with three different roughness heights (Table 1). In Table 1 the

flow rates are presented relatively depending on best efficiency point (BEP) flow rate.

The numerical analysis results of the flow in the pipe gave us the basic recommendations about the required computational grid parameters and overall quality for the accurate analysis of the flow in the centrifugal pump (Fig. 7). The specific speed the analysed pump is n_q=24. The main geometric parameters of the pump are:

- inlet diameter 0.16 m,
- outlet diameter 0.33 m,
- outlet width 0.031 m.

Fig. 7. *Computational domain of the pump*

CFD analyses were done with computational grids with about 13.5 million elements (Fig. 8). The y^+ depends on the size of the first element and on the size of the speed. Because the numerical analysis was done for different flow rates, it is not possible to have the same value of y^+ for all operating regimes just with one computational grid.

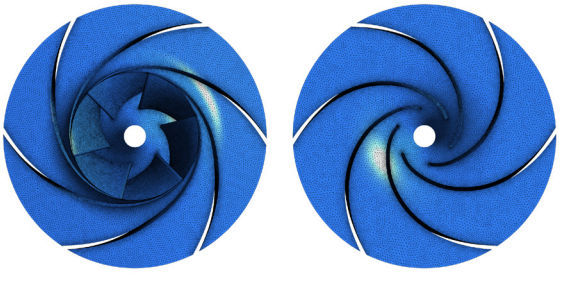

Fig. 8. *Computational grid of pump impeller*

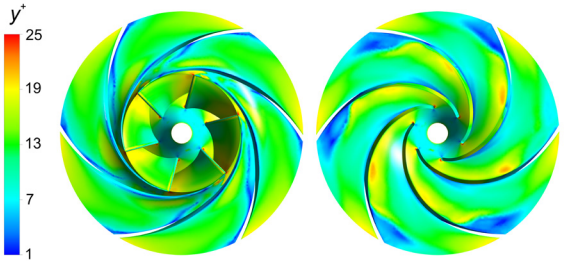

Fig. 9. *Distribution of y^+ for BEP*

In our case, we had one computational grid for all flow rates and y^+ distribution on the impeller blades is presented in Fig. 9 for BEP. For the flow rates smaller than BEP, the y^+ is smaller, for the full load operating regime the y^+ is bigger than in the Fig. 9.

At the BEP, y^+ is between 10 and 30 in most areas, but on the part of pressure side of the impeller blades, the y^+ is smaller than 10 and on the part of suction side it is bigger than 30.

The quality of computational grid was provided with average aspect ratio around 100 at the near-wall elements and with the expansion ratio of 1.2. The size of elements outside the boundary layer was defined depending on the local flow properties, for each part of the pump.

The fluid in the CFD analysis was water at 25 °C, with density 997 kgm^{-3} and dynamic viscosity 8.899 kgm^{-1}s^{-1}.

The results of time dependent efficiency distribution for the two operating regimes are presented in Figs. 10 and 11. Relative efficiency is defined as a ratio between efficiency of each operating regime and maximal efficiency obtained with measurements. In Fig. 10 the results for the smallest flow rate (0.055 m^{3}s^{-1}) are presented and in this case the difference between the average results obtained using smooth walls and different heights of roughness is quite small, less than five percent.

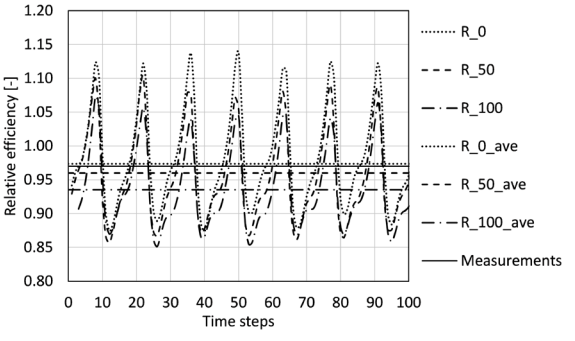

Fig. 10. *Pump efficiency distribution for different values of wall roughness for small flow rate*

If we compare the average results at part load for different heights of the roughness and for smooth wall with the results of measurements, the conclusion is that only the efficiency for smooth walls is noteworthy higher than the measured efficiency. From measurements of the pump wall roughness the approximate value of the R_a value was obtained, which is around 5 μm and with the algorithm in the paper [1] this value can be calculated to the sand-grain roughness coefficient. For the investigated pump, the

sand-grain roughness equivalent is approximately 50 μm.

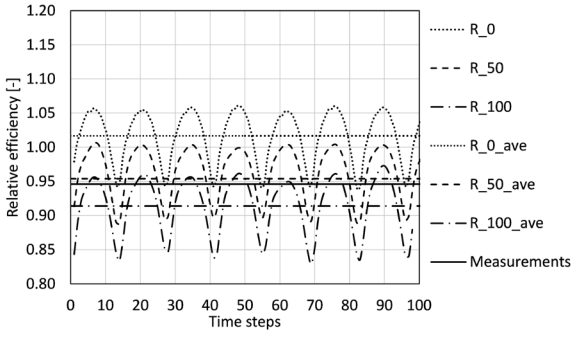

Fig. 11. *Pump efficiency distribution for different values of wall roughness for high flow rate*

In Fig. 11 the results for the flow rate bigger than the best efficiency point (0.095 m^3s^{-1}) are presented and in this case the difference between the results obtained using smooth walls and different heights of roughness is much bigger, more than ten percent.

At this operating point, roughness influence is slightly different. Efficiency for smooth walls and for 50 μm roughness is higher than measured efficiency. The efficiency is smaller only for the 100 μm roughness.

In Figs. 10 and 11 only the results for smooth walls and two values of the roughness are presented, because the computational time for unsteady analysis was quite long and we did not make calculations for the same number of time steps for all values of the roughness.

It is not possible to take all flow parameters into account, but from the obtained results (Fig. 12), we can conclude that wall roughness is an important parameter in accurate numerical analyses, especially when absolute accuracy is important.

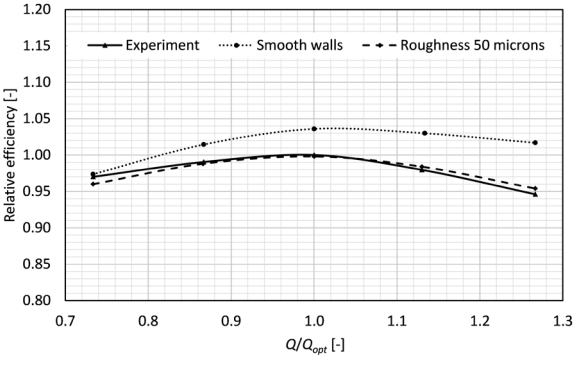

Fig. 12. *Comparison of pump efficiency characteristics between experiment and numerical analysis*

Comparison between numerical and experimental results is presented in Fig. 12. Results are presented for different flow rates between 0.7 and 1.3 Q_{BEP}. For small flow rates, all results are very close and the difference between experimental results and results for rough wall is very small.

The measurements of the efficiency were done using different instruments:

- flow rate - electromagnetic flow meters,
- head – pressure gauge,
- power – wattmeter,
- rotational speed – digital rpm device.

The measurements uncertainty was in accordance with the international standard ISO 9906. The relative uncertainties of the used instruments for each variable are:

- flow rate ±1.5 %,
- head ±1 %,
- power ±1 %,
- rotational speed ±0.35 %.

The different situation is for the operating point right of the best efficiency point, where the difference between experimental results and results for smooth wall is around seven percent. Taking wall roughness into account, the numerical results approach the experimental results, but the difference is still around one percent, approximately the same order of magnitude as at a part load operating regime.

The comparison in the Fig. 12 is presented for only one sand-grain equivalent roughness size 50 μm, which is supposedly the closest to the real value and was obtained at roughness measurements of the impeller surface and calculated to the appropriate sand-grain equivalent. The results considering wall roughness are better in comparison with the results for smooth walls, but there are still some discrepancies, which are probably also caused by different parameter y^+, since the computational grid for all calculations was the same. There are also other possible reasons for the inaccuracy of the numerical results, which were not taken into account.

4 CONCLUSIONS

The numerical prediction of energetic characteristics of different hydraulic machines can be obtained using different CFD codes. Sometimes numerical results match very well with the experimental ones but in many cases the situation is different. That is why the researchers paid a lot of attention to the quality of computational grid, appropriate turbulence models,

accurate boundary conditions and other necessary flow and fluid parameters.

Nevertheless, consideration of the wall roughness usually remained forgotten. Wall roughness is present at the majority of the industrial flow analyses. One of the possible reasons why the wall roughness is neglected is the required quality of computational grid or some problems with turbulence models.

The numerical analysis of the flow over rough walls can be performed in two ways. First with exact geometrical modelling of the wall roughness, and second with using special equivalent parameters for roughness prediction. From the computational point of view, the first method is very demanding and time consuming. That is why many CFD codes use different coefficient, like sand-grain equivalent coefficient.

Because there is not a lot of research work on this topic, this paper presents some relations between the roughness coefficient and the usage of numerical methods for accurate prediction of losses in centrifugal pumps. In particular, the focus was on the size of the computational grids near the walls.

The paper also presents the influence of the dimensionless parameter y^+ on the accuracy of numerical results with comparison of theoretical and numerical results. It is shown that very small values of y^+ give a big difference between theoretical and numerical results. The usage of appropriate y^+ is necessary, because the surface roughness increases the wall shear stress in the turbulent boundary layer.

The second part of the paper deals with the numerical prediction of unsteady pump efficiency for different values of wall roughness. The results show that the influence of the wall roughness is not negligible thus it is very important to consider it. The main problems are the exact prediction of the sand-grain roughness equivalent and using the appropriate y^+ coefficient for all calculations.

Further investigations will analyze different shapes of wall roughness in terms of finding the accurate interface between real wall roughness and sand-grain roughness equivalent.

5 NOMENCLATURES

B Constant, [-]
C Log-layer constant, [-]
D Diameter, [m]
h Roughness, [m]
h^+ Dimensionless roughness height, [-]
h_s^+ Dimensionless sand-grain roughness, [-]
L Length, [m]
n_q Specific speed, [rpm]
Q Flow rate, [m^3s^{-1}]
Q_{opt} Optimal flow rate, [m^3s^{-1}]
p Pressure, [Pa]
R_a Arithmetic average of roughness, [m]
u^+ Near wall velocity, [ms^{-1}]
u Velocity, [ms^{-1}]
U_t Velocity at a distance Δy, [ms^{-1}]
u_τ Friction velocity, [ms^{-1}]
Δy Distance from the wall, [m]
y^+ Dimensionless distance from the wall, [-]
ΔB Shift, [-]
κ Von Karman constant, [-]
λ Friction factor, [-]
μ Dynamic viscosity, [$kgm^{-1}s^{-1}$]
ν Kinematic viscosity, [m^2s^{-1}]
ν_t Turbulent kinematic viscosity, [m^2s^{-1}]
ξ Losses, [Pa]
ρ Density, [kgm^3]
τ_ω Wall shear stress, [Pa]

6 REFERENCES

[1] Adams, T., Grant, C., Watson, H. (2012). A simple algorithm to relate measured surface roughness to equivalent sand-grain roughness. *International Journal of Mechanical Engineering and Mechatronics*, vol. 1, no. 2, p. 66-71, **DOI:10.11159/ijmem.2012.008**.

[2] Aupoix, B. (2014). Wall Roughness Modelling with k-ω SST Model, *10th International ERCOFTAC Symposium on Engineering Turbulence Modelling and Measurements*, Marbella.

[3] Aupoix, B., Spalart, P.R. (2003). Extensions of the Spalart-Allmaras Turbulence Model to Account for Wall Roughness. *International Journal of Heat and Fluid Flow*, vol. 24, no. 4, p. 454-462, **DOI:10.1016/S0142-727X(03)00043-2**.

[4] Lin, C., Moeng, C., Sullivan, P.P., McWilliams, J.C. (1998). The effect of surface roughness on flow structures in a neutrally stratified planetary boundary layer flow. *Physics of Fluids*, vol. 9, no. 11, **DOI:10.1063/1.869439**.

[5] Akinlade, O.G. (2005). *Effects of Surface Roughness on the Flow Characteristics in a Turbulent Boundary Layer*, PhD Thesis. Department of Mechanical Engineering, University of Saskatchewan, Saskatoon.

[6] George, J., De Simone, A., Iaccarino, G., Jimenez, J. (2010). Modeling roughness effects in turbulent boundary layers by elliptic relaxation, *Center for Turbulence Research, Proceedings of the Summer Program*, p. 119-128.

[7] Juckelandt, K., Bleeck, S., Wurm, F.-H. (2015). Analysis of losses in centrifugal pumps with low specific speed with smooth and rough walls, *Proceedings of 11th European Conference on Turbomachinery Fluid dynamics & Thermodynamics*, p. 1-10.

[8] Kang, Y.-S., Yoo, J.-C., Kang, S.-H. (2006). Numerical prediction of roughness effects on the performance degradation of an axial-turbine stage. *Journal of Mechanical Science and*

Technology, vol. 20. no. 7, p. 1077-1088, **DOI:10.1007/BF02916007**.

[9] Levin, L.Y., Semin, M.A., Klyukin, Y.A. (2014). Estimation of wall roughness functions acceptability in CFD simulation of mine ventilation networks. *Proceedings of XLII International Summer School–Conference*, p. 25-32.

[10] Dutta, R., Nicolle, J., Giroux, A.M., Piomelli, U. (2016). Evaluation of turbulence models on roughened turbine blades. *28th IAHR Symposium on Hydraulic Machinery and Systems, Grenoble*, **DOI:10.1088/1755-1315/49/6/062007**.

[11] Vijiapurapu, S., Cui, J. (2010). Performance of turbulence models for flows through rough pipes. *Applied Mathematical Modelling*, vol. 34, no. 4, p. 1458-1466, **DOI:10.1016/j.apm.2009.08.029**.

[12] ANSYS CFX Solver Theory Guide (2016). Release 17.0., ANSYS, Inc., Canonsburg.

Strojniški vestnik - Journal of Mechanical Engineering 63(2017)9, 537-547

DOI:10.5545/sv-jme.2017.4320 Original Scientific Paper
Received for review: 2017-01-11
Received revised form: 2017-05-04
Accepted for publication: 2017-06-16

Electric-Thermo-Mechanical Analysis of Joule Heating in Dilatometric Specimens

Martin Herrejón-Escutia[1] – Gildardo Solorio-Díaz[1] – Héctor Javier Vergara-Hernández[2] – Edgar López-Martínez[3] – Gerardo Marx Chávez-Campos[2] – Octavio Vázquez-Gómez[2,4,*]

[1] Michoacan University of Saint Nicolas of Hidalgo, Mechanical Engineering, Mexico
[2] Morelia Institute of Technology, Mexico
[3] University of the Isthmus, Campus Tehuantepec, Mexico
[4] National Council of Science and Technology, Mexico

A mathematical model of Joule heating was developed for an AISI 304 stainless steel in a hollow cylinder dilatometric specimen. The model was developed by means of creating a balance of energy by coupling the generation term due to the Joule heating and the thermal expansion of the specimen. A Newtonian heating system was assumed for a volume element, and it was resolved by means of the finite differences method, generating its own computer code in the Scilab free-license software. The model considers the thermophysical and electrical properties of steel, depending on the temperature. Thermal interactions at the boundary and the linear thermal expansion coefficient were determined by solving the inverse heat conduction problem (IHCP) using the thermal profile and thermal expansion measured experimentally by means of a direct heating device. The model was validated by comparing the thermal response and experimental thermal expansion with simulated responses for different heating rates.

Keywords: mathematical model, continuous heating, Joule effect, dilatometry, AISI 304 stainless steel

Highlights

- *A mathematical model of Joule heating was developed to predict the thermal history and expansion of a dilatometric specimen.*
- *Thermal boundary conditions were determined for the Joule heating of a dilatometric specimen by solving the Inverse heat conduction problem.*
- *Coefficient of linear thermal expansion dependent of the temperature was determined by solving the mathematical model and develop of an experimental device of Joule heating.*
- *The mathematical model was satisfactorily validated comparing the thermal history and strain percentage by dilatation with the experimental measurements as a function of the heating rate.*

0 INTRODUCTION

Dilatometry is one of the most commonly used thermal analysis techniques in the study of solid-solid phase transformations in ferrous alloys [1] and [2], as it makes it possible to monitor (in real time) the microstructural evolution of a phase in terms of the changes in volume that occur during a thermal cycle. When a material undergoes a phase transformation, the crystal structure is modified, and this is manifested as a positive (expansion) or negative (contraction) volume change. This analysis technique makes it possible to determine the critical transformation temperatures that can be used for constructing isothermal transformation (IT) diagrams and/or continuous cooling and continuous heating transformation (CCT and CHT) [1] to [4]. These diagrams are of practical interest in various metallurgical applications, such as the simulation and design of heat treatments, in the prediction of mechanical properties, and in the formulation of mathematical models to resolve the thermal and microstructural fields during the formation or decomposition of a phase [5] and [6]. Many of these studies use commercial dilatometry equipment to determine transformation kinetics through dilatometric specimens of different shapes and sizes, for example, solid cylindrical shape, hollow, or flat in small sizes, ensuring that the changes in volume obtained are due solely to the phase transformation or the internal changes in the material and not to distortion caused by the thermal shock in the heating and quenching stages. Likewise, the dilatometry devices can use different heating media such as magnetic induction, thermal radiation, and direct current or Joule heating [3], [7] and [8]. This latter medium is characterized by providing thermal homogeneity in the material and good control of the heating rate (HR), which can remain constant for the whole heating stage. Another characteristic of Joule heating is that heat generation in the material is internal, which provides a quasi-linear relationship between the current and the temperature, provided no phase transformation exists [9], unlike

*Corr. Author's Address: National Council for Science and Technology of Mexico, Av. Insurgentes 1582, 03940 Mexico City, Mexico, ovazquezgo@conacyt.mx

radiation or induction heating in which the behaviour of the temperature depends on the electrical resistance and the refractory material of the furnace (radiation), or the frequency and magnitude of the electric current, as well as the type of inductor (magnetic induction). Another advantage of the direct methods is that they make it possible to obtain an alternate measurement on the most accurate and exact temperature at which the material acts as an electric heating resistance, which can be monitored in real time depending on voltage and intensity. However, because the material is the electrical resistance of the circuit, it is difficult to control the system efficiently. For that, a prior thermoelectric characterization is needed before obtaining the optimal control parameters, because the materials have different thermal and electric properties. In this paper, a mathematical model of Joule heating was implemented with hollow cylindrical dilatometric specimens to predict history and thermal expansion. The purpose of the model is to understand and estimate the thermoelectric behaviour of conductor materials in a direct experimental heating device.

1 MATHEMATICAL MODEL

1.1 Problem Description

Fig. 1 shows the dimensions of a hollow cylindrical dilatometric specimen of AISI 304 stainless steel, heated using the Joule heating process. The selection of material mainly owes to the fact that AISI 304 steel does not have internal changes to its structure, such as phase transformation, in the operating temperature range (250 °C to 850 °C). The specimen has a 1-mm-thick wall and is subjected to heating by the Joule effect under natural convection conditions on the outer surface of the specimen. Under these conditions, the Biot number is 4.5×10^{-4}; consequently, a Newtonian heating system in the radial direction is considered for the problem. Taking into consideration that it is a Newtonian system, it is expected that the temperature gradient in the radial direction should be negligible, creating a totally isothermal zone in this direction. During heating, the specimen expands due to the thermal expansion of the material, which is associated with the thermal strain generated. Meanwhile, the specimen is attached to a system of jaws that are used as power supply terminals and cooled though a moderate internal water flow, which makes the temperature profiles parabolic and symmetric in the axial direction, and ensures that the temperature reaches its highest values in the middle part of the specimen. This temperature is representative of the amount of energy generated in the system by the Joule heating.

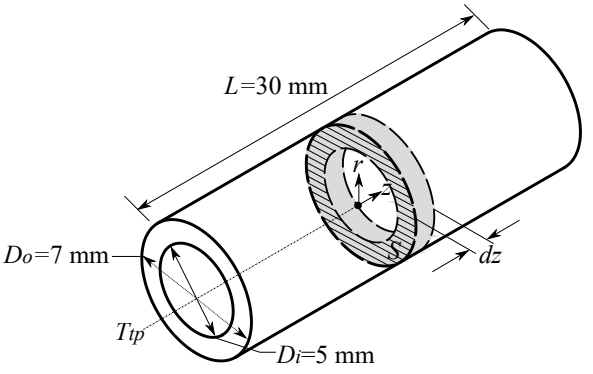

Fig. 1. *Hollow cylindrical specimen heated by the Joule effect*

1.2 Thermoelectric Model

An energy balance inside the isothermal zone indicated by the volume elements *dz* was made based on Fig. 1, considering the heat generation and accumulation terms as well as heat loss due to convection through the specimen walls:

$$Q_a = Q_g - Q_l, \tag{1}$$

where the terms Q_a, Q_g *and* Q_l are accumulated heat, the generated heat and the lost heat by convection, respectively. The accumulated heat is defined based on the change of temperature with regard to the time and thermophysical properties of the material such as:

$$Q_a = \rho C_p V \frac{dT}{dt}, \tag{2}$$

where T and t are heating temperature and time, respectively, ρ is density, C_p is specific heat and V is the element volume. In the case of the hollow cylinder, the volume is defined through the transverse area S which is a function of the radii of the cylinder and the thickness of the volume element $L=dz$ expressed as:

$$V = S \cdot L = \pi (r_o^2 - r_i^2) dz, \tag{3}$$

where r_o and r_i are the external and internal radii of the cylinder, respectively. Heat lost by convection and radiation is expressed based on an overall heat transfer coefficient (OHTC) on the outer and inner surfaces of the specimen defined as h_o and h_i, respectively. However, the environmental temperature of the outer surface T_o is different from the inner surface T_i due to the fact that the outer surface is completely exposed to the environment, T_o remains constant, making

it possible for heat transfer by natural radiation and convection, whereas the inner surface is considered to be a closed cavity in which air is confined and not completely still, limiting natural convection heat transfer by natural convection, and the governing mechanism therefore being radiation heat transfer, this causes the value of the T_i to increase during heating, but always below the temperature of the specimen, generating a temperature gradient towards the interior. From this, we have:

$$Q_l = h_i(T - T_i)A_i + h_o(T - T_o)A_o, \tag{4}$$

where $A_i = 2\pi r_i dz$ is the inner surface, and $A_o = 2\pi r_o dz$ is the outer surface of the specimen.

Finally, the heat generated by Joule heating **[10]** Q_g is associated with the energy generated by the passage of electric current and is defined through Watt's law as:

$$Q_g = I^2 R_e, \tag{5}$$

where I is the intensity of electric current, R_e is the electric resistance that can be expressed in terms of resistivity ρ_e or electrical conductivity σ_e, such as:

$$R_e = \rho_e \frac{L}{S} = \frac{1}{\sigma_e}\frac{L}{S}. \tag{6}$$

Consequently, the resistance of the volume element is:

$$R_e = \left(\frac{1}{\sigma_e}\right)\frac{dz}{\pi(r_o^2 - r_i^2)}. \tag{7}$$

Substituting the Eqs. (2) to (7), in Eq. (1), we have the governing equation for the problem of Newtonian heating by the Joule effect:

$$\rho C_p \pi(r_o^2 - r_i^2)dz\frac{dT}{dt} = \frac{I^2}{\sigma_e}\left[\frac{dz}{\pi(r_o^2 - r_i^2)}\right] - \\ -h_i(T - T_i)2\pi r_i dz - h_o(T - T_o)2\pi r_o dz, \tag{8}$$

dividing by $\rho C_p \pi(r_o^2 - r_i^2)dz$,

$$\frac{dT}{dt} = \left(\frac{I^2}{\sigma_e}\right)\left(\frac{1}{\rho C_p}\right)\left[\frac{1}{\pi(r_o^2 - r_i^2)}\right]^2 - \\ -\frac{2\left[h_i(T - T_i)r_i + h_o(T - T_o)r_o\right]}{\rho C_p(r_o^2 - r_i^2)}. \tag{9}$$

Eq. (9) is a differential equation describing the heating rate, considering accumulated heat, heat generated by the Joule effect, heat dissipated by convection and radiation toward the heating medium.

1.3 Thermal Dilatation

Temperature changes cause thermal dilatation, expansion or contraction, in materials. In most of these, unitary thermal strain **[11]** ε_T is expressed in terms of temperature change such as:

$$\varepsilon_T = \alpha \cdot \Delta T, \tag{10}$$

where α is the linear thermal expansion coefficient and ΔT is the temperature change regarding a reference temperature.

By analysing the thermal strain of the volume element of Fig. 1 and considering the real strain ε **[12]** in terms of area we have:

$$\varepsilon = \ln\left(\frac{A}{A'}\right) = \ln\left(\frac{r_o^2 - r_i^2}{r'^2_o - r'^2_i}\right). \tag{11}$$

Assuming that there are no temperature gradients in the radial direction, it is expected that the temperature in the volume element be uniform as will the linear thermal expansion, maintaining the difference between the out and inner radii Δr. Based on the above, Eqs. (10) and (11) are equalized at the strain value, obtaining an expression for the instant outer radius r'_o according to temperature change and the linear thermal expansion coefficient such that:

$$r'_o = \frac{2r_o - \Delta r}{2 \cdot \exp(-\alpha \cdot \Delta T)} + \frac{\Delta r}{2}. \tag{12}$$

Dilatation strain ε_d is calculated based on the relationship of the instant diametric change $\Delta D'$ and initial diameter D_o through:

$$\varepsilon_d = \frac{\Delta D'}{D_o} = \frac{r'_o - r_o}{r_o}. \tag{13}$$

1.4 Method of Solution

The proposed model in Eq. (9) may be solved analytically by considering constant thermophysical and electric properties; however, this does not happen in reality. Consequently, a solution of this type would be inaccurate. To provide a correct solution to the model it is necessary to consider the thermophysical and electrical properties of the material, and current intensity based on temperature and time: $\rho(T)$, $C_p(T)$, $\sigma(T)$ and $I(t)$, respectively, making Eq. (9) take the form of a nonlinear differential equation whose analytic solution is not easily obtained. Consequently, it is proposed to use an approximate solution based on the explicit finite difference method (EFDM). In the

EFDM, temperature profile is a function of the time and temperature and is calculated 'back time'. The method of solution was codified in the Scilab free-license software® for which the differential forward form was used ahead of temperature time dT/dt [13] as:

$$\frac{dT}{dt} = \frac{T^{n+1} - T^n}{\Delta t}, \tag{14}$$

where T^{n+1} is temperature future time t^{n+1} and T^n temperature in actual time t^n. Substituting Eq. (14) in Eq. (9) and employing the EFDM we have,

$$T^{n+1} = \left[\frac{I^2}{\sigma \rho C_p} \left(\frac{1}{\pi \left(r_o^2 - r_i^2 \right)} \right)^2 - \frac{2}{\rho C_p \left(r_o^2 - r_i^2 \right)} \cdot \left[h_o \left(T^n - T_o \right) r_o + h_i \left(T^n - T_i \right) r_i \right] \right] \Delta t + T^n. \tag{15}$$

Eq. (15) describes the evolution of the temperature field according to thermophysical and electrical properties, the heat transfer coefficient and the intensity of electric current, depending on the temperature, time and specimen dimensions.

2 EXPERIMENTAL DEVELOPMENT

For the development of the experimental tests a Joule heating device was built using instrumentation with a source of power of 2.25 kW coupled to a copper conductor jaw system to supply power. The jaws were cooled by means of a constant water flow in order to keep the ends of the specimen at a temperature of approximately 40 °C; ensuring the concentration of the thermal field in the middle of the specimen. The temperature was measured by means of an infrared pyrometer based on a temperature of 250 °C. In turn, the dilatation in the radial direction was measured using micrometer laser with a resolution of ±1.0 μm. The devices used were controlled by a CompactRio NI cRIO 9075 data acquisition system. The experimental device can be seen in Fig. 2.

Specimens of an AISI 304 stainless steel were machined for the heating tests according to Fig. 1. The specimens were heated to a maximum temperature of 850 °C with different heating rates: 0.75 °C s^{-1}, 1.08 °C s^{-1}, and 1.58 °C s^{-1}. Later, they were cooled to room temperature under natural convection conditions with still air and without passage of electric current. During heating, time, thermal response and variation of diameter were measured and acquired.

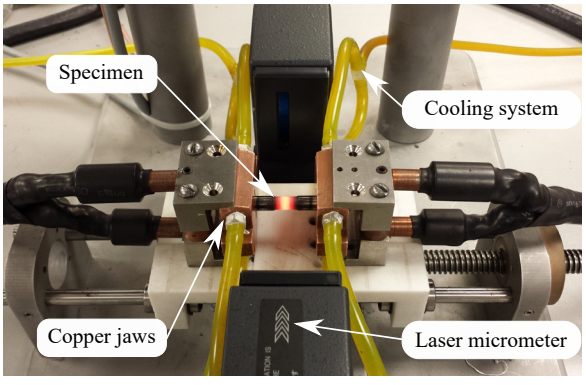

Fig. 2. *Experimental Joule effect heating device*

3 RESULTS

3.1 Experimentation

Results of the tests are shown in Fig. 3: a) thermal and current intensity history and b) strain percentage by dilatation $\%\Delta D'/D_o$. From Fig. 3a we can see the

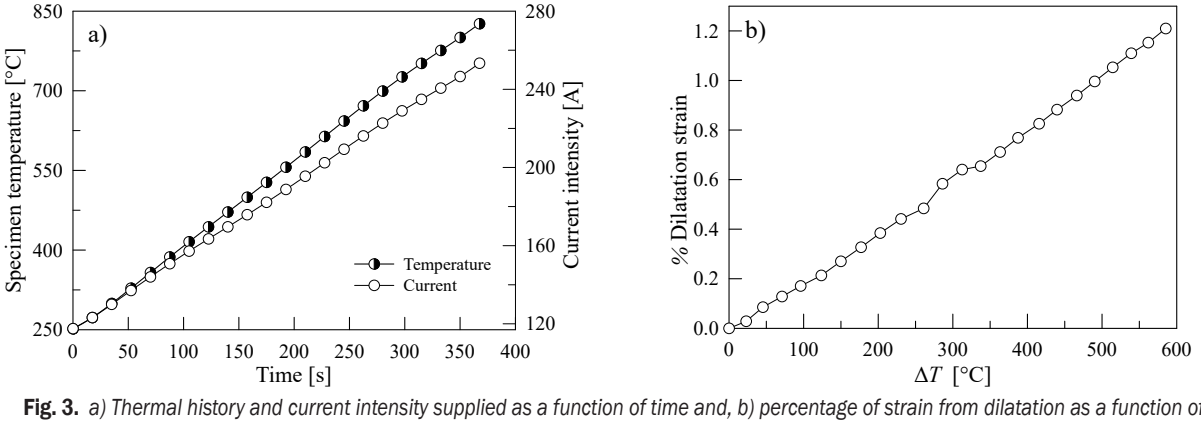

Fig. 3. *a) Thermal history and current intensity supplied as a function of time and, b) percentage of strain from dilatation as a function of temperature change, in a hollow cylindrical specimen heated by the Joule effect to an average heating rate of 1.58 °C s^{-1}*

thermal history measured in the middle section on the outer surface of the specimen, where it can be seen that temperature measurement starts when an approximate temperature of 250 °C is reached and continues up to a temperature of 850 °C, in approximately 380 seconds, obtaining an average heating rate of 1.58 °C s^{-1}. In the same Fig. 3a the current intensity supplied to the specimen in shown with regards to time. The current intensity required to reach an initial temperature of 250 °C is less than 120 A, which increases in direct proportion to the temperature until it reaches an approximate value of 260 A. The behaviour of the current intensity is similar to that of the thermal history, there being a linear relationship between the current supplied and the specimen temperature.

In contrast, the percentage of dilatation strain is shown in Fig. 3b as a function of the temperature change with regard to initial temperature $\Delta T = T - 250$. As with temperature and current intensity, the percentage of dilatation strain presents a behaviour directly proportional to the ΔT value until reaching a change when approaching 600 °C.

3.2 Thermal Boundary Condition (TBC)

As indicated in the model, Thermal Boundary Conditions between the outer and inner surfaces with the environment were defined based on an overall heat transfer coefficient, $h_o(T)$ and $h_i(T)$. In the case of the outer surface, the value of the coefficient must be determined based on the temperature, as the heat flow of the specimen toward the environment is given by the contribution of heat lost by convection and radiation:

$$h_o = h_c + h_r, \tag{16}$$

where h_c is the heat transfer coefficient by convection and h_r is the radiation coefficient. The heat transfer coefficient from natural convection is obtained based on the definition of the Nusselt dimensionless number, Nu_D such as:

$$h_c = \frac{Nu_D \cdot k_{air}}{D_o}, \tag{17}$$

where k_{air} is the thermal conductivity of the air and D_o is the initial outside diameter of the specimen. The value of Nu_D is obtained based on the empirical correlation developed by Rebrov [14], for horizontal cylinders with diameters between 1.31 and 9.9 mm subjected to natural convection,

$$Nu_D = \left[0.98 - 0.01\left(\log Gr_D \Pr\right)^2\right]\left(Gr_D \Pr\right)^x, \tag{18}$$

where Gr_D is the Grashof dimensionless number evaluated with the outer diameter of the specimen and Pr is the Prandtl number while the exponent x is expressed as:

$$x = 0.14 + 0.015\log\left(Gr_D \Pr\right). \tag{19}$$

In contrast, the radiation transfer coefficient h_r is defined as [15]:

$$h_r = \varepsilon \cdot \sigma \left[\frac{\left(T^4 - T_o^4\right)}{T - T_o}\right], \tag{20}$$

where ε is the material emissivity and σ is the Stefan Boltzmann constant and temperatures are expressed in Kelvin.

Fig. 4 shows the heat transfer coefficients as a function of the temperature for the outer surface of the specimen. The natural convection coefficient is practically constant over the whole temperature range, while the radiation coefficient increases exponentially with the rising specimen temperature, indicating that heat transfer by radiation is the high-temperature governing mechanism.

To obtain the TBC inside the specimen, it was necessary to determine the environmental temperature inside the specimen. For this, the temperature of the middle was measured with a thermocouple placed inside the specimen as shown in Fig. 1.

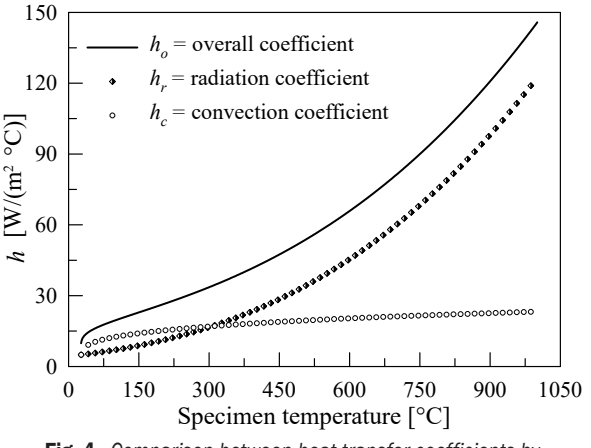

Fig. 4. *Comparison between heat transfer coefficients by convection h_c, radiation h_r, and overall coefficient ho to estimate boundary condition convective in the outer surface of the specimen*

However, the temperature acquired by the thermocouple not only considers heat transfer by convection between the thermocouple and the environment but also radiation between the inner surface and the tip of the thermocouple due to the difference of temperature between the surface and the

environment. This causes the temperature acquired by the thermocouple to be an average temperature between the inner surface and the environment. For this the inner temperature is calculated using a balance of energy on the surface of the thermocouple, equalling the heat gained through radiation with heat lost by convection [16]:

$$\dot{q}_{conv,\rightarrow tp} = \dot{q}_{rad,\leftarrow tp}, \tag{21}$$

where the arrow shows the direction of heat flow, $\rightarrow tp$ toward the thermocouple, $\leftarrow tp$ from the thermocouple,

$$h\left(T_i - T_{tp}\right) = \varepsilon_{tp}\sigma\left(T_{tp}^4 - T^4\right), \tag{22}$$

where ε_{tp} is the emissivity of the thermocouple. For the inner temperature T_i,

$$T_i = T_{tp} + \frac{\varepsilon_{tp}\sigma\left(T_{tp}^4 - T^4\right)}{h}, \tag{23}$$

where, T_{tp} is the temperature acquired by the thermocouple of the centre, whose location is shown in Fig. 1, T is the specimen temperature and h is the heat transfer coefficient by convection between the tip of the thermocouple and the inner surface of the specimen. Fig. 5 shows a) the comparison between specimen temperature T, thermocouple temperature T_{tp} and the average inner temperature T_i calculated based on Eq. (23) as a function of heating time, and b) temperature of the inner room as a function of the specimen temperature.

Finally, to estimate TBC inside h_i the inverse heat conduction problem (IHCP) was solved [17] and [18]. Eq. (9) was resolved for h_i, supplying the thermal history of the specimen, the temperature of the inner and outer room, the current intensity history, electrical and thermophysical properties dependent on the temperature for AISI 304 stainless steel, this data was obtained from the properties reported in the literature [19] and [20]. The IHCP was solved by means of a nonlinear Beck method [21] and [22]; the result is shown in Fig. 6.

In Fig. 6 you can see the behaviour of the overall heat transfer coefficient between the inner surface of the specimen and the environment. When the heating starts, the inner environment has a growing heat extraction capacity up to a temperature of 550 °C, mainly due to a temperature difference between the environment and the specimen. From this point, extraction remains practically constant around 315 W/(m² °C) until reaching a temperature approaching 800 °C, before reaching the maximum specimen temperature. At this point, the extraction capacity drops slightly due to heat saturation of the inner environment and for the heat loss due to convection-radiation in the opposite side of the specimen. This is a particular IHCP solution for the internal heat transfer coefficient due to the dependence of the inner geometry of the specimen.

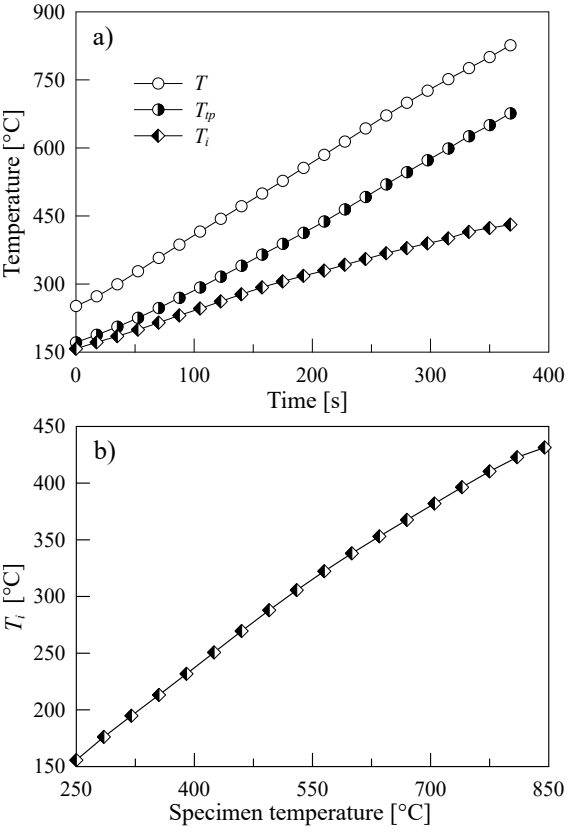

Fig. 5. *a) Comparison between specimen temperature T, thermocouple temperature T_{tp} and the average inner temperature T_i, as calculated based on Eq. (23), and b) temperature of the inner room as a function of the temperature of the specimen*

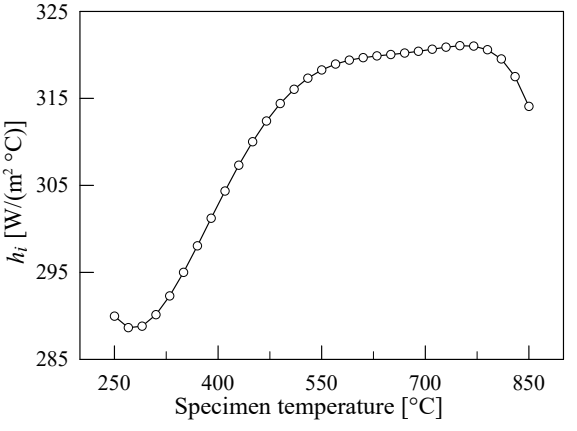

Fig. 6. Heat Transfer coefficient h_i for the inner surface, as a function of specimen temperature calculated based on IHCP solution

3.3 Determining the Linear Thermal Expansion Coefficient

The linear thermal expansion coefficient is determined based on dilatation strain and experimentally measured diameter change, considering that the thermal strain ε_T is equal to dilatation strain ε_d of the specimen.

$$\alpha = \frac{1}{D_o}\frac{\Delta D'_o}{\Delta T}, \tag{24}$$

where ΔT is the change of temperature, expressed as:

$$\Delta T = T^{n+1} - T_r, \tag{25}$$

where T^{n+1} is instantaneous temperature in future time t^{n+1}, for each instantaneous outside radius value r'_o, while T_r is the reference temperature corresponding to the initial outside radius r_o; T_r is a constant that coincides with initial specimen temperature. The linear thermal expansion coefficient obtained from the Eq. (24) and experimental measurements is shown in Fig. 7.

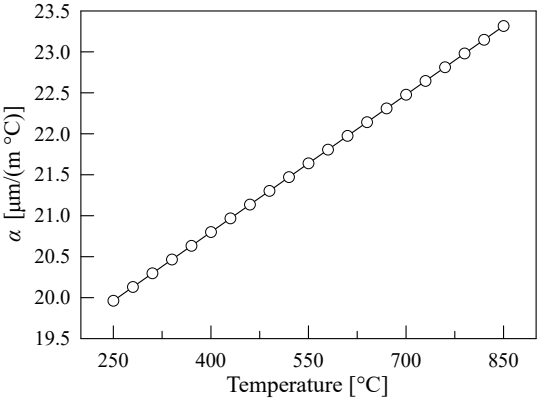

Fig. 7. Experimental linear thermal expansion coefficient α, as a function of temperature for an AISI 304 stainless steel

Fig. 7 shows that the linear thermal expansion coefficient maintains linear behaviour regarding temperature and because it was calculated based on the temperature change ΔT we have a different value for each of the future temperatures T^{n+1}. The average thermal expansion coefficient $\overline{\alpha}$ is 21.64 μm/(m °C), corresponding to stainless steel with an austenitic structure [23].

4 VALIDATION OF THE MATHEMATICAL MODEL

Fig. 8 shows the comparison between the experimental thermal history and that obtained by mathematical model for a heating rate of: 0.75 °C s^{-1}, 1.08 °C s^{-1}, and 1.58 °C s^{-1}. As mentioned previously, the model is supplied with thermophysical and electrical properties dependent on the temperature and heat transfer coefficients h_o and h_i obtained for Rebrov's empirical correlation and solving the inverse IHCP problem, respectively. Fig. 8 shows the thermal history obtained with the mathematical model, which acceptably concurs with the thermal history obtained experimentally. This validates the TBC established for each of the surfaces of the specimen, confirming the assumption in terms of radiative contribution to the interior is significant and accurate, making it possible to appropriately predict the evolution of the thermal field during heating by the Joule effect.

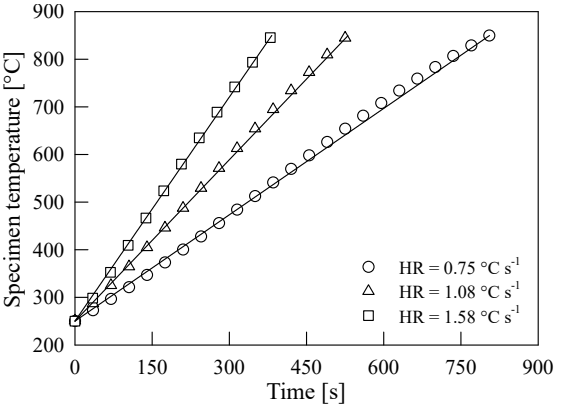

Fig. 8. Shows the experimental thermal history (symbols) and simulated thermal history (lines) for the heating rates of: 0.75 °C s^{-1}, 1.08 °C s^{-1}, and 1.58 °C s^{-1} for an AISI 304 stainless steel

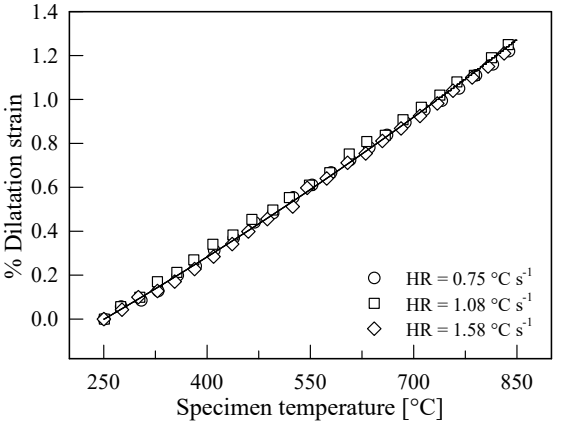

Fig. 9. *Dilation strain experimental (dots) and simulated values with the model (line) for the heating rates of: 0.75 °C s^{-1}, 1.08 °C s^{-1}, and 1.58 °C s^{-1} for AISI 304 stainless steel*

Steel dilatation measurements were used to validate the mathematical model, and Fig. 9 shows the dilation strain for different heating rates for experimental (dots) and simulated values with the model (line). The dilatation strain is referenced to the outer diameter value to a temperature of 250 °C for

each heating rate. As with the thermal history, a linear behaviour is observed where the adjustment between experimental values and those simulated with the model is acceptable. From the same figure it can be inferred that the linear thermal expansion coefficient is independent of the heating rate.

5 SENSITIVITY ANALYSIS

A sensitivity analysis of the mathematical model was performed to determine the effect of the critical input variable on the specimen's thermal history. For this the function of electrical conductivity $\sigma_e(T)$ was employed, modifying the function ±20 % and ±40 % with respect to the original value, this response was called the "medium scenario", trying to emulate a material with greater and weaker conductivity to determine its influence on the thermal history of the specimen. Likewise, the thickness of the dilatometric specimen used was referred to as the difference between the outside and the inside radii Δr. This parameter was selected due to the mass factor and its influence on thermal history, for which the outer diameter was modified from 2.9 mm and 4.1 mm, thereby obtaining different wall thicknesses for the dilatometric specimen. The other input variables such as thermophysical properties and electric current history were set in the sensitivity analysis. Fig. 10 shows the family of curves for electrical conductivity $\sigma_e(T)$ and the current history used in the sensitivity analysis.

5.1 Input Variables

Electrical conductivity is a major input variable in the model because, under the physical principal of Joule heating, the dilatometric specimen acts as electrical resistance to the circuit, so that a small change in its value is reflected as an increase or decrease of the required electric current intensity. Likewise, the thickness of the specimen delimits the heating conditions due to the amount of mass to be heated and the contact area through which the electric current circulates. Both variables were modified and analysed with regard to simulated thermal history, comparing the results with the medium scenario response. Fig. 11 shows the effects of electrical conductivity and the thickness of the specimen on simulated thermal history.

Fig. 11a shows that when using conductivity values below σ_e, the thermal response suddenly accelerates, reaching elevated temperatures in short times. In this regard, the heating rate is greater than the medium scenario rate. Later, the heating rate changes, approaching the medium scenario rate of 0.66 °C s^{-1} until a temperature of 900 °C is reached. As indicated, when reducing electrical conductivity, the resistivity of the material increases. The abrupt change observed at the beginning of the curves, with conductivity below σ_e owes to current history $I(t)$, Fig. 10b, which is the electric current history used in the medium scenario and in whole analysis scenarios. A material with greater resistivity requires less current to reach a specific temperature. However, by keeping the same current history, the material tends to heat at greater rates, as seen in this case; the model tries to maintain the restriction in regards to heating rate, stabilizing the thermal response with regards to the medium scenario response. In the opposite case, for conductivity greater than σ_e, the temperature drops below the starting temperature (350 °C), this light undercooling is more apparent when the

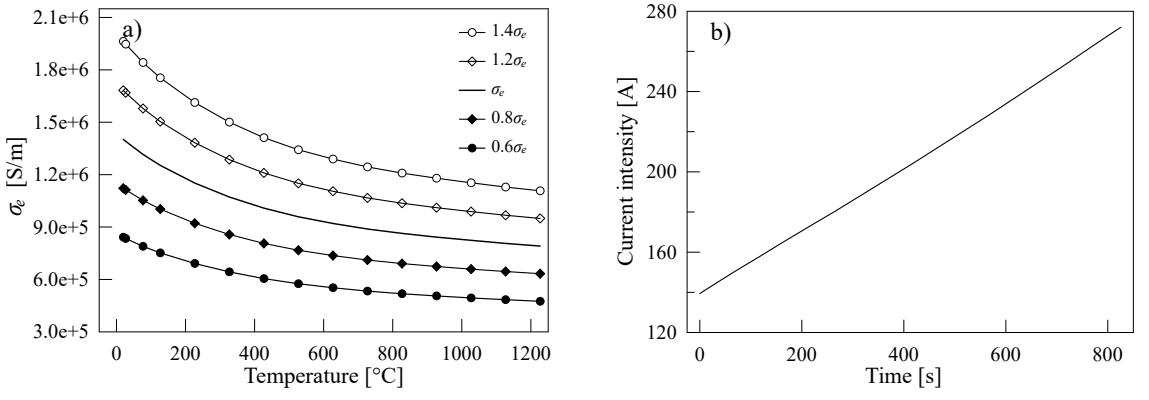

Fig. 10. *a) Electrical conductivity for an AISI 304 stainless steel as function of the temperature; the figure shows the family of curves used in sensitivity analysis, the value of the original electrical conductivity varying ±20 % and ±40 %, the solid line indicated the electrical conductivity used for the medium scenario, and b) electric current history used for sensitivity analysis*

electrical conductivity is higher, due to electrical resistivity reducing without opposing the passage of current, which is insufficient to maintain and raise the temperatures above 350 °C. Furthermore, the boundary conditions are fundamental to heating of the specimen due to the fact that the amount of heat lost by the boundaries is greater than the amount generated by the Joule heating, reducing the temperature of the specimen until the current intensity rises until reaching and raising the initial temperature. However, for the same current history, conductivity values above σ_e do not allow the temperature seen in the medium scenario to be reached, because when increasing conductivity, resistivity drops, making the system require a greater amount of current to reach the established temperature of 900 °C. In this case, when conductivity is equal to 1.4 σ_e the temperature to be reached at the same time or with the same current intensity is barely 734 °C.

In contrast, wall thickness influences the thermal response of the specimen, as shown in Fig. 11b. In this figure, thicknesses between 0.4 mm and 1.6 mm are listed, considering that the thickness of the specimen for the medium scenario is 1 mm. When specimen thickness is below 1 mm, thermal response is incredibly fast, especially when the Δr is equal to 0.4 mm, the temperature then rises rapidly to 800 °C in just 18 seconds, averaging a heating rate of 25 °C s^{-1}, well above the rate of the medium scenario rate of 0.66 °C s^{-1}. Later, the rate continuously drops to approximately 0.66 °C s^{-1} until reaching the temperature of 900 °C, the same effect can be seen for a thickness of 0.8 mm, but to a lesser degree. These changes are directly associated with the contact area. Upon reducing the area, current density increases, making the current concentrate and increasing the temperature of the specimen considerably. In contrast, when thickness increases above 1 mm, the current supply is insufficient to maintain the initial temperature of 350 °C, and consequently to increase it. In this case, the heat extracted by the surfaces of the specimen is greater than the heat generated and the temperature drops to 250 °C for a thickness of 1.6 mm. After a time, the current continues to increase, Fig. 10b, increasing the temperature of the specimen to above 350 °C. However, with the same current history, the specimen does not manage to heat up to the temperature of 900 °C like in the medium scenario. When the thickness of the specimen is greater, the density of the current is reduced, preventing the material from heating up the same way.

As has been noted, electrical conductivity and specimen thickness have a strong impact on thermal response, both variables are critical to meeting the thermal heating conditions due to the Joule effect. Therefore, both material selection and specimen dimensions are essential to adequately design a thermal cycle.

6 PREDICTIONS

Finally, the mathematical model was employed to carry out a series of predictions on a metallic alloy other than AISI 304 stainless steel, a super nickel-based Hastelloy® C-276, which is characterized for having high mechanical resistance at high temperatures. Fig. 12 shows the thermal behaviour of Hastelloy® C-276 heated by the Joule effect to a temperature of 900 °C, in Fig. 12a shows thermal response, 12b the electric current history, and 12c the percentage of dilatation strain. To predict the thermal behaviour of Hastelloy® C-276 the same heating rate used on the stainless steel

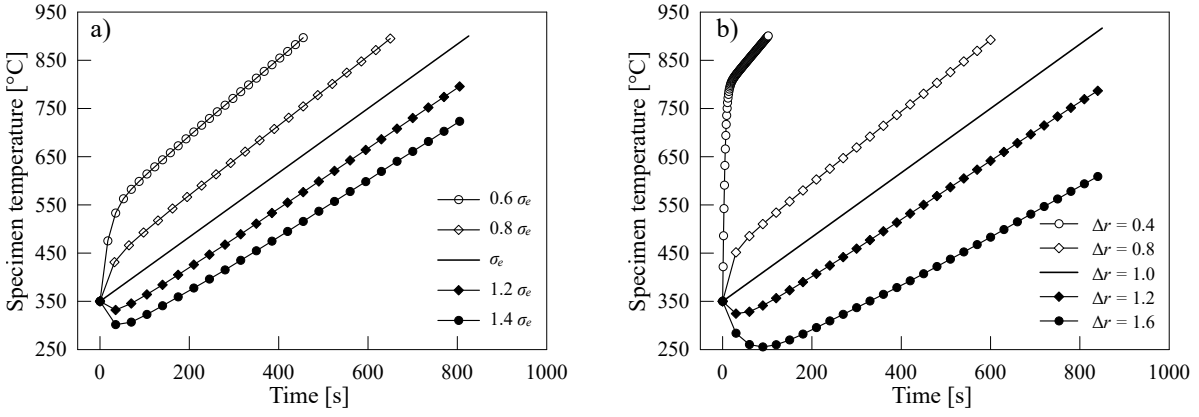

Fig. 11. *a) Simulated thermal response from the specimen using different values of electrical conductivity for an AISI 304 stainless steel, and b) simulated thermal response from the specimen using different values of thickness of the specimen for an AISI 304 stainless steel; the solid line shows the thermal response of medium scenario, the heating rate was 0.66 °C s^{-1}*

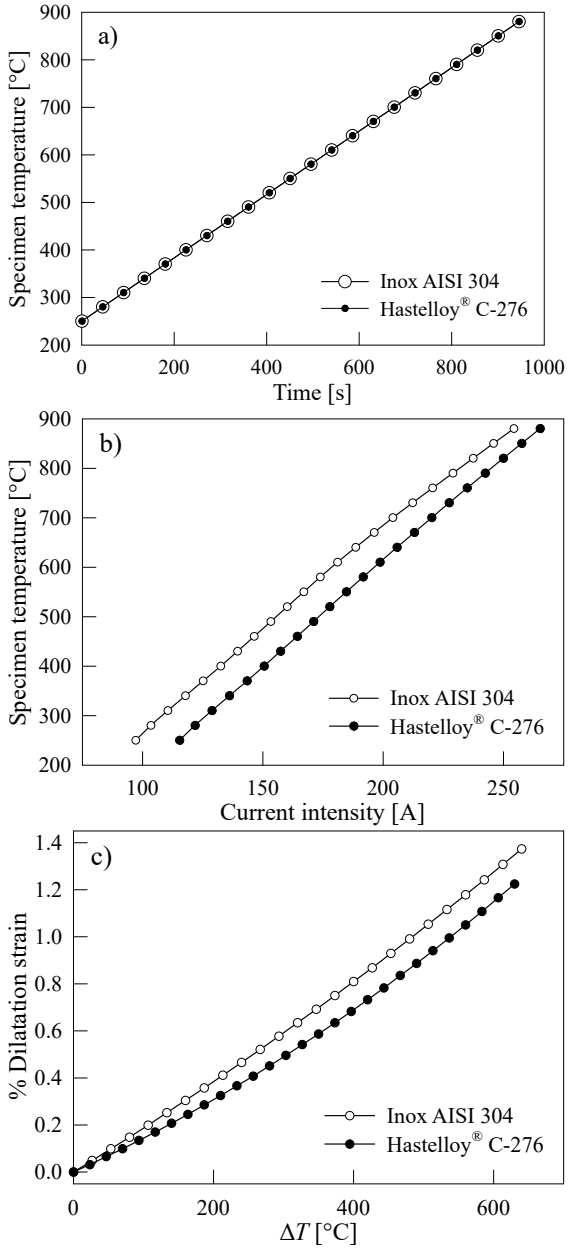

Fig. 12. *a) Prediction and comparison of thermal history, b) current history, and c) percentage of dilatation strain of an alloy base nickel Hastelloy® C 276 with regards to AISI 304 stainless steel*

(0.66 °C s^{-1}) was applied, along with similar specimen dimensions with a thickness of Δr 1 mm.

Fig. 12a shows the comparison between the thermal history of the Hastelloy and stainless steel, showing that there is no difference in thermal response for both materials, regardless of the thermophysical and electrical properties. This is due to the heating rate remaining fixed at 0.66 °C s^{-1} in both cases. The model sample has the capacity to adjust the heating rate and simultaneously calculate the electric current required to heat the specimens at a final temperature of 900 °C. Fig. 12b shows the comparison between the current histories predicted by the model, both materials initial temperatures are 250 °C. Unlike the thermal response, it can be observed that to heat a Hastelloy specimen to 900 °C requires a greater current. The behaviour is similar and mostly linear for the two materials. Finally, Fig. 12c shows the behaviour of the dilatation strain of both materials. It can be noted that the behaviour is not completely linear, which generates a curvature as the temperature rises. Although, specimens with the same thickness are considered, the response is different due to the thermal expansion coefficient. Stainless steel has greater strain by dilatation when reaching 900 °C than the Hastelloy does. These predictions are useful for estimating, establishing, and designing heating conditions for a conductor material and specifying the amount of electric current and thickness required to reach the temperature given in order to study the mechanical-electrical-thermal behaviour of the material.

7 CONCLUSIONS

Based on the results obtained it has been shown that it is possible to develop a mathematical Joule heating model for a dilatometric specimen, by estimating the thermal history, electric current history, and percentage of dilatation strain for a hollow cylindrical specimen with thermophysical and electrical properties, depending on the temperature. It was also shown that it is possible to estimate the thermal boundary conditions using an empirical correlation and the solution to the IHCP to determine the overall heat transfer coefficient in the inner and outer surfaces of the specimen, taking into account the phenomena of convection and radiation. Likewise, the model was satisfactorily validated by comparing it with the thermal history and percentage of dilatation strain by experimental with simulated responses with the mathematical model, to data acquired at a different heating rate. Additionally, a sensitivity analysis was conducted to determine the effect of the critical variables of the model, such as electrical conductivity and the thickness of the specimen. The effect of electrical conductivity was observed on the thermal history, leading to the conclusion that the increase in conductivity hinders heating because the electrical resistance of the system decreases. In contrast, the thickness of the specimen has a strong influence on the heating rate, because when the thickness is decreased, the current density increases to rapidly

achieve rates higher than those established. Finally, the mechanical-electrical-thermal behaviour of the nickel-based Hastelloy® C 276 was estimated, with electric properties similar to stainless steel and it was shown in the results that they were as expected, that is, a lesser temperature in the middle section and dilatation of the specimen for the same value of electric current supplied to the AISI 304 stainless steel specimen, due to the fact that Hastelloy has lower conductivity and linear thermal expansion than that of stainless steel.

8 ACKNOWLEDGEMENTS

M. Herrejón-Escutia would like to thank the National Council of Science and Technology of Mexico (CONACYT) for the scholarship (No. 267206) received for his doctoral studies. The authors are grateful to SEP-CONACYT and PRODEP for the support received through grants CB-256843 and UNISTMO-PTC-108, respectively.

9 REFERENCES

[1] García de Andrés, C., Caballero, F.G.., Capdevila, C., Álvarez, L.F. (2002). Application of dilatometric analysis to the study of solid–solid phase transformations in steels. *Materials Characterization*, vol. 48, no. 1, p. 101-111, **DOI:10.1016/S1044-5803(02)00259-0**.

[2] Moravčík, R., Štefániková, M., Čička, R., Čaplovič, Ľ., Kocúrová, K., Šturm, R. (2012). Phase transformations in high alloy cold work tool steel. *Strojniški vestnik - Journal of Mechanical Engineering*, vol. 58, no. 12, p. 709-715, **DOI:10.5545/sv-jme.2012.531**.

[3] Oliveira, F.L.G., Andrade, M.S., Cota, A.B. (2007). Kinetics of austenite formation during continuous heating in a low carbon steel. *Materials Characterization*, vol. 58, no. 3, p. 256-261, **DOI:10.1016/j.matchar.2006.04.027**.

[4] López-Martínez, E., Vázquez-Gómez, O., Vergara-Hernández, H.J., Campillo, B. (2015). Effect of initial microstructure on austenite formation kinetics in high-strength experimental microalloyed steels. *International Journal of Minerals, Metallurgy, and Materials*, vol. 22, no. 12, p. 1304-1312, **DOI:10.1007/s12613-015-1198-4**.

[5] Vázquez-Gómez, O., Barrera-Godínez, J.A., Hernández-Morales, B., Vergara-Hernández, H.J., López-Martínez, E. (2012). Mathematical model of thermal and microstructural evolution during austempering of ductile iron. *Materials Performance and Characterization*, vol. 1, no. 1, p. 1-14, **DOI:10.1520/MPC104384**.

[6] López-Martínez, E., Hernández-Morales, J.B., Solorio-Díaz, G., Vergara-Hernández, H.J., Vázquez-Gómez, O., Garnica-González, P. (2013). Prediction of hardness profiles in medium and low carbon steel jominy probes. *Mexican Journal of Chemical Engineering*, vol. 12, no. 3, p. 606-616. (in Spanish)

[7] Mohanty, R.R., Girina, O.A., Fonstein, N.M. (2011). Effect of heating rate on the austenite formation in low-carbon high-strength steels annealed in the intercritical region. *Metallurgical and Materials Transactions A*, vol. 42, p. 3680-3690, **DOI:10.1007/s11661-011-0753-5**.

[8] Vázquez-Gómez, O., Barrera-Godínez J.A., Vergara-Hernández H.J. (2015). Kinetic study of austenite formation during continuous heating of unalloyed ductile iron. *International Journal of Minerals, Metallurgy, and Materials*, vol. 22, no. 1, p. 27-31, **DOI:10.1007/s12613-015-1039-5**.

[9] Herrejón-Escutia, M., Arreola-Villa, S.A., Solorio-Díaz, G., Vázquez-Gómez, O. (2016). Experimental determination of the electrical resistivity of a nickel base alloy during continuous heating by Joule effect, Investigative *Compendium of Academia Journals Celaya*, p. 2856-2860. (in Spanish)

[10] Holman, J.P. (1986). *Heat Transfer*. McGraw-Hill, Singapore.

[11] Gere, J.M., Goodno, B.J. (2013). Mechanics of Materials. Cengage Learning, Toronto.

[12] Dieter, G.E. (1986). *Mechanical Metallurgy*. McGraw-Hill, New York.

[13] Malek, A. (2011). Applications of nonstandard finite difference methods to nonlinear heat transfer problems, Belmiloudi, A. (ed.), Heat Transfer-Mathematical Modelling. Numerical Methods and Information Technology. *InTech*, p. 185-208, **DOI:10.5772/14439**.

[14] Boetcher, S.K.S. (2014). Natural Convection from Circular Cylinders. Springer, Cham, **DOI:10.1007/978-3-319-08132-8**.

[15] Poirier, G.H., Geiger, D.R. (2009). *Transport Phenomena in Materials Processing*. TSM Minerals Metals Materials, Pennsylvania.

[16] Cengel, Y.A. (2003). *Heat Transfer a Practical Approach*. McGraw-Hill, New York.

[17] Narazaki, M., Kogawara, M., Ming, Q., Watanabe, Y. (2009). Measurement and database construction of heat transfer coefficients of gas quenching. *Strojniški vestnik - Journal of Mechanical Engineering*, vol. 55, no. 3, p. 167-173.

[18] Özisik, M.N., Orlande H.R.B. (2000). *Inverse Heat Transfer: Fundamentals and Applications*. Taylor & Francis, New York.

[19] Daw, J.E., Rempe, J.L., Knudson, D.L. (2009). *Thermal properties of structural materials found in light water reactor vessels*. Idaho National Laboratory (INL), Indaho, **DOI:10.2172/974795**.

[20] Ho, C.Y., Chu, T.K. (1977). *Electrical resistivity and thermal conductivity of nine selected AISI stainless steels*. Center for Information and Numerical Data Analysis and Synthesis, Indiana.

[21] Beck, J.V. (1970). Nonlinear estimation applied to the nonlinear inverse heat conduction problem. *International Journal of Heat and Mass Transfer*, vol. 13, no. 4, p. 703-716, **DOI:10.1016/0017-9310(70)90044-X**.

[22] Reinhardt, H.-J., Hào, D.N. (1994). Sequential approximation to nonlinear inverse heat conduction problems. *Mathematical and Computer Modelling*, vol. 20, no. 10-11, p. 189-200, **DOI:10.1016/0895-7177(94)90177-5**.

[23] Hawbolt, E.B., Chau, B., Brimacombe, J.K. (1983). Kinetics of austenite-pearlite transformation in eutectoid carbon steel. *Metallurgical Transactions A*, vol. 14, no. 9, p. 1803-1815, **DOI:10.1007/BF02645550**.

Vsebina

Strojniški vestnik - Journal of Mechanical Engineering
letnik 63, (2017), številka 9
Ljubljana, september 2017
ISSN 0039-2480

Izhaja mesečno

Razširjeni povzetki (extended abstracts)

Strojniški vestnik - Journal of Mechanical Engineering 63(2017)9, SI 71

Prejeto v recenzijo: 2017-05-26
Prejeto popravljeno: 2017-08-17
Odobreno za objavo: 2017-08-24

Fenomen tečenja in ciklična plastifikacija konzolnega nosilca

Andrej Žerovnik* – Ivan Prebil – Robert Kunc
Univerza v Ljubljani, Fakulteta za strojništvo, Slovenija

Fenomen tečenja je na napetostno-deformacijskih krivuljah enoosno obremenjenih preizkušancev viden ob prvem prehodu iz elastičnega v elasto-plastično področje kot ostra konica (točka tečenja), kateri sledijo padec napetosti, napetostna planota (t. i. Lüders-ova planota) ter nadaljnje utrjevanje. Padec napetosti in napetostna planota sta posledici hitrega večanja števila mobilnih dislokacij. Posledica takšnega odziva je nehomogena plastična deformacija materiala tekom tvorjenja napetostne planote. Pojav je značilen za železo, nizkolegirana jekla, titanove in aluminijeve zlitine ter nekatere druge kovinske zlitine, kot tudi za polimere, kompozite in laminate ter nekatere kamenine.

Fenomen tečenja je bil v povezavi z enoosnim obremenjevanjem podrobneje raziskan že v preteklosti. Za popis fenomena tečenja so bile izpeljane različne formulacije konstitutivnih modelov, ki pa so se v večji meri osredotočale na monotone obremenitvene primere. Večina obstoječih konstitutivnih modelov za popis ciklične plastifikacije omenjenega fenomena ne upošteva, dejanski vpliv upoštevanja fenomena tečenja na ciklično plastifikacijo pa do sedaj ni bil poznan. Avtorji prispevka so v preteklosti predstavili konstitutivni model ciklične plastifikacije, ki vsebuje tudi popis fenomena tečenja.

Z namenom verifikacije razvitega konstitutivnega modela in prikaza doprinosa enačb popisa fenomena tečenja na rezultate numeričnih simulacij ciklične plastifikacije je v prispevku predstavljena analiza ciklične plastifikacije konzolnega nosilca. Nosilec je izdelan iz materiala EN 42 CrMo 4 v normaliziranem stanju (184 HV), ki izkazuje ciklično utrjevanje, in v poboljšanem stanju (296 HV), ki izkazuje ciklično mehčanje. Analiza zajema primerjavo numeričnih simulacij z rezultati eksperimentalnega dela. Zaradi dolgih računskih časov je primerjava omejena na prvih 100 obremenitvenih ciklov.

Eksperimentalno delo je izvedeno na enoosnem dinamičnem preizkuševališču Instron 8802, za ustrezno vpetje konzolnega nosilca pa je izdelano posebno vpetje, ki zagotavlja ustrezno togost. Konzolni nosilci so obremenjeni z različnimi robnimi pogoji (različne amplitude pomika), tekom preizkusa pa so bili opazovani sila, pomik ter deformacije na mestu največjih pričakovanih deformacij konzolnega nosilca. Za merjenje deformacij je uporabljen optični merilni sistem GOM Aramis 5M, medtem ko sta sila in pomik merjena s pripadajočo opremo preizkuševališča.

Za izvedbo numeričnih simulacij po metodi končnih elementov je generirana in uporabljena simbolno-numerična koda končnega elementa, simulacije pa so izvedene za primer konstitutivnega modela z upoštevanjem enačb popisa fenomena tečenja in brez njih. Na podlagi predhodnih meritev so določeni parametri konstitutivnega modela za obe stanji materiala.

Primerjava sile konzolnega nosilca v odvisnosti od pomika in števila ciklov kaže na dobro ujemanje rezultatov eksperimentalnega dela z rezultati numeričnih simulacij v primeru upoštevanja fenomena tečenja, medtem ko v primeru neupoštevanja fenomena tečenja rezultati izraziteje odstopajo. Podobne ugotovitve glede doprinosa popisa fenomena tečenja potrjuje tudi primerjava deformacijskih polj konzolnega nosilca, kjer je izrazita razlika vidna predvsem v začetni fazi obremenjevanja, medtem ko v nadaljevanju nekoliko izzveni. Za samo razumevanje in prikaz doprinosa popisa fenomena tečenja v konstitutivnih modelih so prikazane največje primerjalne napetosti (Von Mises). Primerjava posameznih rezultatov prikazuje popolnoma drugačen potek primerjalnih napetosti v primeru upoštevanja fenomena tečenja in kaže na to, da je v primeru upoštevanja fenomena tečenja cona plastične deformacije manjša, iz česar je možno sklepati, da je ciklična plastifikacija v najbolj obremenjenem delu izrazitejša. Analiziran je tudi vpliv cikličnega utrjevanja/mehčanja na ciklično plastifikacijo.

Analiza sprememb posameznih parametrov konstitutivnega modela, prikazanih v delu, omogoča razumevanje vpliva fenomena tečenja na ciklično plastifikacijo konzolnega nosilca. Predstavljeni rezultati potrjujejo ustreznost in smiselnost popisa fenomena tečenja v konstitutivnem modelu ciklične plastifikacije.

Ključne besede: fenomen tečenja, ciklična plastifikacija, mehanski preizkusi, MKE-simulacije, konstitutivni model, mehanika kontinuuma

*Naslov avtorja za dopisovanje: Univerza v Ljubljani, Fakulteta za strojništvo, Aškerčeva 6, 1000 Ljubljana, Slovenija, andrej.zerovnik@fs.uni-lj.si

Strojniški vestnik - Journal of Mechanical Engineering 63(2017)9, SI 72

Prejeto v recenzijo: 2017-03-03
Prejeto popravljeno: 2017-05-09
Odobreno za objavo: 2017-06-16

Uporaba prilagojenega modela sil za natančno struženje različnih kovinskih materialov

Richárd Horváth* – Judit Lukács
Univerza v Óbudi, Fakulteta za strojništvo in varnostni inženiring Donát Bánki, Madžarska

Rezalne sile so zelo pomembne, saj vplivajo na obremenitve stroja, pri natančnem struženju pa lahko povzročijo deformacije tankih oz. vitkih obdelovancev. Nastale sile niso odvisne samo od lastnosti materiala (trdota, natezna trdnost itd.) in od rezalnih parametrov (v_c - rezalna hitrost, m/min; f – podajanje, mm; a_p – globina reza, mm), temveč tudi od geometrije rezalnega roba orodja, ki opredeljuje geometrijo odrezka (debelino in širino).

Članek obravnava uporabo prilagojenega modela sil pri tehnologiji natančnega struženja, kjer ima pri oblikovanju odrezkov glavno vlogo polmer vrha orodja. Meje parametrov natančnega struženja, znotraj katerega so bile opravljene preiskave, so bile: a_p = 0,25 do 0,7 mm; f = 0,03 do 0,15 mm.

Obravnavani so bili trije različni materiali, ki so razširjeni v množični proizvodnji (nelegirano jeklo C45, avstenitno nerjavno jeklo KO36 in evtektična aluminijeva zlitina za tlačno litje AS12). Izmerjene so bile komponente rezalne sile v treh smereh (F_c – glavna rezalna sila, N; F_f – podajalna sila, N; F_p – potisna sila, N) in specifične rezalne sile. Običajni geometrijski parametri (h – debelina odrezka, mm in b – širina odrezka, mm) niso primerni za karakterizacijo preseka nedeformiranega odrezka pri natančnem struženju, saj pri oblikovanju odrezka deluje predvsem zaokroženi vrh. Zato sta bila uvedena nova parametra geometrije: h_{eq} – ekvivalentna debelina odrezka, mm, in l_{eff} – efektivna dolžina roba orodja, mm.

Za natančno struženje so bile uvedene nove vrednosti specifične rezalne sile ($k_{1,0.1}$, N/mm2), s pomočjo katerih je bil zasnovan nov model sile na podlagi novih teoretičnih parametrov preseka nedeformiranega odrezka za vse tri materiale. Novi model sile s teoretičnimi parametri preseka nedeformiranega odrezka (h_{eq} in l_{eff}) pri vseh preiskovanih materialih omogoča ocenjevanje komponent prostorskih sil (F_c, F_f, F_p).

Izkazalo se je, da so specifične rezalne sile pri vseh treh komponentah močno odvisne od vrednosti l_{eff} in niso samo funkcija h_{eq} (učinek je najmanj izražen pri k_c in najbolj izražen pri k_p). V model specifičnih rezalnih sil je zato treba vključiti oba geometrijska parametra kljub Kienzle-Victorjevi enačbi (v primeru večjega preseka odrezka). Napake novega modela sil sledijo Gaussovi porazdelitvi z majhno vrednostjo standardne deviacije pri vseh materialih. Model, ki je prilagojen silam pri natančnem struženju, je mogoče uporabiti tudi pri materialih s tehnološko bistveno drugačnimi lastnostmi.

Uporabnost enačb tako ni odvisna od materiala obdelovanca in modeli so primerni za ustrezno natančno ocenjevanje komponent rezalne sile v procesu načrtovanja tehnologije.

Ključne besede: natančno struženje, model sil, merjenje sil, specifična rezalna sila, nelegirano jeklo, avstenitno nerjavno jeklo, evtektična aluminijeva zlitina za tlačno litje

*Naslov avtorja za dopisovanje: Univerza v Óbudi, Fakulteta za strojništvo in varnostni inženiring Donát Bánki, Népszinház str. 8., Budimpešta, 1081 Madžarska, horvath.richard@bgk.uni-obuda.hu

Strojniški vestnik - Journal of Mechanical Engineering 63(2017)9, SI 73

Prejeto v recenzijo: 2016-12-15
Prejeto popravljeno: 2017-06-02
Odobreno za objavo: 2017-07-10

Vpliv razmerja med debelino in premerom luknje matrice na proces štancanja pločevine

Kaan Emre Engin[1,*] – Omer Eyercioglu[2]

[1]Univerza v Adiyamanu, Tehniška fakulteta, Oddelek za avtomobilsko tehniko, Turčija
[2]Univerza v Gaziantepu, Tehniška fakulteta, Oddelek za strojništvo, Turčija

Postopek štancanja je zelo razširjen v proizvodnji pločevinastih izdelkov. Učinkovitost procesa je odvisna od ravnovesja med kakovostjo površine štancanih izdelkov in prihranka energije med procesom. Čeprav je štancanje na prvi pogled morda preprost postopek, pa je ta proces odvisen od mnogih parametrov.

Splošni parametri procesa so rezilna reža, vrsta in debelina materiala, rezalna hitrost, geometrija orodja, obraba orodja in kinematika stiskalnice. Vpliv različnih parametrov procesa na kakovost površine in energijsko učinkovitost je dobro preučen, manjkajo pa podatki o vplivu razmerja med debelino in premerom orodja na kakovost površine in energijsko učinkovitost.

Namen predstavljene študije je raziskava vpliva omenjenega razmerja na obremenitve pri štancanju, potrebno energijo za rezanje in kakovost površine štancanih delov (s preiskavo kotov napredovanja razpok in porazdelitve con) pri različnih rezilnih režah.

Opravljeni sta bili eksperimentalna študija in študija po metodi končnih elementov. Uporabljena so bila štiri različna razmerja med debelino in premerom matrice (t/D_m = 1/5, t/D_m = 1/10, t/D_m = 1/30 in t/D_m = 1/50) ter pet različnih rezilnih rež (1 %, 3 %, 5 %, 10 % in 20 % debeline) za štancanje 2 mm debelih okroglih delov iz nerjavnega jekla AISI 304. Za eksperimentalno študijo je bil izdelan poseben komplet orodij z izmenljivimi pestiči in matricami iz jekel AISI 4140 in St37, uporabljena pa je bila hidravlična stiskalnica s kapaciteto 300 kN. Hitrost prebijala med štancanjem je bila konstantna, t.j. 0,01 m/s. Za študijo po metodi končnih elementov je bil uporabljen paket Deform-2D. Privzet je bil osnosimetričen proces štancanja in za simulacijo parametrov procesa je bil uporabljen 2D-model. Za izračune je tako zadostoval samo polovični model orodja. Uporabljen je bil normaliziran kriterij loma po Cockroftu in Lathamu, za modeliranje pa so bili uporabljeni izoparametrični kvadratni elementi.

Ugotovljena je bila povezava med energijo za štancanje, koti napredovanja razpok in porazdelitvijo con. Pogoji rezanja so idealni tedaj, ko je obremenitev prebijala najmanjša za prihranek energije in je kakovost izdelka zadovoljiva, tako da niso potrebne dodelave površinskih napak. To pomeni, da mora globina strižne cone (vtiskovanja) znašati vsaj eno tretjino debeline pločevine in ne sme nastajati srh. Idealni pogoji za rezanje so doseženi, ko se kot realne smeri napredovanja razpok (β) ujema s kotom idealne smeri napredovanja razpok (θ). Realna smer napredovanja razpok je dejanska smer napredovanja po površini traku, idealna smer pa predstavlja želeno pot napredovanja razpok proti rezalnim robovom pestiča in spodnje matrice. Če je vrednost β blizu vrednosti θ, bo površina bolj gladka. Idealna velikost rezilne reže za AISI 304, s katero je mogoče doseči prihranek energije in dobro kakovost površine, je 3 % za t/D_m = 1/5 in t/D_m = 1/10, ter 5 % za t/D_m = 1/30 in t/D_m = 1/50.

Iz rezultatov sledi sklep, da idealna velikost rezilne reže ni odvisna le od debeline materiala, temveč tudi od razmerja med debelino in premerom izdelka. S povečanjem razmerja t/D_m se povečata tudi obremenitev pestiča in globina giba, s tem pa rezalna energija. Ko se povečuje obseg materiala z enako debelino, se nekoliko poveča tudi vrednost rezilne reže. Rezultati analize po MKE se dobro ujemajo z rezultati eksperimentov. Študija je pomembna, ker zapolnjuje vrzel v literaturi o vplivih razmerja med debelino in premerom luknje matrice na proces štancanja.

Ključne besede: proces štancanja, parametri štancanja, strižna cona, rezilna reža, rezalna energija, obremenitve pri štancanju, razmerje med debelino in premerom

*Naslov avtorja za dopisovanje: Adiyaman University, Altinsehir Mah., No:13, Adiyaman, Turčija, kengin@adiyaman.edu.tr

Strojniški vestnik - Journal of Mechanical Engineering 63(2017)9, SI 74

Prejeto v recenzijo:2017-03-09
Prejeto popravljeno: 2017-06-13
Odobreno za objavo: 2017-06-29

Vpliv parametrov procesa na mikrostrukturo in mehanske lastnosti aluminijeve zlitine AA5182, varjene z vlakenskim laserjem

Celalettin Yuce[1,*] – Mumin Tutar[1] – Fatih Karpat[1] – Nurettin Yavuz[1] – Gökhan Tekin[2]

[1] Univerza v Uludagu, Oddelek za strojništvo, Bursa, Turčija
[2] Coskunöz A.Ş., Turčija

Lasersko varjenje aluminijevih zlitin je pomembna industrijska tehnologija. S svojo visoko hitrostjo, dostopom samo z ene strani, odsotnostjo neposrednega stika med orodjem in obdelovancem ter preprosto avtomatizacijo je idealna tehnologija za montažo pri proizvodnji avtomobilskih karoserij. V primerjavi s konvencionalnimi varilnimi postopki ima manjši toplotno vplivani pas, s čimer se zmanjšajo težave metalurške narave. Kljub številnim prednostim aluminijevih zlitin pa se pri njihovem varjenju srečujemo tudi z določenimi težavami. Širok razpon temperatur pri uparjanju in strjevanju lahko povzroči nestabilnost parnice, prebojne luknje, poroznost in različne metalurške napake, kot so npr. vroče razpoke. Težavo pri teh zlitinah predstavlja tudi izguba legirnih elementov in slabo sprejemanje energije laserja. Težave pri varjenju aluminijevih zlitin in mehanske lastnosti spojev so neposredno odvisne od parametrov procesa.

Lasersko varjenje v avtomobilski industriji je predmet številnih eksperimentalnih in teoretičnih študij, še vedno pa manjkajo podatki o vplivu parametrov procesa varjenja z vlakenskim laserjem na mikrostrukturo in mehanske lastnosti materialov z veliko toplotno prevodnostjo ali z volatilnimi kemijskimi elementi, kot je serija 5xxx. Za te zlitine je običajno na voljo le ozek razpon ustreznih varilnih parametrov, ki ga je tudi težko poiskati, saj se parnica in zvarna kopel med procesom varjenja močno spreminjata. Aluminijeve zlitine imajo v primerjavi z jeklom večjo začetno odbojnost za laserski žarek in toplotno prevodnost, zato je za varjenje s parnico potrebna večja gostota moči kot pri jeklu. Moč laserja, velikost točke in hitrost varjenja so pomembne spremenljivke varilnega procesa. V predstavljeni študiji je bilo opravljeno lasersko varjenje prekrivnega spoja delov iz aluminijeve zlitine AA55182 z namenom preučitve vplivov parametrov varilnega procesa na mehanske in mikrostrukturne lastnosti spojev. V eksperimentih so bili obravnavani parametri procesa moč laserja, varilna hitrost in položaj gorišča. Varivost je bila ovrednotena s preiskavo mikrostrukture in mikrotrdote prereza, mehanske lastnosti pa z nateznim preizkusom.

Na podlagi rezultatov eksperimenta je bila opravljena analiza odvisnosti med natezno trdnostjo, globino penetracije in širino zvarnega šiva ter parametri procesa. Ugotovljeno je bilo, da je zaradi čezmernega vnosa toplote prišlo do prevelike penetracije in izparevanja varka, zato se je zmanjšala natezna trdnost spojev. Nasprotno je nezadosten vnos toplote povezan z zmanjšanjem globine penetracije in s tem natezne trdnosti. Zato je nujna skrbna izbira vnosa toplote na enoto dolžine, ki je odvisna od moči laserja in hitrosti varjenja. Eksperimenti so tudi pokazali, da položaj gorišča vpliva na širino vara in na globino penetracije. Največja natezna trdnost je bila ugotovljena pri moči laserja 2750 W, varilni hitrosti 20 mm/s in položaju gorišča 100 mm. Preučena je bila mikrostruktura različnih delov optimalnega vzorca. Mikrostruktura cone spajanja je stebričasta dendritna ter jo je mogoče razdeliti na notranjo in zunanjo cono. Toplotno vplivani pas velikosti nekaj zrn je bil najden v bližini linije spoja. V coni spajanja so bile ugotovljene manjše napake v obliki izločenega prenasičenega vodika in interdendritnih lunkerjev. Preiskava mikrotrdote je pokazala, da se je v coni spajanja zaradi izboljšane mikrostrukture nekoliko povečala trdota. Analiza EDS v coni spajanja je pokazala skoraj 12-odstotno izgubo magnezija glede na osnovni material, v preiskavi SEM pa so bili odkriti delci z železom v coni spajanja.

Ključne besede: varjenje z vlakenskim laserjem, aluminijeve zlitine, karakterizacija mehanskih lastnosti, analiza mikrostrukture

*Naslov avtorja za dopisovanje: Univerza v Uludagu, Oddelek za strojništvo, Bursa, Turčija, cyuce@uludag.edu.tr

Strojniški vestnik - Journal of Mechanical Engineering 63(2017)9, SI 75

Prejeto v recenzijo: 2016-12-19
Prejeto popravljeno: 2017-05-23
Odobreno za objavo: 2017-07-03

Adaptivna robustna regulacija razreda momentnih motorjev z nasičenim vhodom na podlagi nevronskih mrež

Lei Liu – Jian Hu* – Yuangang Wang – Zhiwei Xie
Znanstveno-tehniška univerza v Nanjingu, Šola za strojništvo, Kitajska

Servosistemi z momentnimi motorji so razširjeni v različnih industrijskih aplikacijah. Zaradi omejitev aktuatorjev pogosto nastopi nasičenje vhoda, ki lahko negativno vpliva na regulacijo sistema. Zato obstaja potreba po krmilniku, ki bi zmanjšal vpliv nasičenja vhoda na regulacijo sistema.

Za razrešitev problema nasičenja vhoda sistema servomotorja je zasnovan opazovalec, ki ocenjuje vrednost nasičenja za uporabo v členu usmerjene kompenzacije predlaganega krmilnika. Na ta način je mogoče zmanjšati vpliv nasičenja vhoda.

Zasnovan je opazovalec na podlagi nevronske mreže z eno skrito plastjo za ocenjevanje vrednosti nasičenja vhoda, ki bo pozneje kompenzirano v krmilniku. Uvedena sta tudi adaptivni zakon za ocenjevanje neznanih parametrov in nelinearen robustni člen za odpravo časovno spremenljivih motenj. Tema tega članka je visokonatančno krmiljenje sistema pogonsko-pozicionirnega servomotorja.

Nevronska mreža z eno skrito plastjo lahko zahvaljujoč svoje sposobnosti samoučenja ocenjuje vrednost nasičenja vhoda, napaka ocene pa je omejena. Adaptivni zakon zmanjšuje vpliv negotovosti parametrov sistema, nelinearni robustni členi pa odpravijo časovno spremenljive motnje v sistemu ter izboljšajo njegovo robustnost. Natančnost sledenja motornega pogonsko-pozicionirnega sistema se lahko tako s kombinacijo vseh metod občutno izboljša.

V sistemu servomotorja je veliko nelinearnih dejavnikov, kot so nasičenje vhoda, časovni zamik, trenje, nezveznosti ob spremembi smeri gibanja itd. V tem članku je prikazana samo ocena in kompenzacija nasičenja vhoda. Čeprav se že s tem izboljša natančnost regulacije sistema, pa ni mogoče zmanjšati vpliva drugih nelinearnih dejavnikov v sistemu. Nevronska mreža z eno skrito plastjo omogoča samo lokalno, ne pa globalne aproksimacije. Ker je vrednost nasičenja vhoda globalna, nevronska mreža z eno skrito plastjo ne zadostuje. V prihodnje bo treba vključiti in kompenzirati še več nelinearnih faktorjev, zasnovati pa bo treba tudi učinkovitejšega opazovalca teh faktorjev za izboljšanje natančnosti regulacije sistema servomotorja.

V članku je na podlagi njihove sposobnosti univerzalne aproksimacije zasnovana linearizirana nevronska mreža z eno skrito plastjo, ki omogoča aproksimacijo saturacije vhodov, ki je pozneje učinkovito kompenzirana v krmilniku. Uporabljena je metoda adaptivne robustne regulacije za izboljšanje natančnosti sledenja pogonsko-pozicionirnih sistemov, ki jih poganjajo momentni motorji z nasičenim vhodom. Metoda omogoča celovito obdelavo nasičenja vhoda, negotovosti parametrov in motenj v sistemu. Učinkovitost regulacije je zato večja kot pri drugih krmilnikih.

Ključne besede: momentni motor, nasičenje vhoda, adaptivna robustna regulacija, nevronska mreža, motnja

*Naslov avtorja za dopisovanje: Znanstveno-tehniška univerza v Nanjingu, Šola za strojništvo, No.200, Xiaolingwei, Nanjing, Kitajska, hujian_njust@163.com

Strojniški vestnik - Journal of Mechanical Engineering 63(2017)9, SI 76

Prejeto v recenzijo: 2017-04-22
Prejeto popravljeno: 2017-06-16
Odobreno za objavo: 2017-07-14

Vpliv hrapavosti na izkoristek centrifugalnih črpalk

Andrej Lipej[1] – Simon Muhič[1,*] – Duško Mitruševski[2]
[1] Fakulteta za tehnologije in sisteme, Slovenija
[2] SM Črpalke, Slovenija

Industrijski razvoj obsega veliko število novih energetskih strojev, pri katerih je izkoristek zelo pomembna karakteristika energijskih pretvorb. V procesu razvoja se uporabljajo številne teoretične, eksperimentalne in numerične metode. Pri energetskih strojih je ena od pomembnejših metod numerična dinamika tekočin (Computational Fluid Dynamics, CFD). Za doseganje točnih rezultatov je pomembno natančno definirati geometrijo, ki jo želimo analizirati, uporabiti primeren matematični model in kakovostno računsko mrežo ter zagotoviti realne robne pogoje. Običajno je zelo pomembna izbira ustreznega turbulentnega modela. V večini CFD analiz se upošteva samo hidravlično gladke stene, brez upoštevanja hrapavosti površin. Poleg vseh zgoraj naštetih vplivnih veličin pa je prav hrapavost eden od pomembnih vzrokov napak pri numeričnih analizah.

Črpalke so zelo pomembni energetski stroji, ki zaradi velikega števila strojev v obratovanju rabijo ogromno količino električne energije. Zato je pomembno posvetiti veliko raziskovalnega časa razvoju črpalk, ki posledično obratujejo z zelo visokim izkoristkom.

Tok tekočin ob hrapavih površinah je popisan teoretično zelo dobro. Na omenjenem področju lahko najdemo veliko raziskovalnih rezultatov in druge literature za preproste geometrijske oblike. Za poljubne prostorske geometrije pa je vedno potrebno uporabiti eno izmed numeričnih metod.

Pri CFD analizah, kjer želimo upoštevati hrapavost površin, je možno izvesti numerične analize na dva načina. V prvem primeru lahko generiramo natančno geometrijo hrapave površine, kar vodi do zelo gostih računskih mrež in posledično do dolgih računskih časov, kar ni primerno za industrijske aplikacije. Druga metoda ni tako računsko zahtevna, saj lahko uporabimo parametre, ki nam definirajo hrapavost površine.

V članku je predstavljena analiza vpliva koeficienta ‘sand grain equivalent’, ki predstavlja hrapavost površin, na izgube v centrifugalnih črpalkah. V literaturi ni na voljo veliko rezultatov raziskav s tega področja. Odločili smo se analizirati vpliv hrapavosti pri numeričnih analizah na natančnost napovedi izgub v centrifugalnih črpalkah. Raziskava je bila osredotočena na vpliv velikosti računske mreže v bližini stene.

V prvem delu članka je predstavljen vpliv brezdimenzijskega parametra y^+ na natančnost numeričnih analiz s primerjavami teoretičnih in numeričnih rezultatov. Teoretične analize predstavljajo tok ob ravni plošči in v cevi. Predstavljeni so rezultati, ki pokažejo veliko odstopanje med numeričnimi in teoretičnimi rezultati, če je uporabljena premajhna vrednost y^+ ($y^+<5$). Pravilna uporaba parametra y^+ je pomembna zaradi povečanja strižnih napetosti zaradi hrapavosti površin.

Drugi del članka obravnava numerično analizo in napoved energijskih karakteristik centrifugalnih črpalk z uporabo nestacionarnih numeričnih analiz za različne vrednosti hrapavosti. Iz rezultatov je razvidno, da vpliv hrapavosti na izkoristek ni zanemarljiv in ga je potrebno upoštevati, če hočemo dobiti natančne rezultate. Glavni problem predstavljene analize je v natančni določitvi parametra ‘sand grain equivalent’ glede na realno hrapavost površin in uporabi primerne velikosti parametra y^+ za različne obratovalne pogoje, kjer se spreminja pretok skozi črpalko.

Končni rezultati predstavljajo primerjavo numeričnih rezultatov energijskih karakteristik črpalke z rezultati meritev, kjer je bila v prvem primeru pri numeričnih analizah upoštevana hrapavost sten in v drugem primeru brez upoštevanja hrapavosti. Rezultati z upoštevanjem hrapavosti se bistveno bolje ujemajo z rezultati meritev.
Ključne besede: črpalka, numerična dinamika tekočin, hrapavost, turbulenca

*Naslov avtorja za dopisovanje: Fakulteta za tehnologije in sisteme, Na Loko 2, Novo mesto, Slovenija, simon.muhic@fts-nm.si

Strojniški vestnik - Journal of Mechanical Engineering 63(2017)9, SI 77

Prejeto v recenzijo: 2017-01-11
Prejeto popravljeno: 2017-05-04
Odobreno za objavo: 2017-06-16

Elektrotermomehanska analiza Joulovega segrevanja dilatometrskih preizkušancev

Martin Herrejón-Escutia[1] – Gildardo Solorio-Díaz[1] – Héctor Javier Vergara-Hernández[2] – Edgar López-Martínez[3] – Gerardo Marx Chávez-Campos[2] – Octavio Vázquez-Gómez[2,4,*]

[1] Univerza sv. Nikolaja Hidalga v Michoacanu, dodiplomski program strojništva, Mehika
[2] Inštitut za tehnologijo v Moreliji, Podiplomski in raziskovalni oddelek, Mehika
[3] Univerza Tehuantepeške ožine, Mehika
[4] Nacionalni svet za znanost in tehnologijo, Mehika

Razvit je bil matematični model Joulovega segrevanja votlega cilindričnega dilatometrskega preizkušanca iz nerjavnega jekla AISI 304. Model napoveduje potek temperature v odvisnosti od električnega toka in določa funkcijo toka, ki je potreben za konstantno hitrost segrevanja. Model povezuje temperaturno polje in temperaturne deformacije z enačbami za mehanske deformacije in temperaturni raztezek.

Matematični model obravnava Newtonsko segrevanje diferencialnega elementa volumna, kjer je energijsko ravnotežje doseženo s sklopitvijo člena za nastanek Joulove toplote in členov za akumulacijo in oddajanje toplote s konvekcijo in sevanjem. Iz energijskega ravnotežja izhaja vodilna diferencialna enačba za temperaturno polje. Enačba je razrešena po metodi končnih razlik s posebno programsko kodo v brezplačnem paketu Scilab®. Model določa termofizikalne in električne lastnosti jekla v odvisnosti od temperature.

Eksperimentalni preizkusi so bili opravljeni z napravo za Joulovo segrevanje, sestavljeno iz grelnika, infrardečega pirometra za merjenje temperature in laserskega mikrometra za merjenje temperaturnih raztezkov. Naprave krmili vdelan sistem za zajem podatkov.

Za razrešitev matematičnega modela je bilo treba določiti tri toplotne robne pogoje: 1) skupni koeficient prenosa toplote na zunanji površini, 2) temperaturo v notranjosti in 3) skupni koeficient prenosa toplote na notranji površini preizkušanca. Trije toplotni robni pogoji so bili določeni kot funkcija temperature. Za oceno temperaturnega raztezka je bilo treba najprej določiti vrednost koeficienta temperaturnega raztezka jekla AISI 304 z eksperimentalnimi meritvami spremembe zunanjega premera glede na to, da je temperaturni raztezek enak dilataciji preizkušanca.

Model je bil validiran s primerjavo toplotnega odziva in eksperimentalno določenih temperaturnih raztezkov ter rezultatov simulacije pri različnih hitrostih segrevanja. Ujemanje rezultatov eksperimentov in simulacije je sprejemljivo, zato so bili validirani tudi toplotni robni pogoji in eksperimentalni koeficient linearnega temperaturnega raztezka.

Z analizo občutljivosti je bil ocenjen vpliv kritičnih vhodnih spremenljivk na toplotno zgodovino preizkušanca. Za posnemanje materiala z večjo in manjšo prevodnostjo je bila uporabljena spremenjena električna prevodnost nerjavnega jekla AISI 304. Debelina vzorca je bila spremenjena z zmanjševanjem ogrevane mase in povečevanjem gostote električnega toka skozi preizkušanec.

Simulacije so bile opravljene s superzlitino Hastelloy® C-276 in nerjavnim jeklom AISI 304, pri čemer je bila opravljena primerjava časovnega poteka temperature, funkcije električnega toka in temperaturnih deformacij.

Končno je bil razvit matematični model Joulovega segrevanja votlega cilindričnega preizkušanca z oceno poteka temperature, zgodovine električnega toka in odstotka dilatacije. Dokazano je bilo tudi, da je toplotne robne pogoje mogoče določiti z empiričnimi korelacijami, inverznim modelom prevoda toplote in eksperimentalnimi podatki. Model je bil uspešno validiran za dve kovinski zlitini, ki nimata faznega prehoda v obravnavanem temperaturnem območju. Z analizo občutljivosti je bil ugotovljen vpliv električne prevodnosti in debeline preizkušanca na potek temperature. Rezultati simulacij so pokazali, da nikljeva zlitina Hastelloy® C-276 zaradi svoje električne prevodnosti doseže nižjo temperaturo kot jeklo AISI 304, medtem ko je njen temperaturni raztezek večji kot pri nerjavnem jeklu 304.

Ključne besede: matematični model, neprekinjeno segrevanje, Joulov efekt, dilatometrija, nerjavno jeklo AISI 304

*Naslov avtorja za dopisovanje: Nacionalni svet za znanost in tehnologijo, Av. Insurgentes 1582, 03940 Mexico City, Mehika, ovazquezgo@conacyt.mx

Na Fakulteti za strojništvo Univerze v Ljubljani so obranili svojo doktorsko disertacijo:

- dne *3. julija 2017* **Nejc LUKAČ** z naslovom: »Vpliv časovnega poteka bliskov laserja Er:YAG na procese v snovi z visoko vsebnostjo vode« (mentor: izr. prof. dr. Andrej Senegačnik);

Svetloba laserja Er:YAG se zaradi izredno močne absorpcije v vodi uporablja za natančno segrevanje, uparevanje in odstranjevanje trdih in mehkih tkiv. Disertacija je usmerjena v raziskave vpliva časovnega poteka dovajanja svetlobne energije laserja Er:YAG na segrevanje in odstranjevanje snovi, ki vsebuje vodo. V ta namen smo razvili merilne metode za hitro spremljanje uparevanja in odstranjevanja tkiva med bliskovnim osvetljevanjem ter na osnovi teoretičnih in eksperimentalnih ugotovitev predlagali vrsto rešitev za izboljšanje oblike časovnega poteka bliska za različne vrste laserskih medicinskih posegov. Vsi eksperimenti so bili opravljeni na *in-vitro* vzorcih;

- dne *4. julija 2017* **Kosta SIMONOVIĆ** z naslovom: »Model for Friction Prediction of Diamond like Carbon Coatings (DLC) in Boundary Lubrication Conditions« (mentor: prof. dr. Mitjan Kalin);

V doktorski nalogi smo raziskovali posamične in skupne učinke proti-obrabnega aditiva (cink-dialkil-dithiofosfat, ZDDP), modifikatorja trenja (glicerol isostearat, GIS) in paketa aditivov za avtomobilske motorje na trenje v kontaktih jeklo-jeklo ter jeklo-DLC v širokem območju kontaktnih pogojev mejnega mazanja. Metoda načrtovanja eksperimentov (DOE) je bila uporabljena za pridobitev eksperimentalne matrike ter metoda regresije elastične mreže (Elastic Net) je bila uporabljena za pridobitev modela trenja in map trenja, v odvisnosti od najbolj relevantnih kontaktnih parametrov: tlaka, hrapavosti, temperature in hitrosti. Pridobljeni modeli temeljijo na eksperimentalnih parametrih in njihovih interakcijah, statistična značilnost parametrov in interakcij je bila nedvomno potrjena. Značilni zaključek je, da statistično potrjeni parametri in njihove interakcije kažejo, kateri od preučevanih parametrov skupaj vplivajo na koeficient trenja, torej, kateri eksperimentalni parametri se ne morejo individualno preučevati v režimu mejnega mazanja, če želimo priti do veljavnih zaključkov. Pokazano je, da zgolj eno-parametrske študije režima mejnega mazanja ne kažejo pravih lastnosti kontaktov v celotnem področju mejnega mazanja;

- dne *11. julija 2017* **Andrej ČEBULAR** z naslovom: »Vodenje procesa radiofrekvenčnega varjenja« (mentor: izr. prof. dr. Primož Podržaj);

Radiofrekvenčno varjenje je postopek spajanja dielektričnih neprevodnih materialov z vnosom elektromagnetne energije. Prednosti te tehnologije pred konvencionalnimi postopki segrevanja so hiter in efektiven vnos energije, nizka stopnja kontaminacije materiala in možnost integracije v avtomatizirano proizvodnjo. Ta tehnologija se v veliki meri uporablja pri proizvodnji biomedicinskih pripomočkov, kot so raztopinske vrečke in vrečke za dializo. Spremljanje kakovosti v proizvodnji biomedicinskih pripomočkov večinoma temelji na izvajanju destruktivnih testov iz statističnega vzorca, preko katerega se nato sklepa o kvaliteti širše populacije. Ideja predloženega dela je razviti metodologijo in sistem za neinvazivno določanje kvalitete vara na podlagi realnočasnega spremljanja procesa varjenja in odločitvenih struktur z nevronskimi mrežami. Razviti so bili postopki meritev in merilni sistem za spremljanje anodnega toka, anodne napetosti, potisne sile orodja in pomika orodja med procesom radiofrekvenčnega varjenja. S študijo procesa radiofrekvenčnega varjenja in eksperimentalnim delom so bile ugotovljeni vplivi različnih parametrov krivulje anodnega toka in krivulje pomika orodja na kvaliteto vara. Najvplivnejši parametri so bili uporabljeni za pripravo vhodnih vektorjev v nevronske mreže LVQ, ki so zavarjene vzorce, na podlagi zajetih podatkov iz meritev, uspešno razvrstile v skupino ustreznih oziroma neustreznih izdelkov.

Information for Authors

All manuscripts must be in English. Pages should be numbered sequentially. The manuscript should be composed in accordance with the Article Template given above. The maximum length of contributions is 10 pages. Longer contributions will only be accepted if authors provide juastification in a cover letter. For full instructions see the Information for Authors section on the journal's website: http://en.sv-jme.eu .

SUBMISSION:

Submission to SV-JME is made with the implicit understanding that neither the manuscript nor the essence of its content has been published previously either in whole or in part and that it is not being considered for publication elsewhere. All the listed authors should have agreed on the content and the corresponding (submitting) author is responsible for having ensured that this agreement has been reached. The acceptance of an article is based entirely on its scientific merit, as judged by peer review. Scientific articles comprising simulations only will not be accepted for publication; simulations must be accompanied by experimental results carried out to confirm or deny the accuracy of the simulation. Every manuscript submitted to the SV-JME undergoes a peer-review process.

The authors are kindly invited to submit the paper through our web site: http://ojs.sv-jme.eu. The Author is able to track the submission through the editorial process - as well as participate in the copyediting and proofreading of submissions accepted for publication - by logging in, and using the username and password provided.

SUBMISSION CONTENT:

The typical submission material consists of:

- A **manuscript** (A PDF file, with title, all authors with affiliations, abstract, keywords, highlights, inserted figures and tables and references),
- Supplementary files:
  - a **manuscript** in a WORD file format
  - a **cover letter** (please see instructions for composing the cover letter)
  - a ZIP file containing **figures** in high resolution in one of the graphical formats (please see instructions for preparing the figure files)
  - possible **appendicies** (optional), cover materials, video materials, etc.

Incomplete or improperly prepared submissions will be rejected with explanatory comments provided. In this case we will kindly ask the authors to carefully read the Information for Authors and to resubmit their manuscripts taking into consideration our comments.

COVER LETTER INSTRUCTIONS:

Please add a **cover letter** stating the following information about the submitted paper:

1. Paper **title**, list of **authors** and their **affiliations**.
2. **Type of paper**: original scientific paper (1.01), review scientific paper (1.02) or short scientific paper (1.03).
3. A **declaration** that neither the manuscript nor the essence of its content has been published in whole or in part previously and that it is not being considered for publication elsewhere.
4. State the **value of the paper** or its practical, theoretical and scientific implications. What is new in the paper with respect to the state-of-the-art in the published papers? Do not repeat the content of your abstract for this purpose.
5. We kindly ask you to suggest at least two **reviewers** for your paper and give us their names, their full affiliation and contact information, and their scientific research interest. The suggested reviewers should have at least two relevant references (with an impact factor) to the scientific field concerned; they should not be from the same country as the authors and should have no close connection with the authors.

FORMAT OF THE MANUSCRIPT:

The manuscript should be composed in accordance with the Article Template. The manuscript should be written in the following format:

- A **Title** that adequately describes the content of the manuscript.
- A list of **Authors** and their **affiliations**.
- An **Abstract** that should not exceed 250 words. The Abstract should state the principal objectives and the scope of the investigation, as well as the methodology employed. It should summarize the results and state the principal conclusions.
- 4 to 6 significant **key words** should follow the abstract to aid indexing.
- 4 to 6 **highlights;** a short collection of bullet points that convey the core findings and provide readers with a quick textual overview of the article. These four to six bullet points should describe the essence of the research (e.g. results or conclusions) and highlight what is distinctive about it.
- An **Introduction** that should provide a review of recent literature and sufficient background information to allow the results of the article to be understood and evaluated.
- A **Methods** section detailing the theoretical or experimental methods used.
- An **Experimental section** that should provide details of the experimental set-up and the methods used to obtain the results.
- A **Results** section that should clearly and concisely present the data, using figures and tables where appropriate.
- A **Discussion** section that should describe the relationships and generalizations shown by the results and discuss the significance of the results, making comparisons with previously published work. (It may be appropriate to combine the Results and Discussion sections into a single section to improve clarity.)
- A **Conclusions** section that should present one or more conclusions drawn from the results and subsequent discussion and should not duplicate the Abstract.
- **Acknowledgement** (optional) of collaboration or preparation assistance may be included. Please note the source of funding for the research.
- **Nomenclature** (optional). Papers with many symbols should have a nomenclature that defines all symbols with units, inserted above the references. If one is used, it must contain all the symbols used in the manuscript and the definitions should not be repeated in the text. In all cases, identify the symbols used if they are not widely recognized in the profession. Define acronyms in the text, not in the nomenclature.
- **References** must be cited consecutively in the text using square brackets [1] and collected together in a reference list at the end of the manuscript.
- **Appendix(-icies)** if any.

SPECIAL NOTES

Units: The SI system of units for nomenclature, symbols and abbreviations should be followed closely. Symbols for physical quantities in the text should be written in italics (e.g. *v*, *T*, *n*, etc.). Symbols for units that consist of letters should be in plain text (e.g. ms^{-1}, K, min, mm, etc.). Please also see: http://physics.nist.gov/cuu/pdf/sp811.pdf .

Abbreviations should be spelt out in full on first appearance followed by the abbreviation in parentheses, e.g. variable time geometry (VTG). The meaning of symbols and units belonging to symbols should be explained in each case or cited in a **nomenclature** section at the end of the manuscript before the References.

Figures (figures, graphs, illustrations digital images, photographs) must be cited in consecutive numerical order in the text and referred to in both the text and the captions as Fig. 1, Fig. 2, etc. Figures should be prepared without borders and on white grounding and should be sent separately in their original formats. If a figure is composed of several parts, please mark each part with a), b), c), etc. and provide an explanation for each part in Figure caption. The caption should be self-explanatory. Letters and numbers should be readable (Arial or Times New Roman, min 6 pt with equal sizes and fonts in all figures). Graphics (submitted as supplementary files) may be exported in resolution good enough for printing (min. 300 dpi) in any common format, e.g. TIFF, BMP or JPG, PDF and should be named Fig1.jpg, Fig2.tif, etc. However, graphs and line drawings should be prepared as vector images, e.g. CDR, AI. Multi-curve graphs should have individual curves marked with a symbol or otherwise provide distinguishing differences using, for example, different thicknesses or dashing.

Tables should carry separate titles and must be numbered in consecutive numerical order in the text and referred to in both the text and the captions as Table 1, Table 2, etc. In addition to the physical quantities, such as *t* (in italics), the units [s] (normal text) should be added in square brackets. Tables should not duplicate data found elsewhere in the manuscript. Tables should be prepared using a table editor and not inserted as a graphic.

REFERENCES:

A reference list must be included using the following information as a guide. Only cited text references are to be included. Each reference is to be referred to in the text by a number enclosed in a square bracket (i.e. [3] or [2] to [4] for more references; do not combine more than 3 references, explain each). No reference to the author is necessary.

References must be numbered and ordered according to where they are first mentioned in the paper, not alphabetically. All references must be complete and accurate. Please add DOI code when available. Examples follow.

Journal Papers:

Surname 1, Initials, Surname 2, Initials (year). Title. Journal, volume, number, pages, DOI code.

[1] Hackenschmidt, R., Alber-Laukant, B., Rieg, F. (2010). Simulating nonlinear materials under centrifugal forces by using intelligent cross-linked simulations. *Strojniški vestnik - Journal of Mechanical Engineering,* vol. 57, no. 7-8, p. 531-538, DOI:10.5545/sv-jme.2011.013.

Journal titles should not be abbreviated. Note that journal title is set in italics.

Books:

Surname 1, Initials, Surname 2, Initials (year). Title. Publisher, place of publication.

[2] Groover, M.P. (2007). *Fundamentals of Modern Manufacturing*. John Wiley & Sons, Hoboken.

Note that the title of the book is italicized.

Chapters in Books:

Surname 1, Initials, Surname 2, Initials (year). Chapter title. Editor(s) of book, book title. Publisher, place of publication, pages.

[3] Carbone, G., Ceccarelli, M. (2005). Legged robotic systems. Kordić, V., Lazinica, A., Merdan, M. (Eds.), Cutting Edge Robotics. Pro literatur Verlag, Mammendorf, p. 553-576.

Proceedings Papers:

Surname 1, Initials, Surname 2, Initials (year). Paper title. Proceedings title, pages.

[4] Štefanić, N., Martinčević-Mikić, S., Tošanović, N. (2009). Applied lean system in process industry. *MOTSP Conference Proceedings*, p. 422-427.

Standards:

Standard-Code (year). Title. Organisation. Place.

[5] ISO/DIS 16000-6.2:2002. *Indoor Air – Part 6: Determination of Volatile Organic Compounds in Indoor and Chamber Air by Active Sampling on TENAX TA Sorbent, Thermal Desorption and Gas Chromatography using MSD/FID.* International Organization for Standardization. Geneva.

WWW pages:

Surname, Initials or Company name. Title, from http://address, date of access.

[6] Rockwell Automation. Arena, from *http://www.arenasimulation.com,* accessed on 2009-09-07.

EXTENDED ABSTRACT:

When the paper is accepted for publishing, the authors will be requested to send an **extended abstract** (approx. one A4 page or 3500 to 4000 characters). The instruction for composing the extended abstract are published on-line: http://www.sv-jme.eu/information-for-authors/ .

COPYRIGHT:

Authors submitting a manuscript do so on the understanding that the work has not been published before, is not being considered for publication elsewhere and has been read and approved by all authors. The submission of the manuscript by the authors means that the authors automatically agree to transfer copyright to SV-JME when the manuscript is accepted for publication. All accepted manuscripts must be accompanied by a Copyright Transfer Agreement, which should be sent to the editor. The work should be original work by the authors and not be published elsewhere in any language without the written consent of the publisher. The proof will be sent to the author showing the final layout of the article. Proof correction must be minimal and executed quickly. Thus it is essential that manuscripts are accurate when submitted. Authors can track the status of their accepted articles on http://en.sv-jme.eu/.

PUBLICATION FEE:

Authors will be asked to pay a publication fee for each article prior to the article appearing in the journal. However, this fee only needs to be paid after the article has been accepted for publishing. The fee is 240.00 EUR (for articles with maximum of 6 pages), 300.00 EUR (for articles with maximum of 10 pages), plus 30.00 EUR for each additional page. The additional cost for a color page is 90.00 EUR. These fees do not include tax.

Strojniški vestnik -Journal of Mechanical Engineering
Aškerčeva 6, 1000 Ljubljana, Slovenia,
e-mail: info@sv-jme.eu

9 770039 248001
ISSN 0039-2480

http://www.sv-jme.eu

Contents

Papers